Exploration of Optoelectronic Properties in Lead Halide Perovskites

Seonhong Min

Department of Chemistry

The Graduate School of Sungshin Women's University

Exploration of Optoelectronic Properties in Lead Halide Perovskites

A Master's Thesis

Submitted to the

Graduate School of Sungshin Women's University

in partial fulfillment of the requirements

for the degree of

Master of Science

Seonhong Min

May, 2024

This is to certify that we have examined the

Master's Thesis of

Seonhong Min

Submitted to Department of Chemistry

Approved as to style and content:

Committee Chairman: Yoonho Lee

Committee Member: Bonjae Koo

Committee Member: Junsang Cho

The Graduate School of Sungshin Women's University

ABSTRACT

Exploration of Optoelectronic Properties in Lead Halide Perovskites

Seonhong Min

Department of Chemistry

Graduate School of

Sungshin Women's University

Three-dimensional (3D) and two-dimensional (2D) lead halide perovskites have been considered as a promising material for light-emitting diodes and photovoltaics due to its tunable optoelectronic properties such as band gap, absorption or emission wavelength, charge carrier recombination dynamics, etc,. These properties can be finely-tunned to modulate the nanocrystals size, halide ion composition and surface ligands. First, we have investigated Pb-X

bonding strength (more ionic Pb−Cl versus more covalent Pb−I) in lead octahedral $[PbX_6]^{4-}$and their impact on growth kinetics in 3D bulk nanocrystals. We determined the activation energies for growth kinetic in $CsPbX_3$ (X = Cl, and I) nanocrystals; 92 kJ/mol for $CsPbCl_3$ and 71 kJ/mol for $CsPbI_3$.

Second, we have elucidated the halide ion migration activation energy in 2D lead halide perovskites. Binding mode of spacer ligand in 2D structures generated by multi− or mono− dentate nature of ligand affects the rigidity of lead halide frameworks which is associated with halide vacancy formation and halide stability. Halide ion migration kinetic in RP phase and DJ phase of 2D lead halide perovskites is elucidated by temperature− and thickness− dependent spectroscopic measurements. We determined the activation energies for halide ion migration kinetic in 2D perovskites with different binding mode of spacer; 50.9kJ/mol for Ruddlesden−Popper (RP) vs and 60.8kJ/mol for Dion−Jacobson (DJ) phase, respectively.

In summary, understanding such growth mechanism related with chemical bonding of Pb−X and structure characteristic of 2D lead halide perovskites provides strategies for synthesis of dimensionally−

tunable perovskites across 3D–2D for optoelectronic application in light–emitting diodes or photovoltaics.

TABLE OF CONTENTS

LIST OF FIGURES

LIST OF TABLES

CHAPTER I

Introduction

Dimensionally Tunable 3D–2D Lead Halide Perovskite

Three–dimensional (3D) lead halide nanocrystals have general formula of ABX_3 structures, where A cation is [eg., Cs^+(cesium), FA^+ (formamidinium), and MA^+ (methylammonium)] located the center of $[PbX_6]^{4-}$ octahedra frameworks connected by corner–sharing [7] **(Figure I.2)**. These Lead halide perovskites are extensively investigated as a

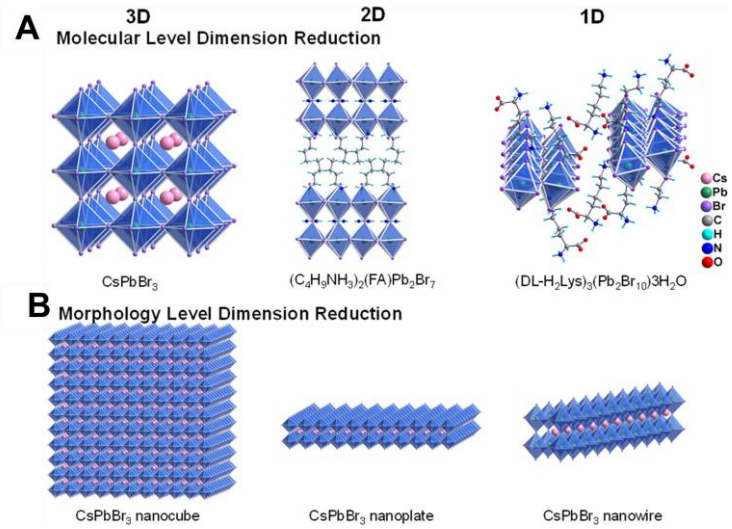

Figure I.1. Dimensional reduction at the (A) molecular and (B) morphological level. Reprinted with permission form ref [6]. Copyright © 2021 American Chemical Society

promising candidate in the field of optoelectronics for light-emitting diodes (LEDs), photovoltaics, photodetector, and X-ray scintillating imaging.[1–4] These lead halide perovskites are facile to control for their dimensionality across three-dimension (3D) to zero-dimension (0D) at the molecular level. Tunable optoelectronics properties can provide a degree of freedom to modulate bandgap, charge carrier lifetime, photoluminescence (PL) quantum yield, and halide stability[5,6] **(Figure I.1).** By dimensionality and halide composition engineering, we can further tune optoelectronic properties of perovskites to achieve perovskites LEDs with

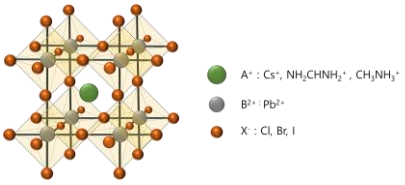

Figure I.2. Crystal structure of lead halide perovskites.

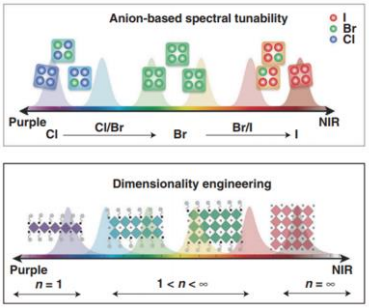

Figure I.3. Schematic representation of spectral tunability in lead halide perovskites by anion and dimensionality engineering. Reprinted with permission form ref [8]. Copyright *Light Sci Appl* **10**, 61 (2021)

color pure and full-color emission covering color gamut of National Television System Committee (NTSC) standard CIE diagram[20]. (**Figure I.3**)

Importantly, the lead halide perovskites compared to other semiconductor are defect-tolerant materials[9]. **Figure I.4** shows the electronic structure of MAPbI3 including its intrinsic defect. In lead halide perovskites, the defect energy level which is produced by halide vacancies or dangling bond are generated nearby or inside the band edges. These shallow defects leading to low nonradiative recombination rates can influence the device performance and stability. [9,10]

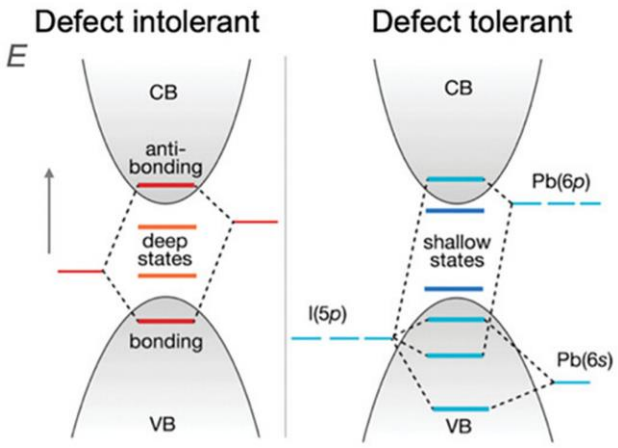

Figure I.4. Electronic structure of typical III-V, II-VI, or group IV semiconductors (left) compared to the lead halide perovskite crystal structure (right). Reprinted with permission form ref 9. Copyright © 2017 American Chemical Society.

Generally, 2D lead halide perovskite can be classified into i) Ruddlesden–Popper (RP) phase ($L_2A_{n-1}Pb_nX_{3n+1}$) and ii) Dion–Jacobson (DJ) phase ($LA_{n-1}Pb_nX_{3n+1}$) where in L is spacer ligands; monodentate spacer cation (e.g., butylammonium, phenethylammonium, etc.) for RP

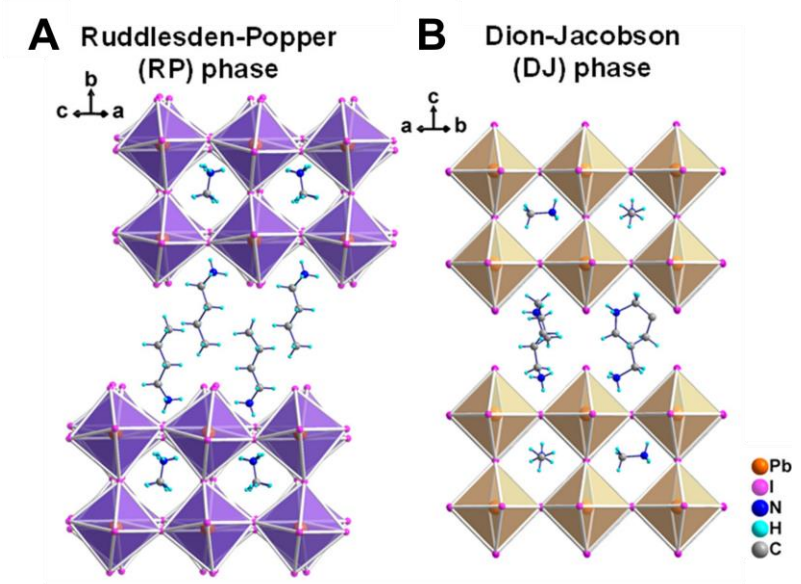

Figure I.5. Crystal structure of two–dimensional lead halide perovskites; (A) Ruddlesden–Popper phase and (B) Dion–Jacobson phase. Reprinted with permission from ref 6 . Copyright © 2021 American Chemical Society.

phase and bidentate spacer cation (e.g., butane–1,4–diamine, 1,4–phenylenedimethanammoium, etc.) for DJ phase; A is a monovalent cation; (e.g., Cs+, MA+ and FA+, etc.); and X is halide (Cl, Br and I)[6]. **(Figure I .5)** By introducing the organic spacer cation into the octahedra frameworks of 3D perovskites, two–dimensional (2D) sheets are generated with different

layer number (n) as illustrated in Figure Ⅰ.5. The inserted large organic cations (L; spacer ligand) into the 3D perovskites $[PbX_6]^{4-}$ inorganic sheets give rise to dielectric mismatch between inorganic well (barrier) and organic well which can be called quantum well (QW) [6,11,12].

This quantum well structure provides not only quantum confinement effect but also dielectric confinement effect as compared to 3D lead halide perovskites. In particular, the dielectric confinement effect is governed by the layer number in 2D perovskites due to the decreasing of dielectric constant (ε) with increasing the thickness of the inorganic sheets so in the 3D perovskites (bulk) this effect is entirely disappeared[13]. The research fields of 2D metal halide perovskites rapidly grow in the last few

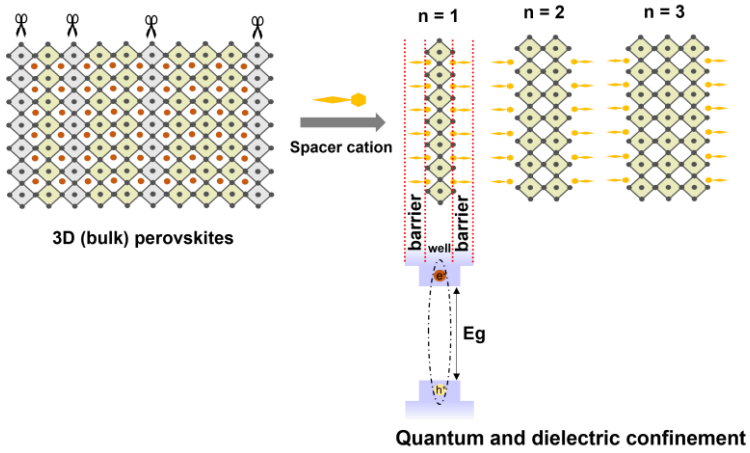

Figure I.6. Illustrations of 2D perovskites generation by introducing the spacer organic cation into the 3D perovskites and quantum and dielectric confinement effect created by quantum well structure.

years rather than 3D perovskites since, by modulating the QW structure (*n* value of 2D perovskites), the bandgap and carrier recombination dynamics can be fine-tuned for achieving the Pb-based optoelectronic device with better performance stability.[3,11,14]

Generally, 2D lead halide perovskite can be classified into i) Ruddlesden-Popper (RP) phase ($L_2A_{n-1}Pb_nX_{3n+1}$) and ii) Dion-Jacobson (DJ) phase ($LA_{n-1}Pb_nX_{3n+1}$) where in L is spacer ligands; monodentate spacer cation (e.g., butylammonium, phenethylammonium, etc.) for RP phase and bidentate spacer cation (e.g., butane-1,4-diamine, 1,4-phenylenedimethanammoium, etc.) for DJ phase; A is a monovalent cation; (e.g., Cs+, MA+ and FA+, etc.); and X is halide (Cl, Br and I). **(Figure I .6)**

Kinetics of Perovskite Nanocrystals Crystallization and Ostwald Ripening

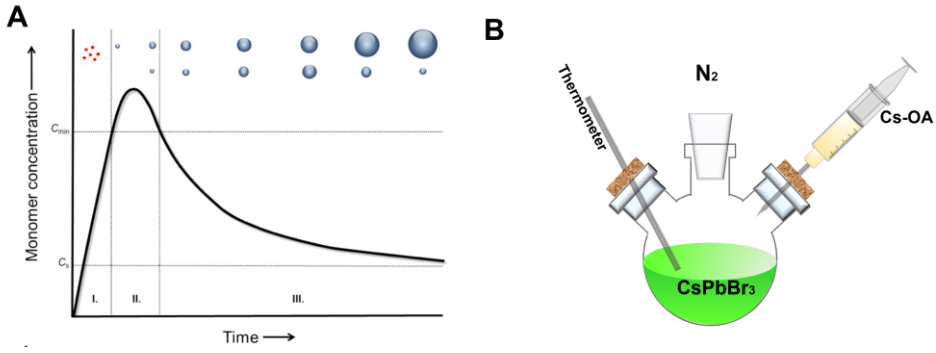

Figure I.7. (A) Lamer plot model and (B) Schematic of hot-injection method for synthesis of CsPbBr3 perovskite nanocrystals. (A) is reprinted with permission from ref15. Copyright © 2015 American Chemical Society.

Generally, growth of nanocrystals including the perovskite nanocrystals can be understood as illustrated in Lamer plot[15] **Figure Ⅰ.7A)**. For synthesis the homogeneous nanocrystals, the concentration of the precursor and reactant reach the supersaturation instantly for rapidly inducing the nucleation. Especially, in the Pb-based optoelectronic devices, nonhomogeneous perovskite nanocrystals which induce the randomicity of optoelectronic properties give rise to poor device performance [16,17]. If there is rapid nucleation and additional nucleation is suppressed simultaneously, final nanocrystals will be obtained with maintaining size uniformity with the same grow pathway.

Hot-injection method is generally used for synthesis of colloidal perovskite nanocrystals[18,19] **(Figure Ⅰ.7B)**. With this method the burst nucleation can be achieved by controlling the precursor reactivity with adjusting the temperature parameter. Lead halide (PbX_2) salt is dissolved with surface-passivating ligands containing long hydrocarbon chains at the elevated temperatures. When heating the solution over the precursor decomposition temperature or injecting the precursor solution at higher temperature, as shown in nucleation step in Lamer plot model (Figure Ⅰ.7A), the monomer concentration rapidly rise above the nucleation threshold (; supersaturation). After the nucleation process is

completed due to the consumption of precursors or abrupt decrease the reaction temperature, the monomer concentration level drops below the threshold of nucleation and crystal growth process starts. Especially, the perovskite nanocrystals size is controlled by regulating the organic ligand ratio, chain length of ligand and the precursor injection temperature [20–22]. Thus, corresponding optical band gap energy can be tuned by controlling such parameters.[21,23].

Nanocrystals growth mechanism is also elucidated by Ostwald ripening process which is gradual transition for the larger nanocrystal with small surface area. The driving force of this natural phenomenon is difference of surface energy between a small crystal (large surface area) and a large crystal (small surface area) [24]. There are several factors that affect Ostwald ripening including concentration gradient, temperature, reaction time and so on. For instant, higher temperatures increase the solubility of the crystals, so smaller crystals dissolve more easily than larger ones, resulting in the growth of larger crystals at the expense of smaller crystals [24–26]. Similarly, in film casted perovskite nanocrystals from colloidal solution, annealing time or temperature of films are considered as the factor affecting the Ostwald ripening [22]. Understanding, therefore, growth mechanisms in terms of Ostwald ripening and the factors is important to

optimize nanocrystals growth process for producing the device with high-quality nanocrystals.

Halide Ion Migration in Lead Halide Perovskites.

Halide ion migration is governed by two processes: diffusion and ion exchange reaction [27]. Generally, vacancy or interstitial diffusion mechanisms carry out the ion migration in lead halide perovskites lattice

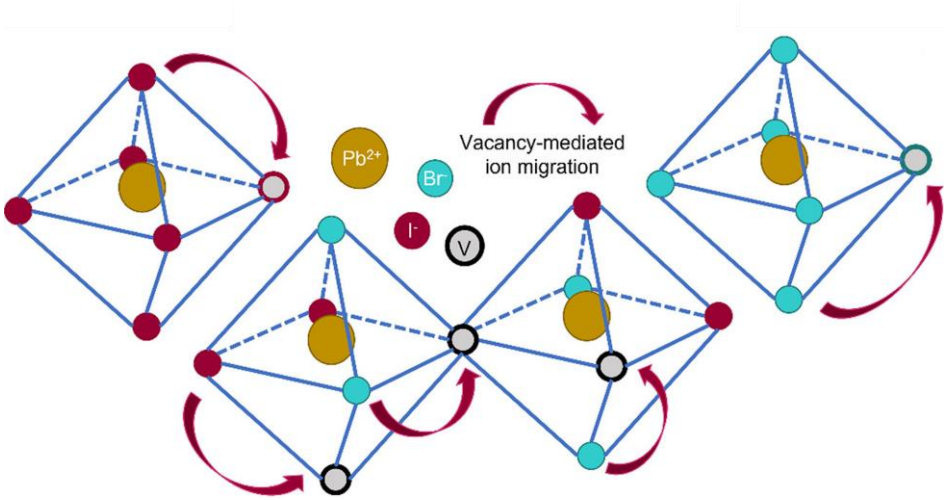

Figure I.8. Schematic of halide ion migration and mixed halide migration in l[PbX6]4- octahedral framework mediated by vacancy. Reprinted with permission from ref[28]. Copyright © 2021 American Chemical Society

(Figure I .8)[27,28]. The X-site halide ion of the lattice has lowest activation energy due to the facile vacancy-assisted diffusion, whereas the lead cation is located at the center of octahedral lattice $[PbX_6]^{4-}$, creating a significant energy barrier that suppresses the ion migration [27,28]. A-site

cation is occupied large volume within lead halide perovskites lattice. Consequently, for this large cation to migrate, it must overcome the four adjacent halide ions, involving a higher activation energy than that required for the halide ions. Defects in lead halide perovskites also has great impact on ion diffusion [28]. For its low formation energy including interstitial and vacancy of A-site, Pb and halide site, the defects lower the activation energy of diffusion which enable halide ions to access facile pathway for inter diffusion [27-29].

Halide ion exchange reaction, for example in ABX_3 perovskite nanocrystals, is followed by the chemical equation (1) [27].

$$ABX_3 + X'^- \rightarrow ABX_2X'^- + X'^- \cdots \rightarrow ABX_3'^- \quad (1)$$

When the new halide ion (X'^-) diffuse into the parent ABX3 nanocrystals, the counterpart X ion is extracted. The halide exchange can be conducted by liquid phase process and solid phase process (figure 1.1).

Post-synthetic halide exchange method is widely used in liquid phase process [30,31]. In this method, the halide source is directly loaded into the parent $CsPbX_3$ nanocrystals for fast halide exchanges. The metal halide salts: lead halide (PbX_2), zinc halide (ZnX_2), etc., are dissolved in organic ligand solvent: oleic acid, oleyl ammine, etc., as a halide source [27]. This is

one of the simple methods to adjusting the halide ratio for fine tuning the band gap, achieving full color emissive mixed halide perovskite nanocrystals in visible spectral region [27,30,31]. However, in the solid phase exchange process, the halide ion diffuses across the interface of the films. The solid state of lead halide perovskites (2D or 3D) films with different halide composition are synthesized by thin film deposition method and then the films are physically paired for halide ion migration at the surface [27,29]. In the lead halide perovskite films with specific thickness, the halide exchange procedure consists of three steps: first, the halide ion is extracted and diffuse to the interface of the films; second, the halide exchange at the surface; third, the halide ion diffuses inside the film [27].

CHAPTER II

How Chemical Bonding Impacts Halide Perovskite Nanocrystals Growth to Bulk Films: Implication of Pb−X Bond on Growth Kineics *

II.1 INTRODUCTION

Lead halide perovskites nanocrystals with the chemical formula of $APbX_3$ (A = methylammonium (MA), formamidinium (FA), and cesium (Cs); X = Cl, Br, and I) have emerged as a leading candidate in the various field of applications including photovoltaics[32,33], light−emitting didoes[34-36], photodetector[37-39], and X−ray scintillators[40,41]. Such perovskite nanocrystals exhibit fascinating optoelectronic properties such as tunable bandgap, high absorption cross−section, narrow emission, long carrier diffusion length, and high photoluminescent quantum yield.[42-45] Given their favorable optical and electronic properties, significant research effort has been made thus far toward understanding and controlling the growth of

* Reprinted with permission from "How chemical bonding impacts Halide Perovskites Nanocrystals to Bulk Films: Implication of Pb−X Bond on Growth Kinetics" by S. Min, H. Choe, S. Hyun Jung, J. Cho *ChemPhysChem*. 2023, 24, e202300202.

such perovskite nanocrystals to achieve more desirable properties.[46-48] Of particular interest in perovskite nanocrystals is the bandgap tunability that can be readily accomplished by varying either size or composition of nanocrystals.[46,49-51] As such, controlling the size of halide perovskite nanocrystals and understanding the correlation between size and optoelectronic property remains an important issue since it is directly linked to the performances and stability of perovskite photovoltaics and optoelectronic devices.[52] For instance, Kim et al reported that $CsPbBr_3$ nanocrystals beyond the quantum confinement regime (and exciton Bohr diameter) exhibit the high photoluminescent quantum yield and stability.[53,54] Also, Kamat et al thoroughly investigated the growth of $CsPbBr_3$ nanocrystals to bulk films.[55-57] In-situ tracking of the spectroscopic features such as emission and absorption allows for understanding the size-dependent nanocrystal growth mechanism.[55-59] It has been revealed that control over the grain size and grain boundaries, mostly acting as carrier recombination sites, influence the excited state dynamics involving different charge carrier separation or recombination kinetics within nanocrystals that also directly affects the efficiency of perovskite-based devices.[60-64]

As a result of ionic bonding characteristics and soft lattices of halide perovskites, fast nucleation and concurrent growth make it difficult to study the growth mechanism of halide perovskite nanocrystals that is strikingly different from more covalent solid nanocrystals such as CdSe and InP nanocrystals.[35,46,65] Recently, Akkerman et al have reported that using trioctylphosphine oxide (TOPO), serving as a complexation agent with a monomer, indeed allows for a slower release of Pb monomer, thus enabling to separate nucleation and growth events of $CsPbBr_3$ nanocrystals.[65] With a longer time scale up to 30 minutes, in-situ tracking of spectral features of nanocrystals can allows for elucidating the nucleation and growth mechanism of $CsPbBr_3$ nanocrystals. One of the important questions to be answered is how the chemical bonding in $CsPbX_3$ (ionicity or covalency governed by the type of halide ions that are directly bound to Pb^{2+} metals by forming $[PbX_6]^{4-}$ octahedral frameworks) influence the growth kinetics of nanocrystals, transforming to bulk films.[55-57] Throughout such transformation, we can indeed obtain a better understanding of size- and surface-defect- dependent changes in the optoelectronic properties of lead halide perovskites. In this study, we have, thus, investigated the growth kinetics using entire series of analogue lead halide nanocrystals including $CsPbCl_3$ (more ionic), $CsPbBr_3$

(intermediate), and $CsPbI_3$ (more covalent) with different chemical bonding motifs but these all are derived from the same parent of $CsPbBr_3$ through halide ion exchanges. Upon subjecting to thermal treatment of nanocrystal films, lead halide perovskite nanocrystals grow, transforming into bulk films. Different growth kinetics governed by the type of halide ions provide a significant insight into the important role of chemical bonding in lead halide perovskites, also playing a critical role in controlling the growth of perovskite nanocrystals to induce more desired optoelectronic properties depending upon photovoltaic (fast dissociation of carriers) or light-emitting applications (fast recombination of carriers) that is also strongly size dependent.[66]

II.2EXPERIMENTAL

Materials

Lead chloride ($PbCl_2$, 99%, Alfa Aesar), Lead bromide ($PbBr_2$, 98+%, Alfa Aesar), Lead iodide (PbI_2, 98.5%, Alfa Aesar), cesium carbonate (Cs_2CO_3, 99%, Alfa Aesar), oleic acid (OA, technical grade 90%, Sigma Aldrich), oleylamine (OLAm, technical grade 70%, Sigma Aldrich), 1-octadecene (ODE, 90%, Sigma Aldrich), Hexanes (96%, Samchun Chemicals), Glass substrate (Plain-type, 90°, SciLab). All chemicals were used as received without additional purification.

Synthesis of CsPbBr3 Nanocrysyals.

The preparation of $CsPbBr_3$ nanocrystals follows the previously reported method with a hot injection.[79-81] First, cesium oleate (Cs-OA) precursor solution was prepared by mixing 0.3693 g of Cs_2CO_3 (1.13 mmol) with 3.4 mL of OA (10.7 mmol) and 3.6 mL of ODE in the 50 ml three-neck rock bottom flask. The reaction mixture was further heated at 150 °C. Second, for the synthesis of $CsPbBr_3$ nanocrystals, 0.828 g of $PbBr_2$ (2.26 mmol), 6mL of OA (18.88 mmol), 6 mL of OLAm (19.05 mmol), and 10 mL of ODE were placed in the 50mL of three neck round bottom flaks. The reaction flask containing mixtures was degassed at 100 °C for 30 min and put under

vacuum. Next, reaction temperature of the flask is ramping to 170 °C under a N_2 flow and 4 mL of as-prepared Cs-OA was swiftly injected. After 10 seconds of reaction, the flask was immediately quenched with an ice water bath. To purify the obtained nanocrystals, the reaction products was centrifuged at 4000 rpm for 10 min and then the precipitates was collected after discarding the supernatant. The precipitates were resuspended to make a colloidal stable dispersion in hexanes.

Halide Exchange Reactions.

Halide exchange reaction using the as-synthesized parent $CsPbBr_3$ was performed by adapting a previously reported method [66,67]. Briefly, halide source stock solutions 0.375 M for Cl (0.188 M for I) were prepared separately by dissolving 0.628 g of $PbCl_2$ (0.52 g of PbI_2) with 1.5 mL of oleic acid, 1.5 mL of oleylamine, and 3 mL of ODE in 20 mL of vial, respectively. Halide stock solution was then heated at using temperature-controlled hot plate under vigorous stirring to entirely dissolve the solids. Next, systematically controlled volume of the halide stock solution was added to parent $CsPbBr_3$ solution in hexanes to yield halide-exchanged nanocrystals of $CsPb(Br_{1-x}Cl_x)_3$ (x = 0-1) and I-rich $CsPb(Br_{1-y}I_y)_3$ (y = 0-1). The final halide compositions such as x and y can be determined

by using Vegard’ s law. The samples were spun down by centrifuging at 4000 rpm for 10 min.

Annealing Experiments Using Nanocrystals Thin Films.

A thin film on glass substrates was prepared by following the methods reported in the previous literature precedence [58,82]. Before deposition of nanocrystals on glasses to make thin films, 1 inch x 1 inch glass substrates were firstly prepared by cutting the microscope slide glass which were further cleaned by sonicating in an ethanol bath for 10 min. The substrates were then treated with ozone cleaner for 10 min to remove organic residues. The perovskite nanocrystals (through directly synthesized via hot injection or post-synthetically prepared via halide exchange) were deposited on the glass substrates by spin-casting at 4000 rpm for 5 s and 5000 rpm for 30 s. Briefly, annealing experiments were conducted by placing the as-prepared 1 inch x 1 inch nanocrystal thins films (Cl and I) on a temperature-controlled hot plates in the temperature range of 110-200 °C. The films were thermally annealed with the desired time and taken periodically for spectroscopic measurements. The completion of annealing was visually seen with color changes of the films.

Characterizations.

Absorption.

UV−Vis absorption spectra were taken using a Varian Cary 60 spectrophotometer in the wavelength of 350—700 nm for $CsPbX_3$ nanocrystals dispersed in hexanes and nanocrystal films deposited on glass substrates. The difference absorption spectra were plotted by subtracting the absorption spectrum taken at initial time (at 0 min or 0 sec) from the absorption spectra taken at longer time. The spectrum of 0 min (or 0 sec) serves as a reference for difference absorbance spectra.

Photoluminescence (PL).

Photoluminescence measurements were performed using JASCO FP−8550 spectrofluorometer in the wavelength of 380−750 nm for $CsPbX_3$ nanocrystals dispersed in hexanes (for solution) and nanocrystal films (for solid) deposited on glass substrates. Excitation wavelength of 365 nm was chosen with a 0.5 nm of scan step size, a 0.1 sec dwell time, and a slit width of 10 nm for both excitation and emission measurements.

Powder X-ray diffraction (XRD).

Powder X-ray diffraction (XRD) measurements were carried out using a Bruker D8 Focus X-ray Powder Diffractometer with a Cu Kα radiation source (λ = 1.5406 Å) in the 2θ range from 10-50°.

Scanning and Transmission Electron Microscope.

Field emission scanning electron microscope (SEM) measurements were made using a JEOL Ltd. JSM-7500F operated at an accelerating voltage of 10 kV. The transmission electron microscopy (TEM) images were taken using a JEM-2100F (HR) (JEOL LTD) at an operating voltage at 200 kV.

Analysis of Grain Size

From X-ray diffraction patterns, Scherer equation is used to determine the grain size along (200) crystallographic planes for the annealed films. The broadening (or sharpening) of the diffraction peak is referred to the grain size (equation 1).

$$\tau = K\lambda / \beta \cos\theta \qquad (1)$$

where τ is the average crystallographic grain (domain) size; K is a shape factor (0.9 is sued here); λ is the wavelength of X-ray beam; β is the line broadening (full width at the half maximum) in radians; and θ is the

Bragg angle.

Tauc Plot Analysis for Bandgap determination.

The absorption spectra were converted to *Tauc* plots using the equation of $(\alpha h\nu)^2$ versus $h\nu$. The straight line was extrapolated from the curvature onto X−axis to estimate the bandgap energy (E_g) of the perovskites as a function of halides. Bandgap of pure $CsPbBr_3$ nanocrystals is 2.41 eV whereas the those of fully exchanged chloride and iodide are 2.91 and 1.82 eV, respectively. Halide compositions were determined based upon the estimated bandgap of the mixed halide perovskites in the range of x and y for $CsPb(Br_{1-x}Cl_x)_3$ (x =0−1) and I−rich $CsPb(Br_{1-y}I_y)_3$ (y = 0−1), following the Vegard's law (equations 4−5).

$$\text{Bandgap (eV) of the } CsPb(Br_{1-x}Cl_x)_3 = (1-x)\times 2.41 + x\times 2.9 \quad (4)$$

$$\text{Bandgap (eV) of the } CsPb(Br_{1-y}I_y)_3 = (1-y)\times 2.41 + y\times 1.8 \quad (5)$$

II.3 RESULTS AND DISCUSSION

Post-synthetic Halide Ion Exchanges in $CsPbX_3$ Nanocrystals.

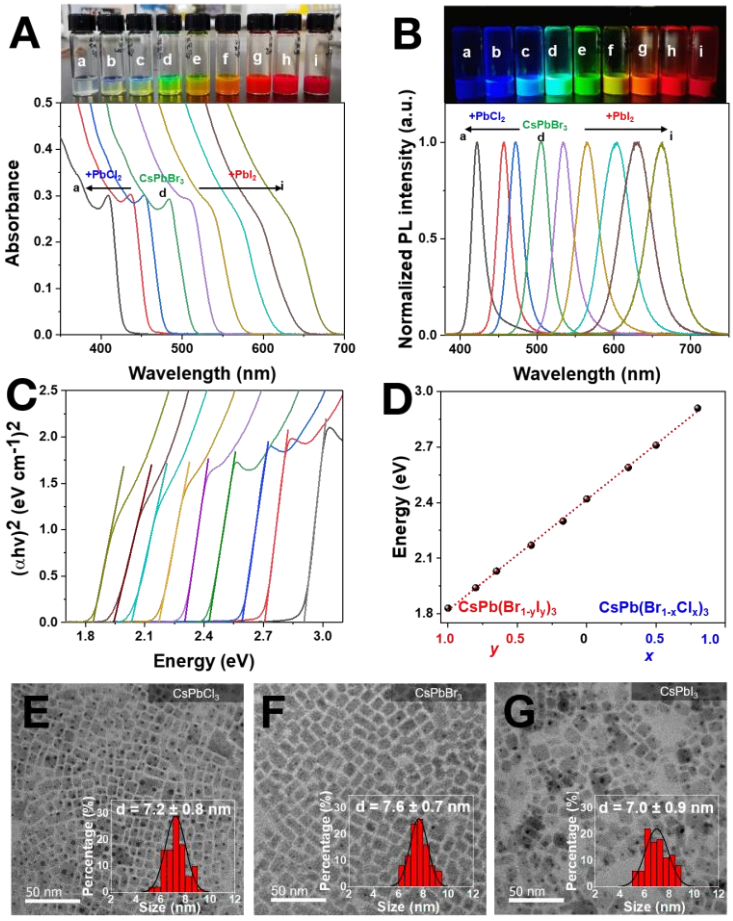

Figure II.1. (A) Absorption and (B) Normalized PL emission spectra for Cl-exchanged $CsPb(Br_{1-x}Cl_x)_3$ (x =0-1) and I-exchanged $CsPb(Br_{1-y}I_y)_3$ (y = 0-1) nanocrystals prepared through halide ion exchanges using the same parent $CsPbBr_3$ nanocrystals (a-i). (C) Tauc plots of panel A and (D) corresponding bandgap determined from panel C for entire series of $CsPbX_3$ nanocrystals shown in panel A. (E-G) Transmission electron microscope images for $CsPbCl_3$(E), $CsPbBr_3$ (F), and $CsPbI_3$ (G). Average

To elucidate the effect of the chemical bonding of Pb−X (determined by the degree of ionicity and covalency of halide ions) on growth kinetics of $CsPbX_3$ (X=Cl, Br, and I) nanocrystals, we have adopted a post−synthetic anion exchange to obtain the same size of nanocrystals with different halides.[67,68] Halide ion exchanges were performed using the same parent $CsPbBr_3$ nanocrystals to prepare homologous series of $CsPbX_3$ nanocrystals with the same size by adding other halide sources ($PbCl_2$ or PbI_2). Post−synthetic ion exchanges enable to preserve the original crystal structure and size of parents yet only alter the anion sublattice and composition spanning from Cl to Br and to I, which enables to rule out any size dependent properties (i.e. surface energy) that probably affect growth kinetics of nanocrystals [63]. The parent $CsPbBr_3$ (green−emitting) and mixed halide perovskites including $CsPb(Br_{1-x}Cl_x)_3$ (x =0−1; blue−emitting) and I−rich $CsPb(Br_{1-y}I_y)_3$ (y = 0−1; red−emitting) nanocrystals are stabilized, respectively. **Figures II.1A,B** display the corresponding absorption and emission features of $CsPbX_3$ nanocrystals. The band−edge absorption (and emission maxima) peaks are controlled in the entire visible spectral range of 410−640 nm (and 420−660 nm). As seen from color changes as a function of varying the halide composition, the band−edge absorption was continuously shifted from 490 nm (for parent

$CsPbBr_3$) to 405 nm (for $CsPbCl_3$) and to 660 nm (for $CsPbI_3$), respectively. Simultaneously, the emission features were also shifted from 505 nm ($CsPbBr_3$) to 420 nm (for $CsPbCl_3$) and to 660 nm (for $CsPbI_3$), respectively. Digital photographs taken under ambient room light (left) and UV excitation (right) vividly describes the coloration of lead halide perovskite nanocrystals as a function of halide compositions (**Figures II.1A,B**). As the halide composition changes, corresponding bandgap also alters continuously since the valence bands position of perovskite nanocrystals are primarily dictated by halide *n*p orbitals (3p for Cl, 4p for Br, and 5p for I) whereas the conduction band edge does not change significantly owing to isoenergetic Pb 6p orbitals [35]. The bandgap of the lead halide perovskites can be readily determined from Tauc plot analysis as depicted in **Figure II.1C**. Corresponding bandgap of the lead halide perovskites shown in **Figure II.1D** indicates that the bandgap of $CsPbX_3$ nanocrystals is varied as a function of the halide compositions of $CsPb(Br_{1-x}Cl_x)_3$ (x =0−1) and $CsPb(Br_{1-y}I_y)_3$ (y = 0−1). As the halide composition changes from parent Br to Cl in the range of x = 0−1 (Br → Cl) and to I in the range of y = 0−1 (Br → I), respectively, the bandgap of the lead halide perovskites changes in the range of 1.8−2.9 eV continuously, following the Vegard ' s law. Transmission electron microscope (TEM) images for $CsPbCl_3$ (x = 1), $CsPbBr_3$ (parents), and

$CsPbI_3$ (y =1) nanocrystals, respectively, revealed that there were no significant changes in the size of nanocrystals during the anion exchange reactions (**Figures II.1E–G** and **Figure A.1A,B**). All of the $CsPbX_3$ nanocrystals retained their original size with an average diameter of ~7–8 nm regardless of the halide compositions. A small deviation in size distribution is mainly derived from the size distribution of as-synthesized nanocrystals. This is in line with previous reports that soft anionic lattices of the lead octahedral enable the topochemical transformation without altering the unit cell and lattices [69,70].

Growth Kinetics of CsPbX3 Nanocrysyals.

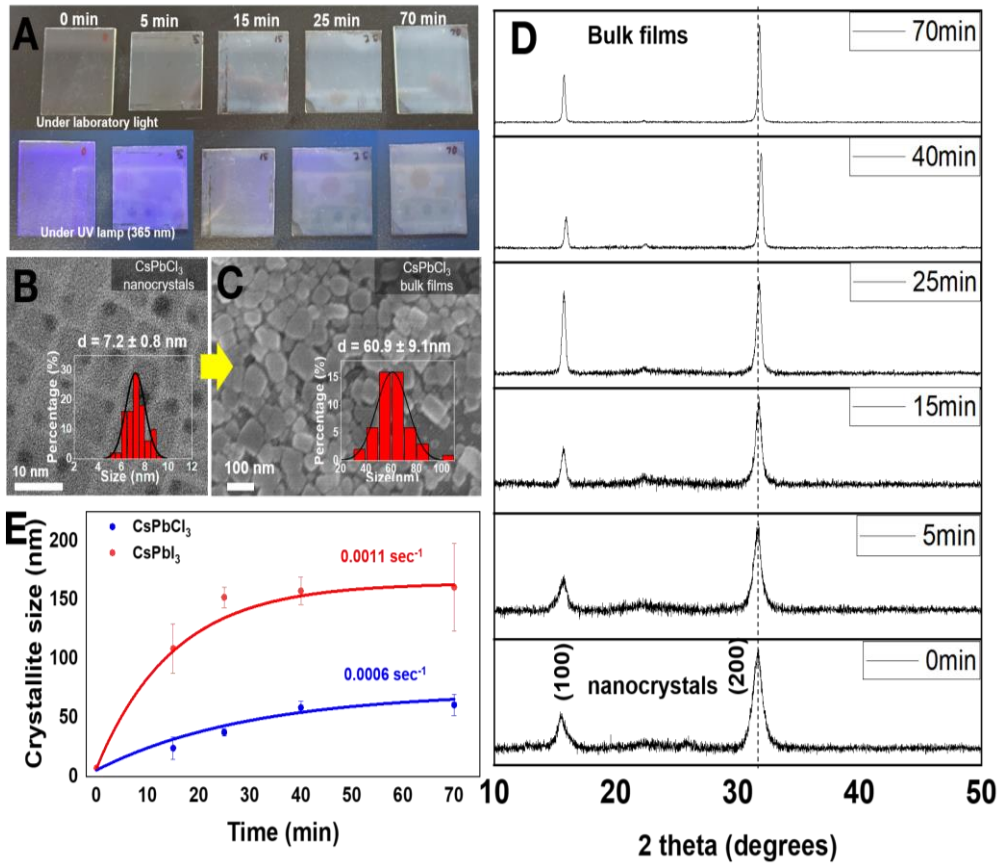

Figure II.2. (A) Digital photographs taken under laboratory light (top) and 365 nm UV lamp (bottom) for $CsPbCl_3$ nanocrystals annealed at 130 °C for different annealing time (0−70 min). (B,C) Transmission electron microscope images taken for 0 min sample (B) and scanning electron microscope image taken for 70 min sample (C). (D) X−ray diffraction patterns for $CsPbCl_3$ nanocrystal films annealed from 0−70 min. (E) Size evolution of average crystallite size of $CsPbCl_3$ and $CsPbI_3$ nanocrystal films upon annealing determined by counting 50 particles from SEM images as shown in Figures (S3 and S5). Monoexponential fits were used to determine the kinetic rate constant of growth of $CsPbCl_3$ and $CsPbI_3$ shown in panel E.

Using the perovskite nanocrystals with different halide compositions, we have further prepared $CsPbX_3$ nanocrystal films through spin-coating on the glass substrates performed at 5000 rpm for 30 seconds. **Figure A.2A** shows as-prepared nanocrystal thin films of $CsPbCl_3$, $CsPbBr_3$, and $CsPbI_3$, respectively, without changes in band-edge absorption and emission features between colloidal nanocrystals and films with nanocrystals deposited on the glass substrate (**Figures A.2B,C**). Digital photographs of such films taken under UV excitation of 365 nm confirm the bright luminescence from each nanocrystal film as a result of quantum confinement effects despite the deposition on the substrates (**Figure A.2A**). When the nanocrystal thin films were thermally treated with a temperature-controlled hot plate, the growth of $CsPbX_3$ nanocrystals into bulk films can be seen [55,57]. As a representative example, **Figure II.2** displays the digital photographs of $CsPbCl_3$ nanocrystal films that were annealed at 130 °C for different annealing times of 0-70 mins under laboratory light (top) and 365 nm UV lamp (bottom). The disappearance of blue emission upon increasing annealing times (> 5 min) reflects that nanocrystals transformed into larger crystallites beyond the quantum confinement regime, in which exciton can be readily dissociated into free charge carriers (or electrons and holes), preferring to undergo

nonradiative recombination. Scanning electron microscope (SEM) images directly provide evidence of growths that initial $CsPbCl_3$ nanocrystals with a size of 7.2±0.8 nm (for 0 min) evolved into larger crystallite with a size of 60.9±9.1 nm (for 70 min), as displayed in **Figures II.2B–C and Figures A.3A–F** (Supporting Information). X-ray diffraction (XRD) patterns for the films corresponding to a panel of Figure 2A were taken (**Figure II.2D**). XRD pattern obtained at 0 mins shows the orthorhombic crystal structure of $CsPbCl_3$ with strong reflection peaks at 15.5 ° and 31.7° that are assigned to (100) and (200) crystallographic planes. As evidenced by the digital photographs and microscope images, the reflection peaks became sharper with increasing annealing times, indicative of the growth of nanocrystals. Using the Scherrer equation (see the details in the Experimental section of the Supporting Information), the average crystallite size (or domain size) along (200) planes gradually increased from ~8 nm (for 0 min) to 32 nm (for 70 min) with the thermal treatment (**Figure A.4A**). We have also repeated the annealing experiment with $CsPbI_3$ nanocrystal films for SEM and XRD measurements (**Figures A.4B and A.5A–F**), following similar growth mechanism like $CsPbCl_3$ films but different growth kinetics (**Figure II.2E**). Such growth is based upon Oswald ripening mechanism: the larger crystallites prefer to grow into larger with an expense of small nanocrystals, consistent with earlier reports with

$CsPbBr_3$ nanocrystals.[55,71] This process is thermodynamically preferable, driven by the difference in surface free energies between larger and smaller nanocrystals. The lower surface free energy of larger crystallites is thermodynamically more stable, thus preferring to grow larger by scarifying the smaller particles with a higher surface free energy.[72,73]

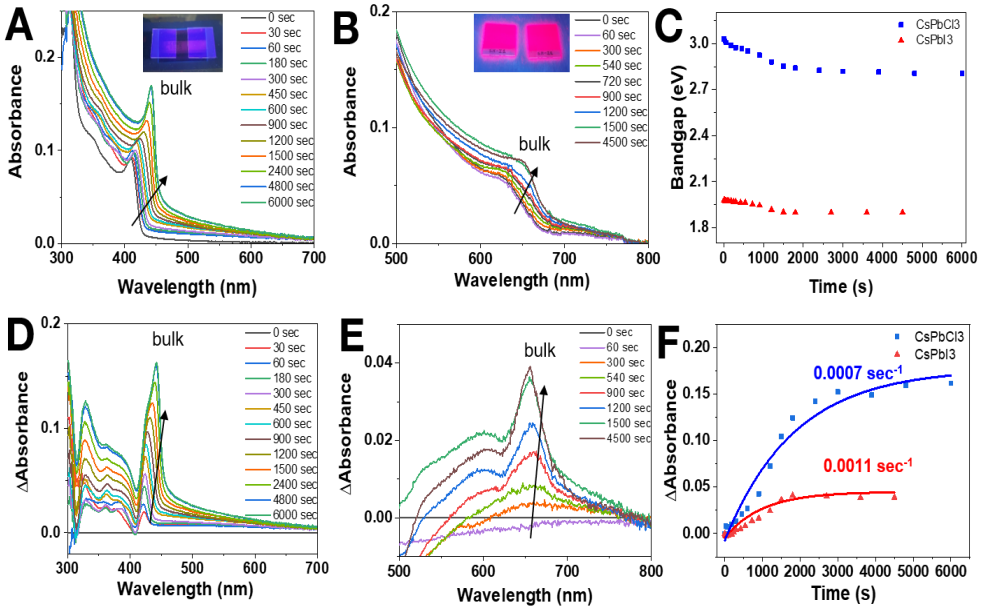

Figure II.3. (A,B) Absorption spectra acquired for the $CsPbCl_3$ (A) and $CsPbI_3$ (B) nanocrystal thin films annealed at 130 °C for different annealing time. (C) Corresponding bandgap changes determined from Tauc plots for $CsPbCl_3$ and $CsPbI_3$. (D,E) Difference absorption spectra of panel A,B for the $CsPbCl_3$ (D) and $CsPbI_3$ (E) nanocrystal thin films. (F) Kinetic traces and monoexponential fits for $CsPbCl_3$ and $CsPbI_3$ nanocrystal by tracking the bulk peak at 440 nm (for $CsPbCl_3$) and 650 nm (for $CsPbI_3$). The photo shown in panels A,B is a pair of nanocrystal thin films under 365 nm UV excitation.

During the Oswald ripening, the chemical bonding of Pb−X and surface free energy might play a critical role in growth kinetics. When the changes in the average crystallite size (determined from SEM images) were fitted using a monoexponential function, it was revealed that the growth of $CsPbI_3$ (k: 0.0011 sec^{-1}) is approximately two times faster than that of $CsPbCl_3$ (k: 0.0006 sec^{-1}).

To further investigate the growth kinetics of such nanocrystal films, we have recorded the absorption of the nanocrystal films of $CsPbCl_3$ and $CsPbI_3$, respectively, during the course of different annealing times (**Figures II.3A,B**). Band−edge absorption of nanocrystals shifted to longer wavelength for $CsPbCl_3$ (405 → 440 nm; 3A)[74] and $CsPbI_3$ (630 → 655nm; 3B), respectively. Corresponding bandgap changes when nanocrystals are converted to bulks are seen in **Figure II.3C** as determined from Tauc plot analysis (**Figures A.6A,B**). These changes in spectroscopic absorption peak provide the size−dependent bandgap of nanocrystals. The size of nanocrystals increased whereas the bandgap decreased upon increasing annealing times, mirroring the previous observations from SEM and XRD measurements. Apparently, the increased portion of scattering observed from 500−700 nm (for CsPbCl3) and 700−800 nm (for CsPbI3) indirectly provide an evidence of increased size of crystallographic grains

for both films, in line with observation from SEM (**Figures II.2B,C**).[75,76] The changes in the absorption during the growth of nanocrystals can be more apparently visualized through taking difference absorption (⊿A) spectra that are further obtained by subtracting the initial spectrum at 0 sec (serving as a reference) from the absorption spectrum taken at longer times (> 0 sec). **Figures II.3D,E** shows ⊿A spectra corresponding to $CsPbCl_3$ (3D) and $CsPbI_3$ (3E) nanocrystal films, respectively. As the nanocrystals transformed to larger crystallites, absorption peaks corresponding to bulk features of each lead halide perovskites (at 440 nm for $CsPbCl_3$ and at 670 nm for $CsPbI_3$) have appeared as a function of increasing the annealing time. By tracking such changes in these bulk peaks shown from the difference absorptions ⊿A, growth kinetics of bulk crystals can be extracted. **Figure II.3F** shows the bulk growth kinetic traces and fitting obtained from ⊿A spectra with a rate constant for growth to bulk films of 0.0011 sec^{-1} (for $CsPbI_3$) and 0.0007 sec^{-1} (for $CsPbCl_3$), respectively. In terms of completion of growth to bulk from nanocrystals, it takes around 4000−6000s for $CsPbCl_3$ and 1500−2000 s for $CsPbI_3$, respectively. From microscopic and spectroscopic observations, it was concluded that the growth of more covalent

nanocrystals of $CsPbI_3$ is faster than that of more ionic $CsPbCl_3$ nanocrystals.

How Pb−X Bonds Affect Growth Kinetics.

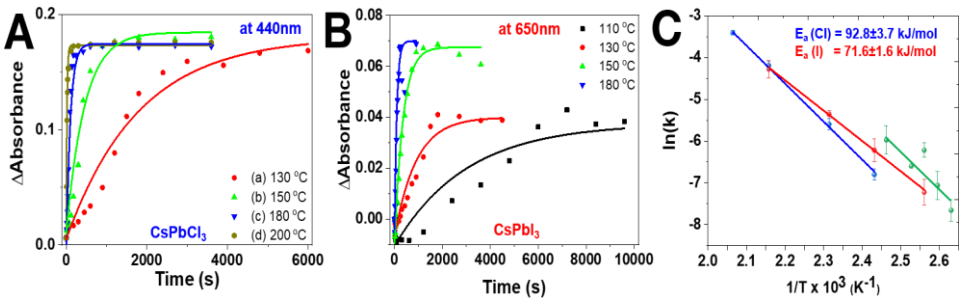

Figure II.4. (A,B) Changes in difference absorption spectra of nanocrystal films by tracking the bulk peak at 440nm (for $CsPbCl_3$; A) and 650 nm (for $CsPbI_3$; B) during the course of annealing at different temperatures (110−200 °C). (C) Arrhenius plot of ln(k) versus inverse temperature (1/T) obtained from the kinetic fitting of panels A,B. Monoexponential fits were used for determination of rate constant (k) as shown in panels A,B. For the relative comparison of activation energy between different $CsPbX_3$ nanocrystals, the literature values corresponding to the activation energy of 75 kJ/mol for $CsPbBr_3$ nanocrystals are plotted together in panel C, based upon the previous report.[55]

To further understand the effect of chemical bonding of Pb−X on growth kinetics and activation energies, we have repeated the annealing experiments shown in Figures 3 (performed at 130 °C) at various annealing temperatures ranging from 110−200 °C. It has been clearly established that the temperature−dependent growth behaviors of $CsPbBr_3$

nanocrystals following the Arrhenius relationship.[55] In this study, we have focused on growth of two different characteristic nanocrystals at the end (more ionic $CsPbCl_3$ *versus* more covalent $CsPbI_3$). **Figures II.4A,B** exhibit the kinetics traces and monoexponential fittings of two different nanocrystal films as seen from difference absorption spectra by tracking the bulk peaks at 440 nm for $CsPbCl_3$ (**Figure II.4A**) and at 650 nm for $CsPbI_3$, respectively (**Figure II.4B**). **Figures A.7A–F** (for $CsPbCl_3$) and **A.8A–F** (for $CsPbI_3$) of the Supporting Information shows the absorption and corresponding difference absorption spectra recorded at different annealing times for $CsPbCl_3$ (150, 180, and 200 °C) and $CsPbI_3$ (110, 150, and 180 °C), respectively. It is worth mentioning that annealing of the $CsPbCl_3$ nanocrystals films at 110 °C takes 8000–10000 s for completion of growth and kinetic traces was significantly deviated from the monoexponential fitting (**Figure A.9A–C** of the Supporting Information). This is probably cooling of the nanocrystal films in air during the measurements that might be more critical when annealed at lower temperature. The kinetic traces can be further fitted using a monoexponential function, and corresponding rate constant (k) can be obtained at the different temperatures. By plotting the natural log of rate

constant ($\ln(k)$) versus inverse temperature (1/T), Arrhenius relationship as described in the following equation (1) can be established

$$\ln(k) = -\frac{Ea}{RT} + \ln(A) \qquad (1)$$

where k is the rate constant; E_a is growth activation energy; A is the preexponential factor; and T is the absolute temperature using Kelvin scale (K). Temperature-dependent rate constant reflects the growth rate get faster upon increasing the annealing temperatures, inducing faster transformation of nanocrystals into bulk for both $CsPbCl_3$ and $CsPbI_3$ nanocrystals, following the same growth mechanism. However, two different characteristic nanocrystals of $CsPbCl_3$ (more ionic) and $CsPbI_3$ (more covalent) with different bonding energy showed different growth kinetics. From the linear relationship between $\ln(k)$ and inverse temperature (1/T), the activation energy for growth of nanocrystals into bulk films were estimated to be 92.8 $\pm$ 3.7 kJ/mol (for $CsPbCl_3$) and 71.6

± 1.6 kJ/mol (for $CsPbI_3$), respectively. When monitoring the wavelength changes during the course of annealing at different temperatures, similar activation energy for $CsPbCl_3$ (87.8 ± 5.0 kJ/mol) and $CsPbI_3$ (74.8 ± 1.6 kJ/mol) films can be also estimated (**Figure A.10A–C** of the Supporting Information).

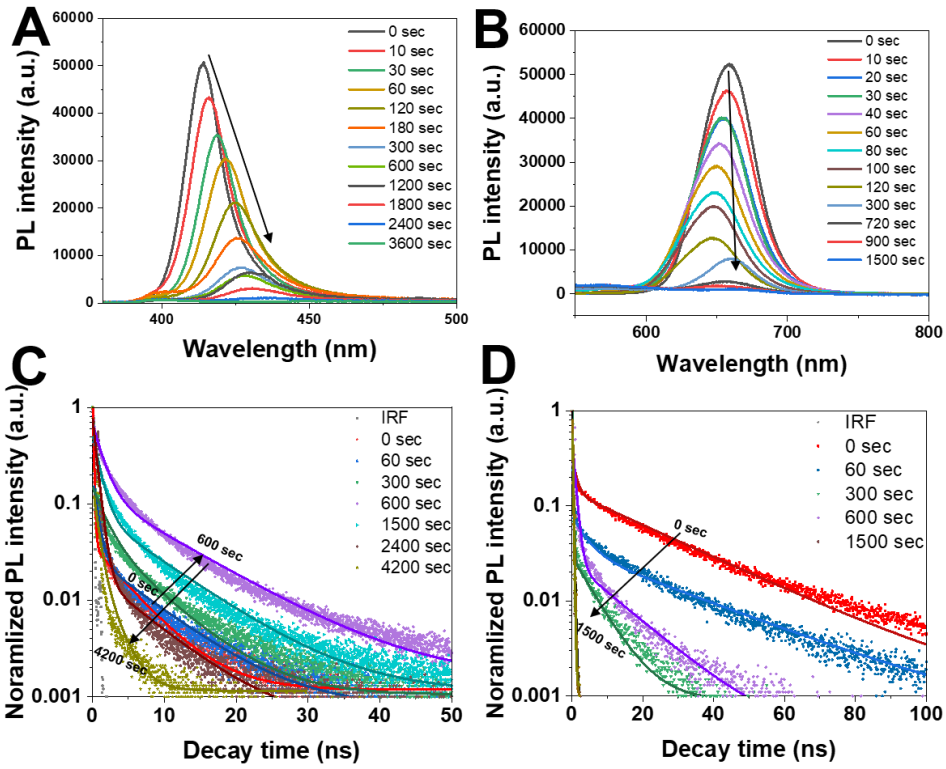

Figure II.5. (A,B) Changes in photoluminescence spectra throughout the sintering of the nanocrystal films of $CsPbCl_3$ (A) and $CsPbI_3$ (B), respectively, treated at 130 °C. (C,D) Corresponding photoluminescence decay curve and kinetic fittings for nanocrystal films of $CsPbCl_3$ (C) and $CsPbI_3$ (D), respectively, upon annealing at 130 °C. The kinetic fitting parameters and details are summarized in Table S1 of Supporting Information. Instrument response function (IRF) was obtained using hexanes alone.

To further understand the charge carrier recombination during the course of annealing of the nanocrystal films while the nanocrystals converted to bulk crystallites, we have recorded the photoluminescence (PL) changes over $CsPbCl_3$ and $CsPbI_3$ nanocrystal films as a function of annealing times (**Figures II.5A,B**). The maximum PL intensities of both nanocrystal films decreased upon annealing the films, reflecting that the size of crystallites grow upon annealing. As the size increased, the quantum confinements of larger crystallites became weaker which in turn diminish the PL intensity owing mainly to the reduced radiative recombination of charge carriers; carrier recombination dynamics will be examined in PL decay measurements later (*vide infra*). It is worth mentioning that it takes 2400 sec for $CsPbCl_3$ and 720 sec for $CsPbI_3$ films that the PL intensity was almost quenched upon thermal treatment as a result of increased crystallite sizes (**Figures II.5A,B**), suggesting that the growth kinetics of $CsPbI_3$ is much faster than that of CsPbCl3, consistent with previous SEM and absorption data (**Figures II.2– II.4**).

Then we have measured the PL decay for both films using time–correlated single photon counting (TCSPC) to elucidate the charge carrier recombination dynamics within different size of crystallites (**Figures 5C,D**). Corresponding PL decay kinetic traces can be fitted using biexponential

functions including a faster component and a slower component (equations 2) and average carrier lifetime can be further calculated (equation 3)

$$I = I_0 + A_1 \exp\left(-\frac{t}{\tau_1}\right) + A_2 \exp\left(-\frac{t}{\tau_2}\right) \quad (2)$$

$$\tau_{avg} = \frac{A_1\tau_1^2 + A_2\tau_2^2}{A_1\tau_1 + A_2\tau_2} \quad (3)$$

where A_1 is a weighted amplitute of the faster component; τ_1 is a lifetime of the faster component; A_2 is a weighted amplitute of the slower component; τ_2 is a lifetime of the slower component; and τ_{ave} is an average carrier lifetime.

Both films commonly show the similar growth behavior that upon annealing the films, the average carrier recombination lifetime reduced from 2.5−1.2 ns (for $CsPbCl_3$) and from 23.7−0.17 ns (for $CsPbI_3$) at the end of annealing as a result of loss of surface passivating ligands when subjected to the thermal treatment at 130 °C (**Figures II.5C,D**). These results reflect that the increased portion of A_1 components with significantly reduced τ_1 prefer a faster carrier recombination in the earlier stage. Interestingly, during the initial stage of the annealing for both $CsPbCl_3$ films (for 600 sec) and $CsPbI_3$ films (for 60 sec), the average carrier lifetime somewhat elongated from 2.5−6.7 ns (for $CsPbCl_3$) and from 23.7−26.5 ns (for

$CsPbI_3$), respectively, reflecting that the growth of nanocrystals into bit larger crystallites facilitates the dissociation of exciton (tightly bound one) into charge carriers (free electron and hole) upon annealing of films with a longer-lived carrier lifetime. The increased size of crystallite size with improved surface defect states favors retarded carrier recombination in the excited states. However, after growing above the certain limit of crystallites (around 20 nm), the average carrier lifetime started to decline, in consistent with the earlier reports, due mainly to loss of surface capping ligands along with increased surface defect states [55]. It is also worth mentioning that stronger surface interaction between surface passivating ligands of oleylammonium (acting as a hard acid) and Cl^- (acting as a hard base) in $CsPbCl_3$ nanocrystals can somewhat retard the growth kinetics of nanocrystals during the sintering while the weaker acid-base interaction with I^- (acting as a soft base) of $CsPbI_3$ nanocrystals gives rise to a faster growth due to the faster loss of ligands throughout the annealing process. Hence, in the case of $CsPbI_3$ films, we have seen the similar changes at even earlier stage owing to the faster growth of $CsPbI_3$ nanocrystals into larger particles.

Correlation of Halide Ionicity and Growth Kinetics.

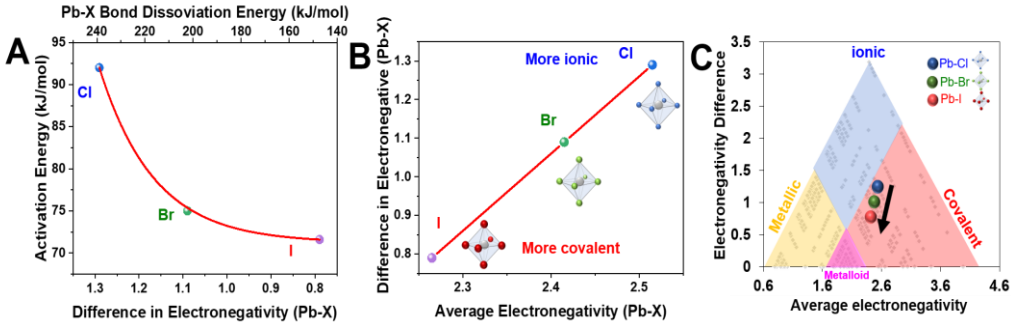

Figure II.6. (A) Activation energy of growth of nanocrystal to bulk films. The activation energy for $CsPbBr_3$ is based on the previous report.[55] (B) average electronegativity and difference in electronegativity between Pb and X (X = Cl, Br, I). (C) Van Arkel–Ketelaar triangle with Pauling electronegativity scale (blue: ionic, red: covalent, and yellow: metallic). The electronegativity used in this study is based upon Pauling electronegativity scale.

Previously, we have seen the decrease in the activation energy from more ionic $CsPbCl_3$ (93 kJ/mol) to more covalent $CsPbI_3$ (72 kJ/mol) as a function of decreasing the degree of ionicity of halides. Overall, the activation energy decreased in the order of $CsPbCl_3$ (93 kJ/mol) > $CsPbBr_3$ (75kJ/mol) > $CsPbI_3$ (72 kJ/mol). Such trend in activation energies indicates that the degree of ionicity and covalency that directly links to the bond energy of Pb−X in lead octahedral $[PbX_6]^{4-}$ affects the Oswald ripening growth kinetics (**Figure II.6A**). The growth and evolution of nanocrystals to bulk films is indeed mediated through the kinetic diffusion

of $Cs[PbX_3]$ monomers that are concurrently generated and released when smaller nanocrystals are dissolved back into solid solution during the Oswald ripening processes [48,65,77]. In other word, the higher surface free energy of smaller nanocrystals tends to dissolve back to produce monomeric species that in turn help to use for making and transforming into bulk crystals. The surface free energy (how thermodynamically stable or unstable) of nanocrystals in turn affects the monomer formation and corresponding growth kinetics of nanocrystals. From the perspective of Pb−X bonding, as the halide changes from more electronegative Cl to less electronegative I (electronegativity: Cl: 3.16 > Br:2.96 > I: 2.66), bonding motifs changes from ionic to covalent along with fixed central metal (Pb:1.87) of $[PbX_6]^{4-}$ octahedral frameworks (**Figure II.6B**). Based on average and difference of electronegativity between Pb and X, the bonding characteristics can be determined in Van Arkel-Ketelaar triangle (**Figure II.6C**), indicating that Pb−Cl is more ionic whereas Pb−I is more covalent than intermediate Pb−Br bond.

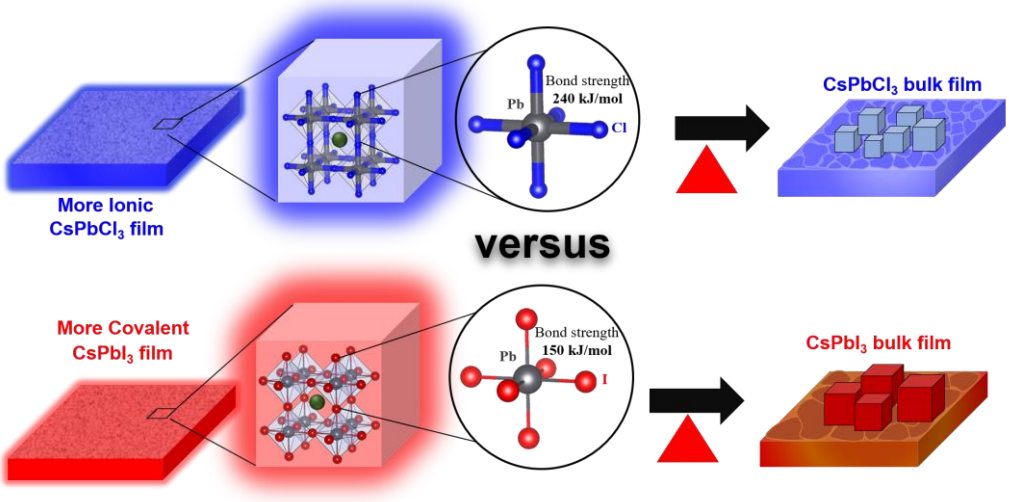

Figure II.7. Schematic illustration of transformative growth of nanocrystals to bulk films with atomistic picture based upon Pb−X chemical bonding.

Figure II.7 illustrates the growth kinetics of two different nanocrystals of $CsPbCl_3$ and $CsPbI_3$. More covalent Pb−I bonds with a less bonding energy of Pb−X exhibit a faster growth as compared to more ionic counterpart of Pb−Cl with the increased bonding energy in Pb−X. This is mainly ascribed to different ionic bonding energies that is derived from different electronegative of halides in lead octahedral frameworks $[PbX_6]^{4-}$ that is basic unit of perovskite lattices. Such ionic bond energy increased with the greater difference between cation (Pb) and anion (X = Cl, Br, and I). The Pb−X bond dissociation energy (kJ/mol) is also reported in the order of Pb−Cl (240) > Pb−Br (200) > Pb−I (150), consistent with the order of

electronegativity of halides (**Figures II.6A,B**) [49]. These reflect that Pb−Cl shows the strongest bonding energy among three Pb−X bonds due to increased portion of ionicity in the chemical bonding of Pb−X. Furthermore, thermodynamic parameters such as lattice enthalpy, surface energy, and interaction with surface passivating ligands (hard−soft acid−base interaction) influenced by different halides (Cl *versus* I) plays a critical role in growth of nanocrystals as well. During the process of dissolution of nanocrystal and monomer formation, higher lattices enthalpy (or smaller surface free energy) for more ionic solids as compared to less ionic counterparts makes them thermodynamically stable due to the stronger electrostatic interactions of cation and anion even at the surfaces. The observation of faster growth of $CsPbI_3$ as compared to $CsPbCl_3$ nanocrystals is also in line with the trend in halide ion migration.[20,46] By comparing the halide ion migration and resulting phase segregation for Cl/Br versus Br/I, more rigid framework with Cl shows the slower halide ion segregation owing to increased Pb−X bond strength and higher activation energy of segregation [49,78].

II.4 CONCLUSION

In summary, size-dependent optoelectronic properties (emission wavelength, bandgap, quantum yield, carrier diffusion length, and carrier recombination kinetics) and control over these properties remain an important in both field of photovoltaics and optoelectronic devices so as to achieve more desired optoelectronic properties. By tracking the transformative changes from nanocrystals to bulk films, we can understand the growth kinetics and mechanism of nanocrystals transforming to bulk crystallites. Chemical bonding of Pb-X mainly determined by the type of halide ions (and electronegativity of X) affected the growth kinetics of nanocrystals. The temperature-dependent study provides a fundamental understanding of the growth kinetics and activation energy of nanocrystals. Future studies are ongoing to elucidate the charge carrier dynamics with different crystal size and halide composition of perovskite nanocrystals to fully exploit such optoelectronic properties with fewer defect densities.

CHAPTER III

Halide Ion Mobility in Paired 2D Halide Perovskites: Ruddlesden Popper Versus Dion–Jacobson Phases*

III.1 INTRODUCTION

Two–dimensional (2D) metal halide perovskites with a reduced dimensionality compared to traditional three–dimensional (3D) perovskites have emerged as a promising candidate in the field of optoelectronics for photovoltaics, light–emitting diodes (LEDs), photodetector, and X–ray scintillating imaging [82-89]. These 2D lead halide perovskites are categorized into (i) RP phase ($L_2A_{n-1}Pb_nX_{3n+1}$), (ii) DJ ($LA_{n-1}Pb_nX_{3n+1}$), and (iii) alternating cation interface (ACI), wherein L represents a spacer ligand; A is monovalent cation (A^+ = MA (CH_3NH_3), FA ($HC(NH_2)_2$), Cs); and X is halide (X^- = Cl, Br, I).[90-93] The increased complexity in 2D structure through modulating the layer thickness (*n*),

* Reprinted with permission from "Halide Ion Mobility in Paired 2D Perovskites: Ruddlesden–Popper Versus Dion–Jacobson" by S. Min, J. Cho *Advanced Optical Mater*. 2024, 12, 2302516. © 2024 Wiley–VCH GmbH. All rights reserved.

type of spacer ligand (L), binding mode (RP, DJ, and ACI), etc, allows for providing a rich, expanded design palette for controlling optoelectronic properties including bandgap, photoluminescence (PL) quantum yield, charge carrier lifetime, and halide stability. In particular, the coordination bonding nature of intercalated spacer ligands (L) (although do not directly affect the optoelectronic properties) can play a critical role in maintaining the stability of the 2D halide perovskites [101-109].

Importantly, a distinctive feature of lead halide perovskites is centered at a bandgap tunability tuned by halide compositions [97,110-115]. Tunable bandgap is essentially required for optimizing the light-harvesting properties in photovoltaics and light-emitting properties in LEDs. Halide ion (or even spacer cation) exchange across the colloidal perovskite nanocrystals, films, and bulk solids, thus, represents a convenient means for modulating the bandgap [97,98,116-119]. However, facile halide ion migration through soft perovskite lattices to form mixed halides gives rise to halide ion instability (or halide segregation) inversely.[99,113,120-124] Halide ion exchange is an entropically-driven process, and the exchange takes place until the final composition reaches the chemical equilibrium of halide composition throughout the system [117,125-128]. Therefore, recently, many research efforts

have been made toward suppressing the halide ion migration for stabilizing the perovskite lattices [98,112,127,129,130].

Halide ion mixing in low dimensional perovskites as compared to 3D perovskites remains underexplored owing to more stabilized perovskite lattices aided by intercalated spacer ligands [130-132]. The 2D perovskite structures resemble quantum well structures wherein the reduced dimensionality and the spacer ligands can bring about additional stabilization against moisture, heat, and external stimulus. Recently, Kamat and colleagues have investigated the important role of spacer ligands in stabilizing the 2D perovskites by mixing and segregating 2D perovskites with different spacer cations of linear BA and aromatic PEA.[97,100,118,133] Indeed, the intercalated ligands can serve as a halide migration barrier, and the aromatic spacer ligands are more effective than linear ones in terms of maintaining the stability of halides.[97,118,134,135] By tracking in-situ and ex-situ spectroscopic changes, a comprehensive understanding of the kinetics of halide ion migration and resulting stability across 2D *vs* 3D metal halide perovskites can be gained [97,100,118,133].

In this study, we have further elucidated the important role of binding mode determined by the coordinating nature of spacer ligands in 2D perovskites:

monodentate (BA) with RP versus bidentate (BDA) with DJ perovskites. We examined the important role of spacer ligands (BA vs BDA) as well as their binding mode (RP vs DJ) in maintaining the halide ion stability given halide mixing potential. Such difference in 2D crystallographic structures indeed brings about different degrees of halide ion mixing kinetics across the interface of the physically-paired 2D bromide and iodide perovskite films. This study provides a significant insight into the stability of halide perovskites and the design principle for achieving more stable low-dimensional perovskite optoelectronics.

III.2 EXPERIMENTAL

Materials.

n-butylammonium bromide (BABr, Greatcell Solar), *n*-butylammonium iodide (BAI, Greatcell Solar), butane-1,4-diammonium bromide ((BDA)Br_2, Greatcell Solar), butane-1,4-diammonium iodide ((BDA)I_2, Greatcell Solar), methylammonium bromide (MABr, Greatcell Solar), methylammonium iodide (MAI, Greatcell Solar), lead bromide ($PbBr_2$, 99.998% metal basis, Alfa Aesar), lead iodide (PbI_2, 99.9985% metal basis, Alfa Aesar), N,N-dimethylformamide (DMF, anhydrous 99.8%, Sigma-Aldrich), dimethyl sulfoxide (DMSO, anhydrous ≥ 99.9%, Sigma-Aldrich), fluorine-doped tin oxide conducting glass with 6~9 Ω/sq (FTO). All chemicals were used as received without additional purification.

Preparation of 2D Precursor Solutions.

It is important to note that the preparation of 2D bromide and iodide precursor solutions were entirely identical except for the halide precursors used. For preparation of Ruddlesden-Popper perovskites (n = 1), 0.3 mmol of BABr (or BAI) and 0.15 mmol of $PbBr_2$ (or PbI_2) was first dissolved in 1 mL containing 4:1 volumetric ratio of DMF:DMSO. For preparation of Dion-Jacobson perovskites (n = 1), 0.15mmol of (BDA)Br_2

(or (BDA)I_2 and 0.15mmol of $PbBr_2$ (or PbI_2) was dissolved in 1 mL containing 4:1 volumetric ratio of DMF:DMSO. All precursor solutions were stirred at ambient temperature in N_2-filled glovebox overnight.

Synthesis of 2D Perovskite Films.

Initially, FTO-coated glasses (2.5 cm x 2.5 cm) were cleaned with soapy water, followed by ultrasonication in mixed ethanol and deionized water for 15 min. Then, FTO substrates were treated with UV ozone for 20 min for surface activation. The substrates were immediately transferred to a N_2-filled glovebox for deposition of 2D perovskite films through spin-coating processes. A 30 μL of as-prepared RP (or DJ) precursor solutions was dropped on to the FTO film and subsequently spin-coated at 4000rpm for 25 sec. After 5 sec, 0.5 mL of chlorobenzene (acting as antisolvent) was rapidly injected into the FTO glass to induce the crystallization of 2D perovskite films. Then the perovskite films were transferred to pre-heated hot plate with 100 °C for 5 min.

Halide Ion Mixing with Paired 2D Perovskites Films.

The 2D lead bromide and iodide films were physically paired by clamping together with binder clips and transferred to a pre-heated hot plate with different heating temperatures (25-140 °C). To directly heat the

physically-paired films, aluminum plates were placed on top and bottom of the paired perovskite films. The clamped films were periodically checked during halide ion mixing process by measuring UV-vis absorption spectra. Noting that halide ion mixing experiments were conducted in ambient air condition if not stated since the halide mixing kinetics can be influenced by atmospheric condition (N_2 or air).

Preparation and Halide Ion Mixing with Paired Quasi-2D (n = 10) and 3D (n = bulk) Perovskite Films.

Quasi-2D and 3D bromide and iodide perovskite films were also prepared to test halide ion exchanges. For 3D perovskite preparation, 0.6 mmol of MABr (or MAI) and 0.6mmol of $PbBr_2$ (or PbI_2) were dissolved in 1 mL of 4:1 volumetric ratio of DMF:DMSO mixture. Other process for synthesis of 3D films were identical with those of 2D films described earlier. To prepare quasi-2D perovskites (n = 10), as-prepared 3D perovskite solution and 2D perovskites solution were stoichiometrically mixed to yield $(BA)_2MA_{n-1}Pb_nX_{3n+1}$ for RP and $(BDA)MA_{n-1}Pb_nX_{3n+1}$ for DJ. In the case of n = 10, the ratio between as-prepared 3D perovskite (MA, Pb, and X) and 2D perovskite (containing spacer, Pb, and X) is 9:1 regardless of the binding mode according to following equations 1,2. Overall, the 180 μL of 0.6 M Pb (3D precursor solution) and 80 μL of 0.15 M Pb (2D

precursor) perovskites solutions were homogeneously mixed at room temperature by stirring over 2−3 hr. Quasi−2D perovskites films were also synthesized following the same procedure as described in 2D and 3D perovskites (annealing at 100 °C for 5 min).

In the case of n = 10 (quasi−2D)

$9MAPbX_3 + (BA)_2PbX_4 \rightarrow (BA)_2MA_9Pb_{10}X_{31}$ (X = Br, I) (equation 1)

$9MAPbX_3 + (BDA)PbX_4 \rightarrow (BDA)MA_9Pb_{10}X_{31}$ (X = Br, I) (equation 2)

Characterizations.

Steady State Absorption Measurements.

Absorption spectra were recorded using a Varian Cary 60 spectrometer in the wavelength of 350−800nm with a scan rate 4800 nm/min for 2D lead halide perovskites films. The difference absorption (⊿A) spectra were acquired by subtracting the absorption spectrum at zero time (0 min; serving as a reference) from the absorption spectra collected at longer time

Photoluminescence (PL).

Photoluminescence measurements were made using JASCO FP−8550 spectrofluorometer in the wavelength of 380−600 nm for the perovskites films. Excitation wavelength was set to be 365 nm with a 0.5 nm of scan

step size, a 0.1 sec of dwell time, and a slit width of 10 nm for emission measurements.

Scanning Electron Microscopes (SEM).

Field emission scanning electron microscope (SEM) images were taken using a JEOL Ltd. JSM-7500F operated at an accelerating voltage of 10 kV. Top-down view and cross-section SEM images were collected using the 2D samples.

Powder X-ray diffraction (XRD)

Powder X-ray diffraction (XRD) measurements were performed using a Bruker D8 Focus X-ray Powder Diffractometer with a Cu Kα radiation source (λ = 1.5406 Å) in the 2θ range from 5-45°.

Determination of Bandgap in the Mixed Halides.

Tauc plots were obtained by converting the absorption spectra with the equation of $(\alpha h\nu)^2$ versus $h\nu$ for the directly-allowed transitions materials. The straight line was extrapolated onto *x*-axis to determine the bandgap (E_g). Halide ion compositions in the mixed halide were further analyzed in consideration of the bandgap of pure bromide and iodide perovskites, respectively, that is also determined from the *Tauc* plots. A

simple Vegard’ s law with a linear interpolation is used to determine the halide composition in the mixed halide perovskites.

III.3 RESULTS AND DISCUSSION

Mixed Halide Stability in 2D RP and DJ Perovskites under Ambient Condition.

The 2D perovskite films with bromide and iodide with RP and DJ phases, respectively, are prepared through a spin-casting process, following previously reported methods (details on the preparation are found in the Supporting Information).[99,136] In this study, a similar chain length of C4 (butane) ligands is used: monodentate spacer ligand of BA with a length of 5.0 Å for yielding RP versus bidentate spacer ligand of BDA with a length of 6.2 Å for stabilizing DJ phase, respectively (**Figure Ⅲ.1A,B**). Hereinafter, we denote the $(BA)_2PbBr_4$ to be BA(Br), $(BA)_2PbI_4$ to be BA(I), $(BDA)PbBr_4$ to be BDA(Br), and $(BDA)PbI_4$ to be BDA(I), respectively, throughout the entire manuscript for simplicity.

To access the halide ion stability (or mobility) in 2D RP and DJ perovskites, we have paired two different halide perovskite films and annealed them at various reaction temperatures (25-140 °C) [98,117,125]. **Figures Ⅲ.1C,D** contrasts the absorption spectra changes over time (for 2880 mins) for the paired 2D bromide and iodides films: denoted as paired BA(Br)|BA(I)

with RP phase versus BDA(Br)|BDA(I) with DJ phase, respectively. Insets of **Figure Ⅲ.1C,D** displayed physically-clamped Br and I films, respectively, left at room temperature (RT). Before pairing, initial 2D films are characterized with a pronounced band-edge absorption peak around 400 nm (BA(Br)), 510 nm (BA(I)), 390 nm (BDA(Br)), and 492 nm (BDA(I)), respectively. Interestingly, 2D DJ perovskites show a little bit of increased bandgap (~ 0.1-0.2 eV) as compared to 2D RP perovskites with the same halide compositions. This is associated with the change in the degree of dielectric confinement with different spacer ligands [137]. To understand halide composition-dependent bandgap changes, we also directly synthesized BA- and BDA-based perovskites films with mixed halides by initially weighing out different halide compositions of Br:I = 100:0, 75:25, 50:50, 25:27, and 0:100, respectively. Absorption spectra of these films were recorded using a FTO and a glass substrate, respectively (**Figures A.11A-D**). Noting that absorbance in the range of 450-550 nm on a FTO substrate is owing to FTO artifacts, which is not shown in the sample on a glass. Absorption spectra of a FTO and a glass along with baseline correction are shown in (**Figure A.11E,F**). Corresponding PL emission spectra for those films with different halide compositions were recorded (**Figures A.11G,H**). Notably, BA-based

perovskite films show distinctive PL emission as a function of halide composition whereas BDA−based perovskite films show very weak PL

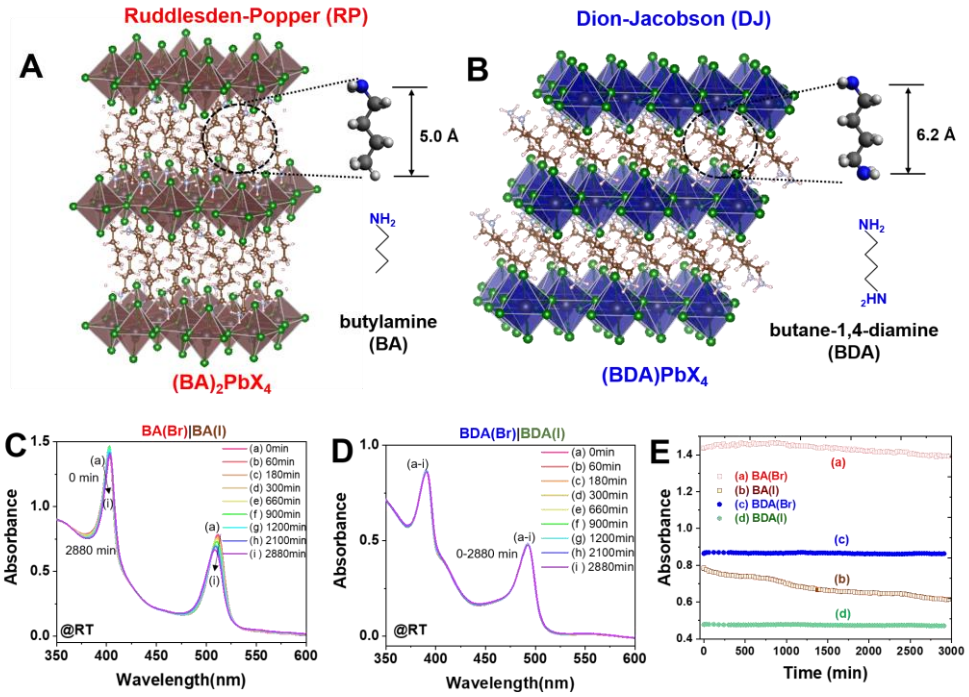

Figure III.1. (A,B) Crystallographic structures of 2D perovskites: (A) Ruddlesden−Popper perovskites using butylamine (BA) and (B) Dion−Jacobson perovskites using butane−1,4−diamine. (C,D) Absorption spectra changes recorded at room temperature (RT; 25 °C) for the physically paired 2D lead halide (X = Br, I) perovskite films with BA (RP) and BDA (DJ), respectively, on a FTO substrate in air. (E) Absorbance changes over time by tracking the absorbance at bromide peak (at 390−400 nm) and iodide peak (at 490−520 nm) for the paired 2D lead bromide and lead iodide perovskites films, respectively, as shown in panel 1C and 1D.

emission except BDA(Br). This is probably associated with a high defect density seen in BDA-based perovskites which can be shown in SEM and XRD (*vide infra*).

Bandgap of 2D perovskites can be further determined by Tauc plots (**Figure A.12A-C**), indicating that the bandgap shifted from 3.25-2.55 eV (for BDA) and from 3.16-2.44 eV (for BA), respectively, as a function of increasing iodide (or decreasing bromide) composition in the mixed halides (**Figure A.12C**). **Figure Ⅲ.1E** displays the change in the absorption intensity changes over time by tracking the Br (390-400 nm) and I (500-520 nm) peaks, respectively, for 2D paired perovskite films, shown in panels of **Figure Ⅲ.1C,D**. Notably, absorption intensities of both BDA (X = Br, I) were retained over time while these values decreased in both BA (X = Br, I) perovskites. Hence, it is important to note that there is significant halide ion mixing occurring in 2D BA-based perovskites (RP) even at room temperature while the halide ion mixing is entirely suppressed in BDA-based perovskites (**Figure Ⅲ.1E**). These changes can be seen more apparent in the difference absorption spectra (**Figure A.12A,B**). Given the halide mixing potential and halide concentration gradient across the paired films, different halide compositions of 2D perovskite films (Br and I) get mixed through the interface of 2D

perovskite films (RP vs DJ).

Halide Ion Migration Kinetics in Paired 2D Perovskite Films.

To understand thermally-activated halide ion migration across the interface of the 2D paired Br|I films, we have recorded absorption changes at different temperatures ranging from 25-140 °C. As shown in the absorption and PL emission spectra of **Figure A11.A-D,** each BA- and BDA-based films (bromide and iodide), exhibited distinctive excitonic features, respectively. **Figure Ⅲ.2A** demonstrates a schematic illustration of the paired BA(Br)|BA(I) films that is thermally heated using a temperature-controlled hot plate in air. As a representative example,

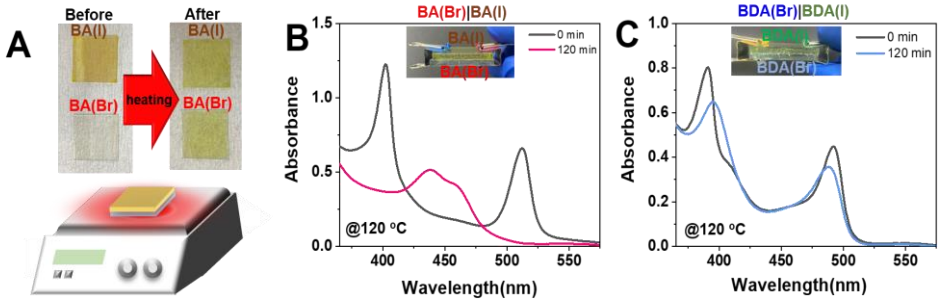

Figure III.2. (A) Schematic illustration (bottom) of thermal heating of paired 2D lead bromide and iodide films on a FTO substrate using temperature-controlled hot plate and digital photograph (top) of BA(I) and BA(Br) film before and after heating at 120 °C for 120 min in air. (B,C) Absorption spectra recoded at 0 min (before heating) and after heating at 120 °C for 120 min: (B) 2D paired BA(Br)|BA(I) and (C) 2D BDA(Br)|BDA(I) films.

Figures Ⅲ.2B,C show the absorption changes recorded at a higher temperature of 120 °C for these paired perovskite films.

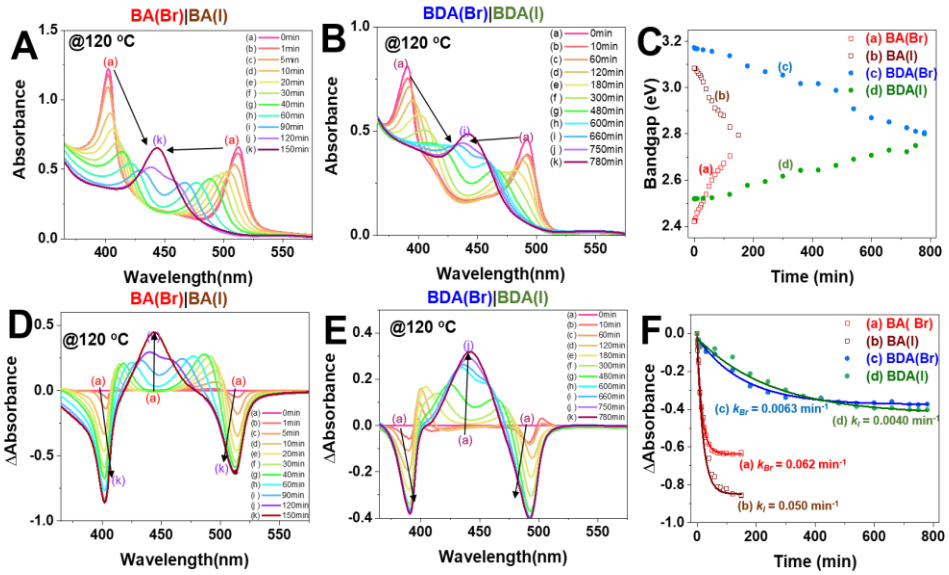

Figure III.3. (A,B) Time-dependent absorption spectra recorded for the paired 2D RP (BA; 3A) and DJ (BDA; 3B) films on a FTO substrate upon heating at 120 °C in air. (C) Change in bandgap of each film. (D,E) Difference absorption spectra corresponding to panel 3A and 3B, respectively. (F) Kinetic trace and fitting by tracking the band-edge peak of BA(Br), BA(I), BDA(Br), and BDA(I), respectively, as shown in difference absorption spectra during heating at 120 °C.

As seen from halide ion stability and mobility at room temperature, it is noticeable that 2D BA-based perovskites films show two different absorption peaks almost merged after heating for 2 hr (Figure 2B) whereas the 2D BDA-based perovskites films maintained the initial band-edge absorption peaks even heating for same time (Figure 2C). It is also

very important to note that halide ion migration kinetics can be somewhat affected by an atmosphere condition (more specifically halide defect concentration controlled by atmospheric gases).[138] Noting that all of these spectroscopic measurements for mixing were mainly conducted in ambient air conditions unless otherwise stated.

To understand these effects, a control experiment for mixing was performed in a controlled glove box filled with inert gas of N2 that will be further discussed later (vide infra). Digital photographs taken for BA perovskites before and after heating also attest that initial BA(Br) with white and BA(I) with dark orange changed to the same color (both greenish) upon mixing **(Figure Ⅲ.2A)**. To observe time-dependent absorption changes shown in Figures 2B,C, we have further recorded the absorption changes for physically paired 2D perovskite films until halides entirely get mixed at 120 °C. Figures 3A,B depict the time-dependent absorption changes seen in such 2D BA(Br)|BA(I) and BDA(Br)|BDA(I) films, respectively. By tracking time-dependent absorption peak shift (corresponding to halide-dependent bandgap), it was able to understand halide ion exchange kinetics across the 2D perovskite films **(Figure Ⅲ.3C)**. Strikingly differently, mixing of BA perovskites requires 150 min for completion whereas it takes 780 min for entire halide ion mixing in the

BDA perovskites (Figures Ⅲ.3A,B). Figures A.14A,B show the digital photograph of each film BA(Br), BA(I), BDA(Br), and BDA(I) before (0 min) and after entirely mixed, and corresponding identical PL emission spectra for these fully mixed perovskite films. The PL emission spectra from the mixed phase of 2D perovskites were identically each other, which cannot be seen in PL emission spectrum of directly-synthesized Br:I = 50:50 films, exhibiting intrinsically segregated halide phases, in line with previous report [139]. (Figures A.14C,D and A.11G,H). This result suggests that post-synthetic halide ion homogenization through the thermal annealing provide an alternative route to access homogeneously mixed 2D perovskites. To better visualize such spectroscopic changes, difference absorption spectra were obtained by subtracting the absorption recorded at a longer time from the absorption recorded at 0 min (Figures 3D,E). In both 2D films (RP and DJ phase), the absorption peak intensity corresponding to 380-400 nm (for Br) and 480-520 nm (for I) decreased gradually, suggesting that parents Br and I are consumed to produce mixed halides that can be expressed in equations (1-2).

$$(BA)_2PbBr_4 + (BA)_2PbI_4 \rightarrow (BA)_2Pb(Br_{0.5}I_{0.5})_4 \quad \textit{for RP phase} \qquad (1)$$

$$(BDA)PbBr_4 + (BDA)PbI_4 \rightarrow (BDA)Pb(Br_{0.5}I_{0.5})_4 \quad \textit{for DJ phase} \qquad (2)$$

The difference in halide composition (halide concentration gradient) in these paired films drives the halide mixing due to entropic stabilization. Figure A.15A,B depict the band-edge wavelength changes over time for BA and BDA-perovskites films, respectively. As a result of halide ion mixing, the mixed halide peak with Br:I = 50:50 appeared around 440-450 nm with different mixing timescales for BA and BDA-based perovskites (Figures Ⅲ3.A,B). The mixed halide peak emerging at 440-450 nm is matched with the halide composition of Br:I = 50:50. (Figures A.11A,B). The disappearance kinetics of parent 2D bromide films are further tracked and fitted using a monoexponential function to understand mixing kinetics (Figure Ⅲ.3F). A pseudo-first-order kinetic rate constant (k) was obtained with 0.050-0.062 min^{-1} (for BA(Br, I)) and 0.0040-0.0063 min^{-1} (for BDA(Br, I)) (Figure Ⅲ.3F). Such huge differences in kinetic rate constants between RP and DJ perovskites by an order of magnitude imply that halide migrations are more facilitated in RP perovskites than in DJ perovskites at given condition (same thermal activation and same carbon chain length).

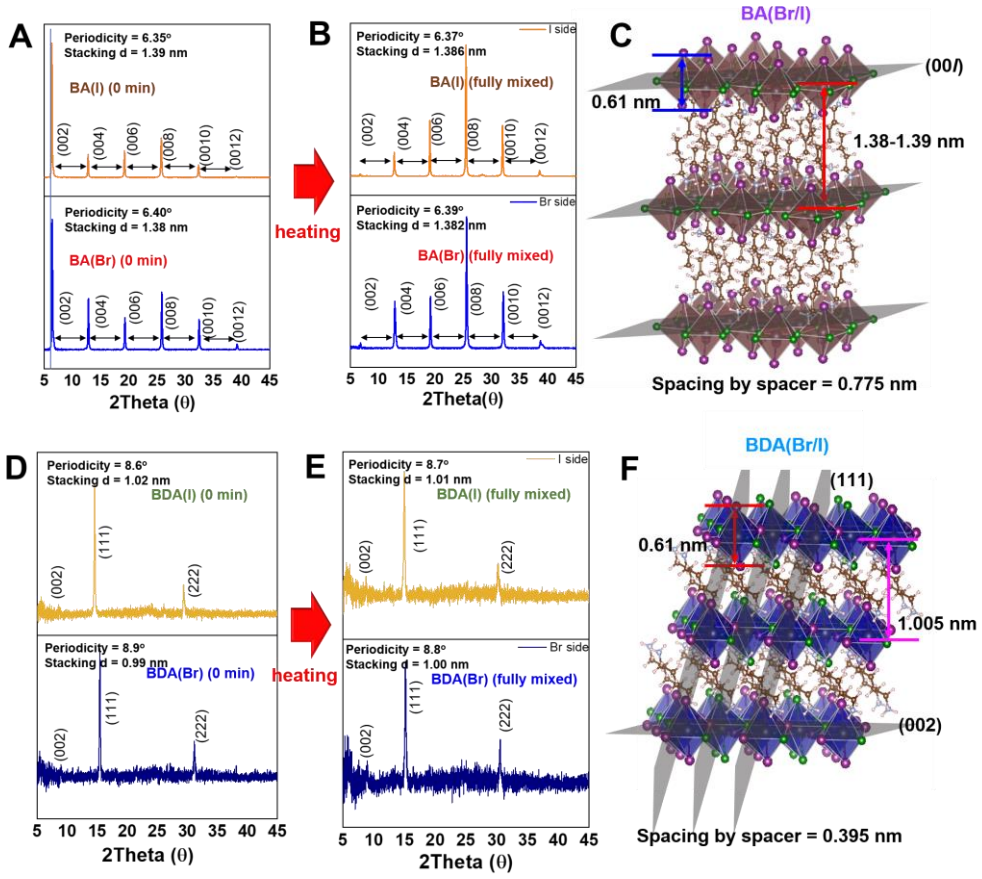

Figure III.4. (A,B) XRD patterns obtained before (0 min; A) and after mixing (fully mixed; B) with BA(Br) and BA(I) on a glass substrate. (C) Crystallographic structure of fully mixed BA perovskites (Br/I). (D,E) (A,B) XRD patterns obtained before (0 min; D) and after mixing (fully mixed; E) with BDA(Br) and BDA(I) on glass substrate. (F) Crystallographic structure of fully mixed BA perovskites (Br/I). Spacing by ligand is calculated by subtracting the length of lead octahedral from the stacking distance.

To characterize the structural changes during the halide ion exchange, we have measured XRD and SEM for 2D films before and after mixing, respectively. **Figures Ⅲ.4A,B** and **A.16A,B** demonstrate XRD patterns

obtained on glass and FTO substrate, respectively, before (Ⅲ.4A and A.16A) and after mixing (Ⅲ.4B and A.16B) for BA-based perovskites.

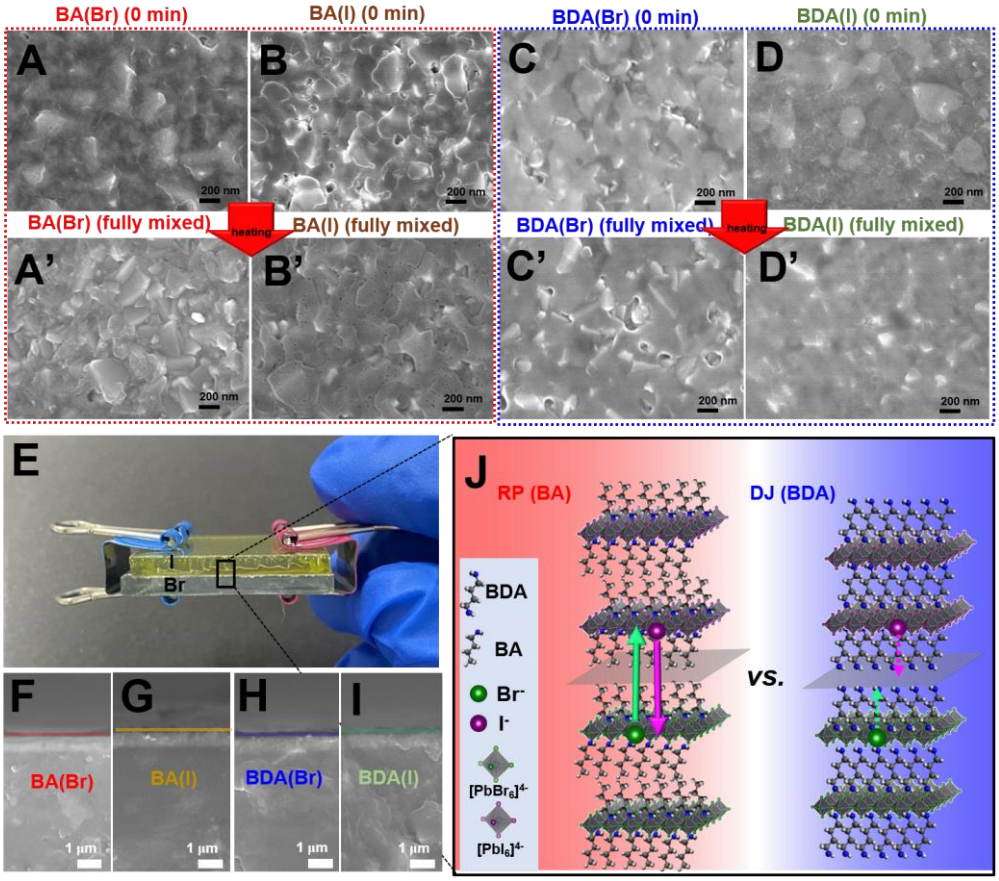

Figure III.5. (A,B) XRD patterns obtained before (0 min; A) and after mixing (fully mixed; B) with BA(Br) and BA(I) on a glass substrate. (C) Crystallographic structure of fully mixed BA perovskites (Br/I). (D,E) (A,B) XRD patterns obtained before (0 min; D) and after mixing (fully mixed; E) with BDA(Br) and BDA(I) on glass substrate. (F) Crystallographic structure of fully mixed BA perovskites (Br/I). Spacing by ligand is calculated by subtracting the length of lead octahedral from the stacking distance.

The 2D layer stacking in crystallographic structure with a periodical repetition was determined based upon a periodicity in 2 theta angle along (00*l*) planes (**Figure Ⅲ.4C**). Initial periodicity for BA(Br) of 6.40° and BA(I) of 6.35° homogenized to the intermediate value of 6.39°–6.37°, mirroring the spectroscopic observations (**Figure Ⅲ.3A**). When converting 2 theta angle (°) to distance (nm), the interlayer spacing of BA(Br) of 1.38 nm and BA(I) of 1.39 nm films was changed to an identical length after entirely mixed (1.382–1.386 nm) (**Figure A.17 and Ⅲ.4C**). Similar phenomena were observed for BDA films during the halide ion mixing (**Figures Ⅲ.4D,E and A.18A,B**). Notably, XRD patterns collected on both glass and FTO were distinctive with enhanced reflection peaks on (111) and (222) instead of (00*l*) reflections for DJ perovskites, consistent with previous publications (**Figure Ⅲ.4F**) [103,140]. However, clear reflection on (002) plane allows for a determination of interlayer spacing to be 0.99–1.02 nm for BDA(Br) and BDA(I) that are changed to an identical number of 1.005 nm for mixed halides (BDA(Br/I) (**Figure A.19 and Ⅲ.4F**).

Figure Ⅲ.5A–D and Ⅲ.5A’–D’ shows SEM images of BA(Br), BA(I), BDA(Br), and BDA(I), before (5A–D) and after mixing (5A’–D’), respectively.

Overall, each 2D films were characterized by 2D flakes owing to the growth nature in a 2D manner. Despite thermal heating, there are no significant morphological changes during halide ion migration and mixing. If the halide ion migration occurs through the solid-state interface, the halide migration kinetics are also determined by the Fickian second diffusion laws (**Figure Ⅲ.3E** and equation 3).

$$\frac{dC}{dt} = D\,\frac{d^2C}{dx^2} \qquad (3)$$

where C is the halide concentration; t is the time; D is the diffusion coefficient; x is the diffusion distance.

As diffusion kinetics is dictated by concentration gradient as well as diffusion distance, we have measured the cross-sectional SEM images for each film (**Figure Ⅲ.5F-I** and **Figure A.20A-D**) to determine the diffusion pathlength. Cross-section SEM images can reveal the average thickness of the film, corresponding to the halide ion migration pathlength, was determined to be 122 ± 20 nm, respectively. Each thickness of 2D films is summarized in **Figure A.20E**. In this scenario, given the similar halide concentration gradient and diffusion length, the halide diffusivity or kinetics is more governed by the diffusion coefficient of materials that is also strongly dependent on the binding mode.

Figure Ⅲ.3J illustrates the schematic demonstration for interfacial halide ion migration and resulting mixing across the halide concentration gradient of the paired 2D films. Taking into account the random orientation and growth of the 2D flakes, overall halide ion mobility was governed by the inherent crystal structures (DJ vs RP). Increased halide stability in DJ is associated with increased rigidity in the frameworks that are maintained by the bidentate binding of spacer ligand BDA. On the other hand, softer frameworks comprised of monodentate BA with only van der Waals gap give rise to facile lead octahedral distortion-induced halide vacancy formation, which can induce the halide ion migration (well-known vacancy-mediated halide migration), following Vacancy-mediated diffusion coefficient (equation 4) [141].

$$D = fa^2 C_v b \qquad (4)$$

where f is the jump correlation factor; a is the lattice parameter; C_v is the vacancy concentration; b is the atom jump frequency.

Activation Energy for Halide Mixing in 2D Perovskites.

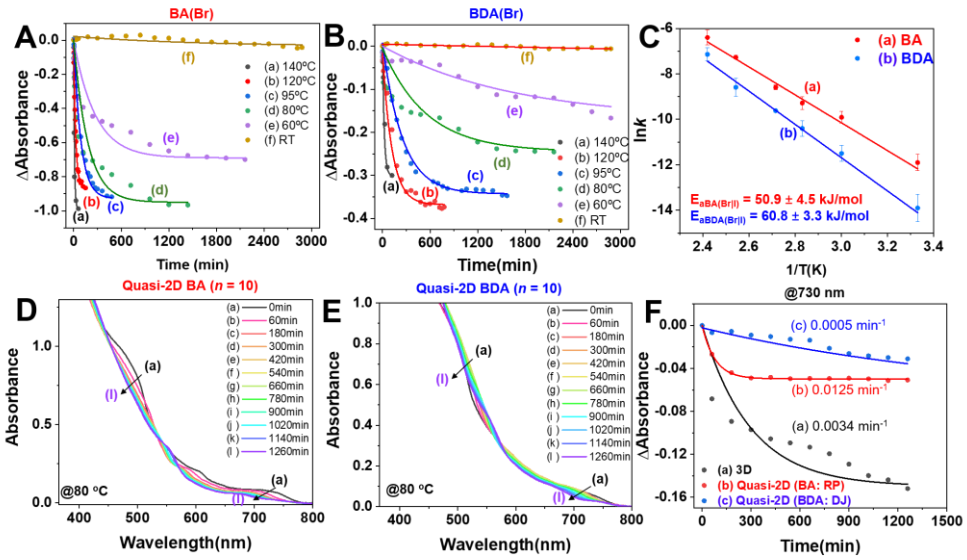

Figure III.6. (A,B) Kinetic trace and fitting obtained from difference absorption spectra over 2D paired bromide and iodide films on a FTO substrate by tracking the bromide peak at 390−400 nm for BA (A) and for BDA (B) recorded at various reaction temperatures from 140−25°C in air. (C) Arrhenius plots validating ln(k) versus inverse temperature (1/T) relationship for these 2D perovskite films with activation energy of halide mixing. (D,E) Absorption spectra changes recorded for the paired quasi−2D bromide and iodide perovskite films (n = 10) with RP (BA: 4D) and DJ phase (BDA: 4E) upon heating at 80 °C. (F) Kinetic traces and fitting obtained from the difference absorption spectra at 730 nm upon heating at 80 °C.

To gain a better understanding of the suppressed halide ion migration in BDA (DJ) perovskites, we have further conducted temperature−dependent studies for halide mixing at different reaction temperatures of 140, 95, 80, and 60 °C, respecitvely. Corresponding evolution of absorption

and difference absorption spectra at given temperatures are depicted in **Figure A.21A–H** (BA) and **Figure A.22A–H** (BDA), respectively. **Figures Ⅲ.6A,B** summarized the change seen in different absorption spectra by tracking the Br peak (390–400 nm) of paired 2D films. With increasing the reaction temperatures from 25–140 °C, it can be seen that the kinetic rate constant (k) for mixing increased from 6.7 x 10^{-6} – 1.6 x 10^{-3} sec^{-1} (for BA) and from 8.3 x 10^{-7} – 7.9 x 10^{-4} sec^{-1} (for BDA–based perovskites). Given the same thermal activation, the rate constants for mixing of DJ perovskite films is an order of magnitude lower than those of RP perovskites. Diammonium cation can immobilize the 2D perovskite layer by attaching the top and bottom of 2D sheets (**Figures Ⅲ.1A,B**). By fitting with pseudo–first–order kinetics, we can obtain the rate constant at different temperatures and calculate the activation energy using the Arrhenius equation (equation 5).

$$ln\,(\mathrm{k}) = -\mathrm{Ea/RT} + ln\,(\mathrm{A}) \qquad (5)$$

where k is the rate constant; E_a is the activation energy; R is the universal gas constant; T is kelvin temperature; and A is the pre–exponential factor. The calculated activation energy for halide mixing in 2D perovskites is 50.9 ± 4.5 kJ/mol (for BA) and 60.8 ± 3.3 kJ/mol (for BDA), respectively (**Figure Ⅲ.6C**). The increased activation energy (or energy

increment around 10 kJ/mol) for BDA is associated with the two-fold increase in hydrogen bonding as a result of bidentate spacer ligands employed in 2D perovskite crystal structures. The diamine group of space ligands can interact with halide ions through hydrogen bonding, stabilizing the perovskite lattices as described in **Figures Ⅲ.1A,B.** Recently, we also investigated the halide mixing across colloidal 2D RP perovskites using only different spacer ligands of aromatic phenethylammonium (PEA) and aliphatic BA. Halide ion mixing activation energy was reported to be 75.3 (PEA) and 57.8 kJ/mol (BA), respectively. The increased activation energy for PEA-based perovskites even with the same binding mode of RP is closely associated with the increased rigidity of frameworks as a result of $\pi-\pi$ interaction between aromatic ligands.[97] Similarly, a binding mode within 2D perovskites dictates the chemical interaction between the spacer ligand and inorganic sheet, affecting the halide ion activation energy. Importantly, in the case of DJ perovskites with increased defect densities (or halide vacancies) as seen from XRD and SEM, intrinsic crystal structures comprised of bidentate amines can dictate the overall halide ion migration kinetics (and stability).

It is also important to note that an atmospheric condition (which definitely affects the defect concentration) plays a critical role in determining the

halide ion diffusion kinetics. It has been well known that 3D halide perovskites can indeed interact with oxygen molecules that can further incorporate into crystal structures. Simultaneously, generated halide vacancy concentration shows somewhat a linear correlation with a partial oxygen pressure [138]. As indicated in equation (4), the halide diffusion coefficient is dictated by halide vacancy concentration (C_v). To understand the role of oxygen in halide ion exchange in 2D perovskites, we have conducted a control mixing experiment at 140 °C in a glove box entirely filled with N_2 (oxygen < 5−10 ppm). **Figures A.23A−F** exhibit the absorption and difference absorption spectra recorded for paired BA−based (S13A,C,E) and BDA−based bromide and iodide (S13B,D,F) films. Noticeably, it takes much longer times for mixing in N_2 condition as compared to in air for both BA and BDA−based films (**Figures A.23E,F**). The rate constant determined from kinetic fittings was 8.9 x 10^{-3} sec^{-1} (BA) and 7.9 x 10^{-4} sec^{-1} (BDA), respectively. Thus, we can conclude that gas condition (such as air or N_2) also strongly influences the surface passivation and defect formation, which ultimately governs halide ion mixing kinetics that should be taken into account for halide stability.[138,142,143]

In addition to O_2, infiltration of ambient water molecules into perovskite lattices affects halide ion migration kinetics as well. Recent studies reveals

that even with 2D perovskite layer protection on 3D perovskites, water molecules can incorporate into the perovskite structures, inducing structural degradations and disproportionation of initial 2D phase into lower number 2D structures.[144,145] We also have examined the substrate effect on halide mixing at 80 °C as a representavie example using either a FTO or a glass (control) as shown in **Figures A.24A–F.** There is no significant difference in halide mixing kinetic rate constants (~10^{-5} sec^{-1} for BA and ~10^{-6} sec^{-1} for BDA –based perovskites), suggesting that halide ion mixing is rather governed by the binding mode.

Halide Mobility in Quasi–2D Perovskites.

To further probe our idea that DJ perovskites are more effective than RP perovskites in stabilizing the halides, we have expanded to quasi–2D perovskites (which are further compared with 3D perovskites). By pairing the two different quasi–2D bromide and iodide films (with the same n = 10), we examined the halide ion stability given temperature (at 80 °C). **Figure A.25** shows UV–vis absorption spectra for 3D $MAPbX_3$ (with n = bulk) and quasi–2D perovskites films with n = 10 (X = Br, I) including BA and BDA as spacers, respectively (details for the preparation of quasi–2D are shown in the experimental section). Previous studies demonstrated that thermally–induced halide ion migration was influenced by layer

number (n) of inorganic slab across 3D−2D perovskites. With reducing the dimensionality of the perovskite layer, the activation energy of halide ion migration increased.[99,129] It has been known that halide ion migration is more facilitated in 3D halide perovskites owing to interconnected $[PbX_6]^{4-}$ lead octahedral frameworks. **Figures Ⅲ.6D,E** and **Figures A.26A−D** show the absorption changes of paired quasi−2D perovskites (with n = 10) and 3D perovskite films upon heating at 80 °C. **Figure Ⅲ.6F** summarized such changes in difference absorption spectra by monitoring at 730 nm for quasi−2D BA (n = 10), quasi−2D BDA (n = 10), and 3D (n = bulk). Notably, the quasi−2D with DJ phase (k: 0.0005 min^{-1}) shows sluggish halide migration than RP perovskites (k: 0.0125 min^{-1}). Considering the halide ion migration is closely related to the halide vacancy formation (or defect density) dominantly (equation 4), introducing the protective 2D perovskites layers atop 3D perovskites or making quasi−2D perovskites with DJ phases (bidentate ligands) provide better halide stability given similar halide diffusion length, crystallinity, grain boundary, halide defect density, and concentration gradient of mixing. In particular, bidentate spacer ligands can provide two−fold increased hydrogen bonding with halide ions as manifested in DJ phases, allowing for coordination on top and bottom of inorganic lead octahedral layers, thus more stabilizing 2D

perovskite lattices.

III.3 CONCLUSION

Halide ion mixing across physically-paired 2D perovskites with RP (BA) and DJ (BDA) perovskites were examined to understand the halide ion stability in different binding modes of 2D perovskites. The 2D layered perovskites are known as more stable than 3D perovskites with increased stability. However, given halide mixing potential, halide ion exchange occurs even at room temperature with BA-based perovskites. Temperature- and layer thickness-dependent studies probe that the mixing of halide anions in DJ (BDA) occurs at an order of magnitude slower than that in RP (BA). The increased activation energy for halide mixing in DJ perovskites as compared to RP perovskites is associated with the multidentating nature of spacer ligands as well as increased hydrogen bondings. Therefore, the binding mode of spacer ligands in 2D structure governs the rigidity of lead octahedral framework, halide vacancy formation, and halide stability (or mobility). Such understanding and engineering the crystallographic structure of the 2D perovskites is essentially required to achieve optoelectronic devices with better stability and performance.

IV. Dissertation Summary and Conclusions

Importantly, we have studied the structure−properties (optoelectronic properties) correlation of lead halide perovskites across 3D) to two−dimensional (2D) perovskite films using kinetic studies.

In Chapter Ⅱ, we have investigated the effect of chemical bonding of Pb−X in octahedral $[PbX_6]^{4-}$ dictated by the type of halide ions on $CsPbX_3$ nanocrystals growth kinetics (transformation to bulk film). The activation energy for growth of 3D lead halide nanocrystals obtained by temperature−dependent study is 93kj/mol for CsPbCl3 and 72J/mol for CsPbI3. This result indicated that ionic bonding of Pb−Cl leads the faster transforming to bulk crystals compared to covalent bonding (less ionic bonding) of Pb−I.

In ChapterⅢ, we have explored halide ion mobility (stability) in Ruddlesden−Popper phase (RP) and Dion−Jacobson (DJ) phase of 2D lead halide perovskites synthesized on film substrates. Temperature, and thickness− dependent spectroscopic studies probe that halide (bromide and iodide) ions migration kinetics is dictated by binding modes (RP vs DJ): halide ions are facilely migrated and mixed in RP phase than DJ phase. Each activation energy of RP and DJ phase obtained by temperature−dependent study indicates the rigidity of $[PbX_6]^{4-}$ octahedral framework

determined by binding mode of organic spacer cation. We can conclude the bonding nature DJ phase with increasing hydrogen bondings are more stable in terms of halide vacancy formation and ion migration.

In summary, through control of halide ion migration kinetics or growth kinetics, we can control the size-dependent optoelectronic properties such as bandgap, emission wavelength and charge carrier recombination kinetic. Also, kinetic study of halide ion migration in 2D lead halide perovskites with RP or DJ phase, is essentially required to understand the halide ion stability in crystal structures. Such kinetic studies using 3D and 2D perovskites provide significant insight into engineering and designing the lead halide perovskites nanocrystals synthesis with more desirable optoelectronic properties and stability. Since the optoelectronic properties of lead halide perovskites (band gap, emission wavelength and carrier recombination dynamics) depends on particle size, layer thickness, and spacer ligand variation, consequently , this study provides strategies to achieve lead halide perovskites based optoelectronic devices with better performance and stability.

APPENDIX A

SUPPLEMENTARY FIGURES AND TABLES

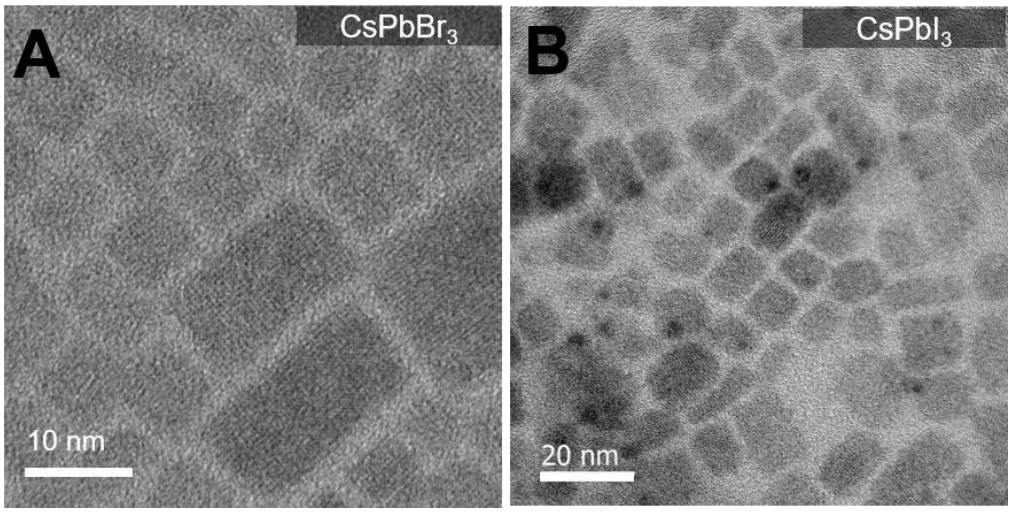

Figure A.1. TEM images for $CsPbBr_3$ (A) and $CsPbI_3$ nanocrystals (B).

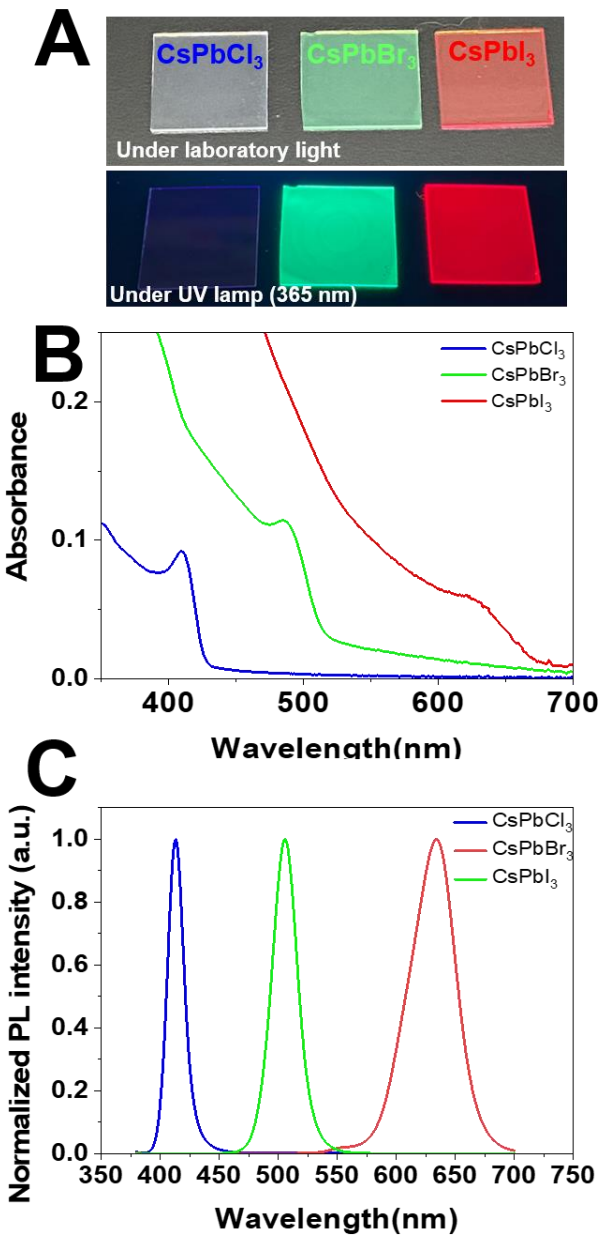

Figure A.2. (A) Digital photographs under laboratory light and UV lamp (365 nm), (B) absorption spectra, and (C) emission spectra for $CsPbCl_3$, $CsPbBr_3$, and $CsPbI_3$ nanocrystal films deposited on glass substrates, respectively.

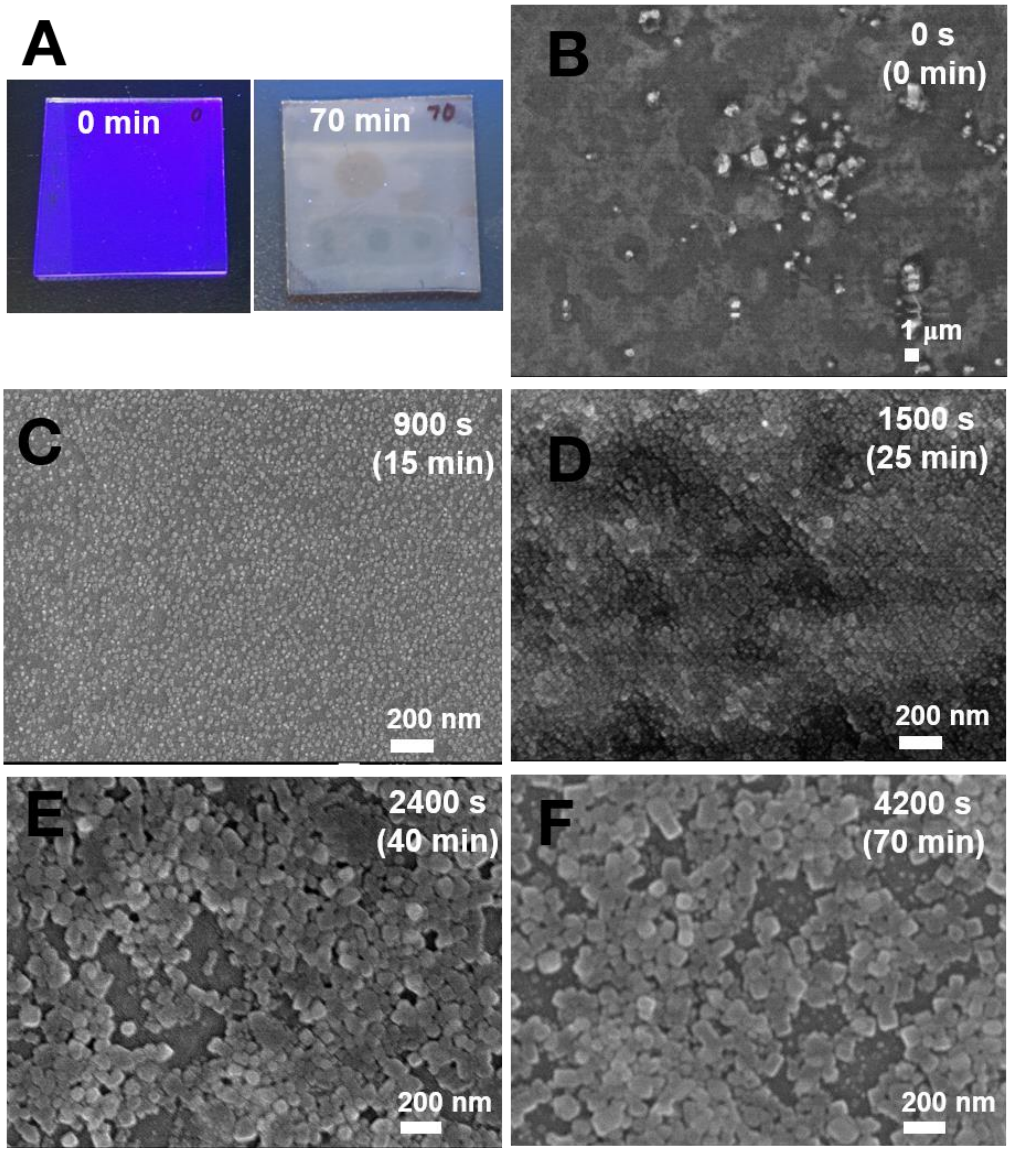

Figure A.3. (A) Digital photograph under 365 nm UV excitation for $CsPbCl_3$ film annealed for 0 and 70 min. (B–F) SEM images for $CsPbCl_3$ films annealed at 130 ^{o}C for different annealing time from 0, 15, 25, 40, 70 min, respectively.

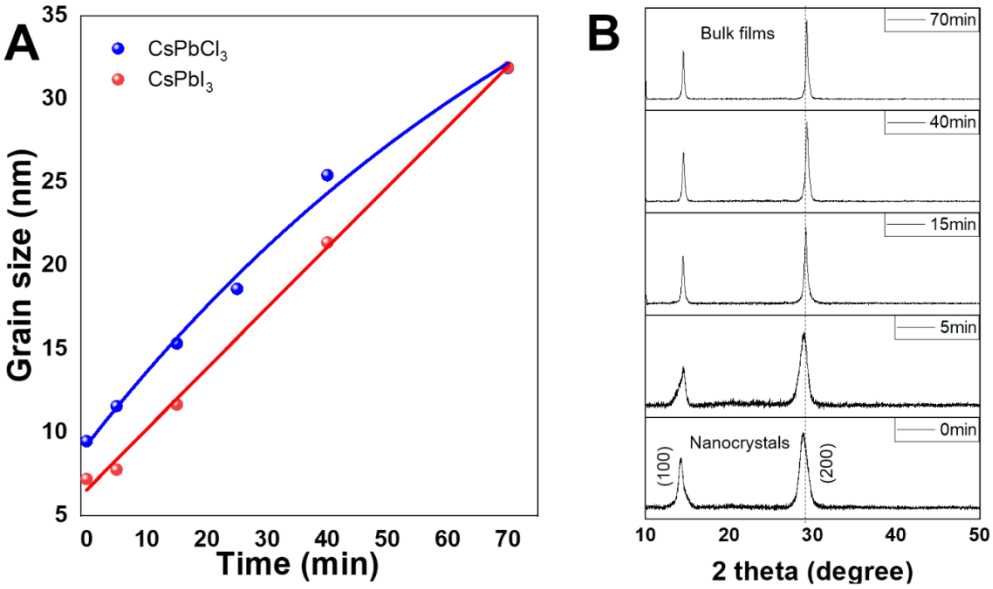

Figure A.4. (A) Grain size changes determined from the XRD patterns using Scherrer equation for $CsPbCl_3$ and $CsPbI_3$ nanocrystal films annealed at 130 °C for 70 min. (B) XRD pattern evolution during the course of annealing for $CsPbI_3$ films annealed at 130 °C for 70 min.

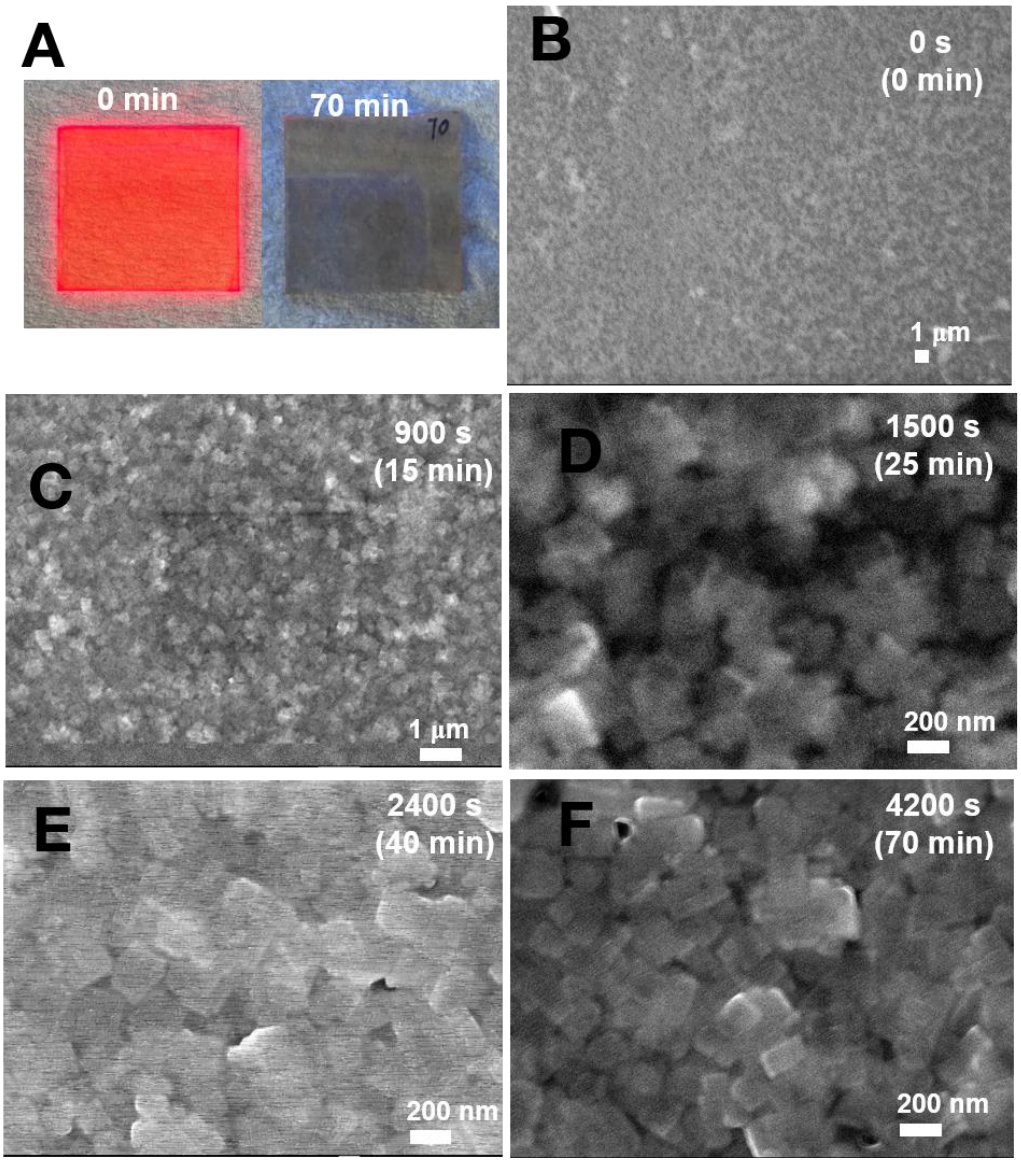

Figure A.5. (A) Digital photograph under 365 nm UV excitation for CsPbI3 film annealed for 0 and 70 min. (B–F) SEM images for CsPbI3 films annealed at 130 oC for different annealing time from 0, 15, 25, 40, 70 min, respectively.

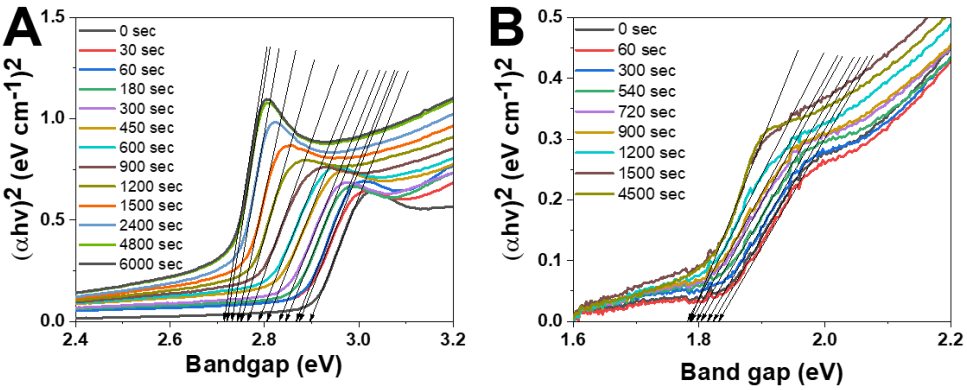

Figure A.6. (A,B) Tauc plots for $CsPbCl_3$ (A) and $CsPbI_3$ (B) nanocrystal films annealed at 130 °C for different annealing times.

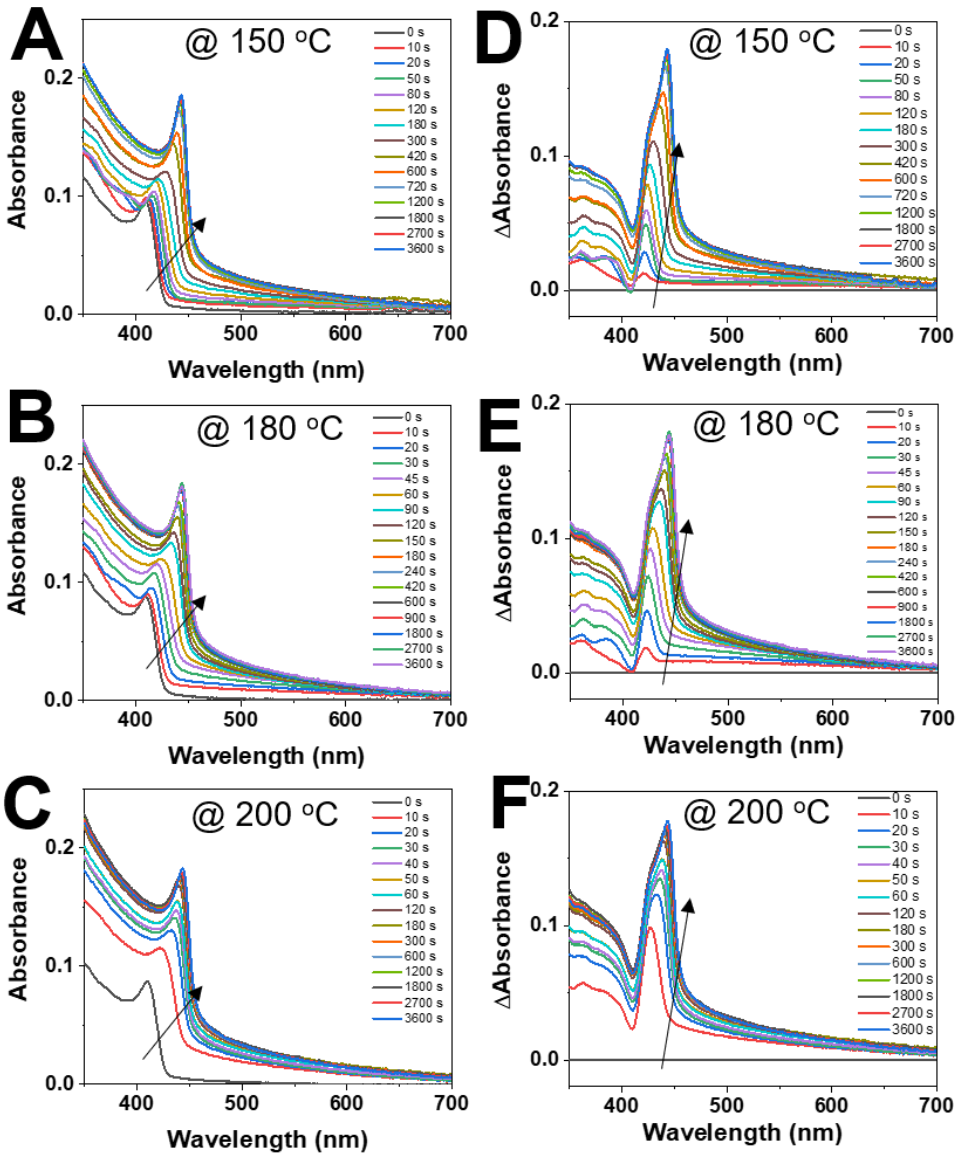

Figure A.7. (A–C) Absorption spectra and (D–F) different absorption spectra acquired for the $CsPbCl_3$ nanocrystal films annealed at different temperature of 150 (A,D), 180 (B,E), and 200 °C (C,F) for different annealing time. The arrows indicate the growth of bulk crystallites as marked by the peak at 440 nm.

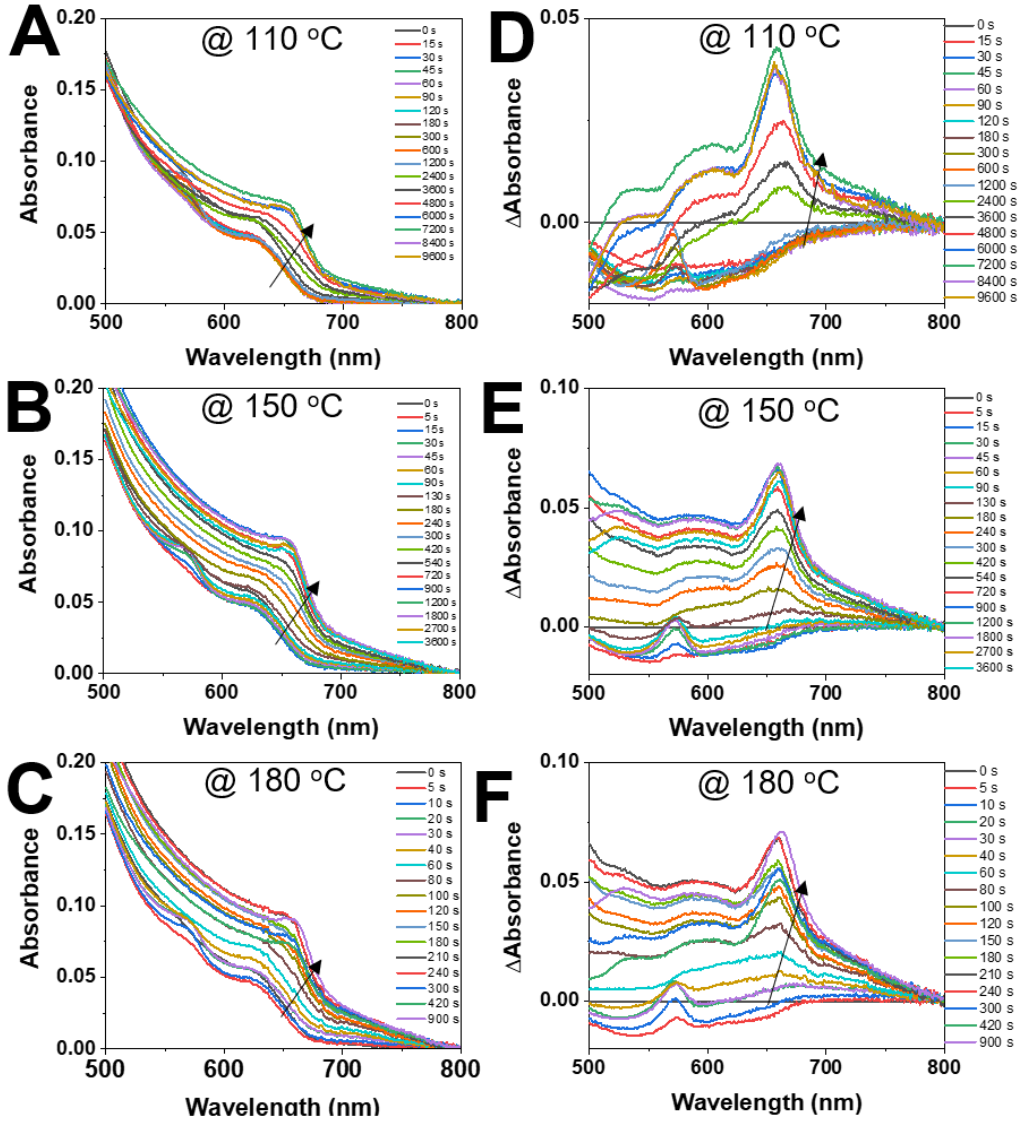

Figure A.8. (A–C) Absorption spectra and (D–F) different absorption spectra acquired for the $CsPbI_3$ nanocrystal films annealed at different temperature of 150 (A,D), 180 (B,E), and 200 °C (C,F) for different annealing time. The arrows indicate the growth of bulk crystallites as marked by the peak at 650 nm.

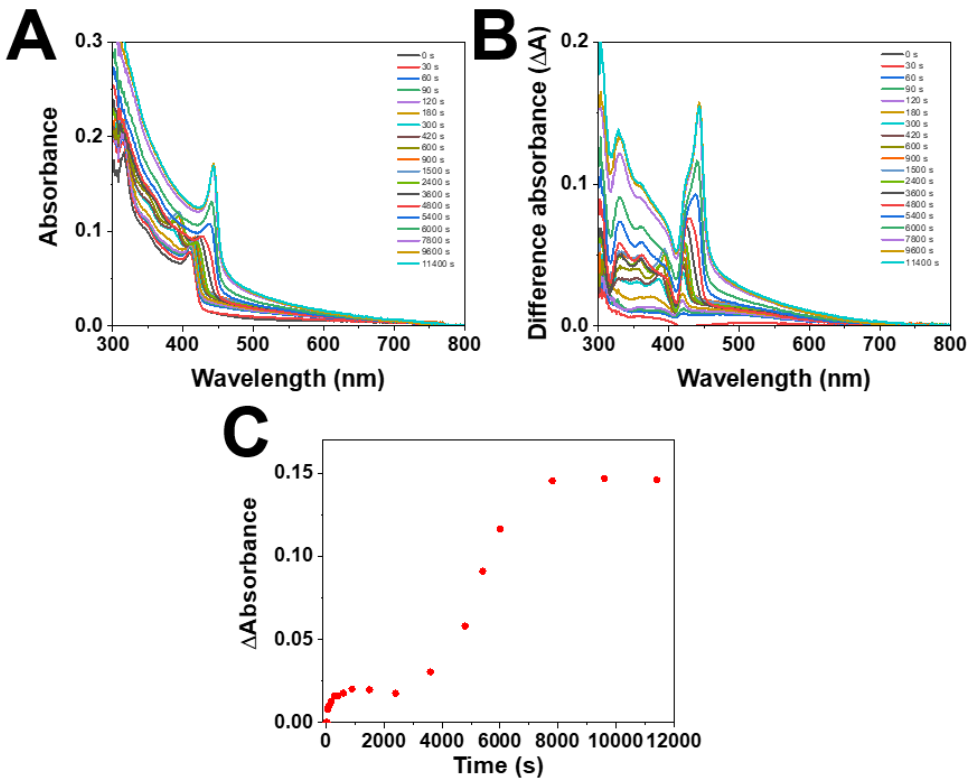

Figure A.9. (A) Absorption spectra and (B) different absorption spectra acquired for the $CsPbCl_3$ nanocrystal films annealed at 110 °C for different annealing times. (C) Corresponding kinetic traces over the annealing time as shown in the panel B by tracking the bulk peak at 440 nm.

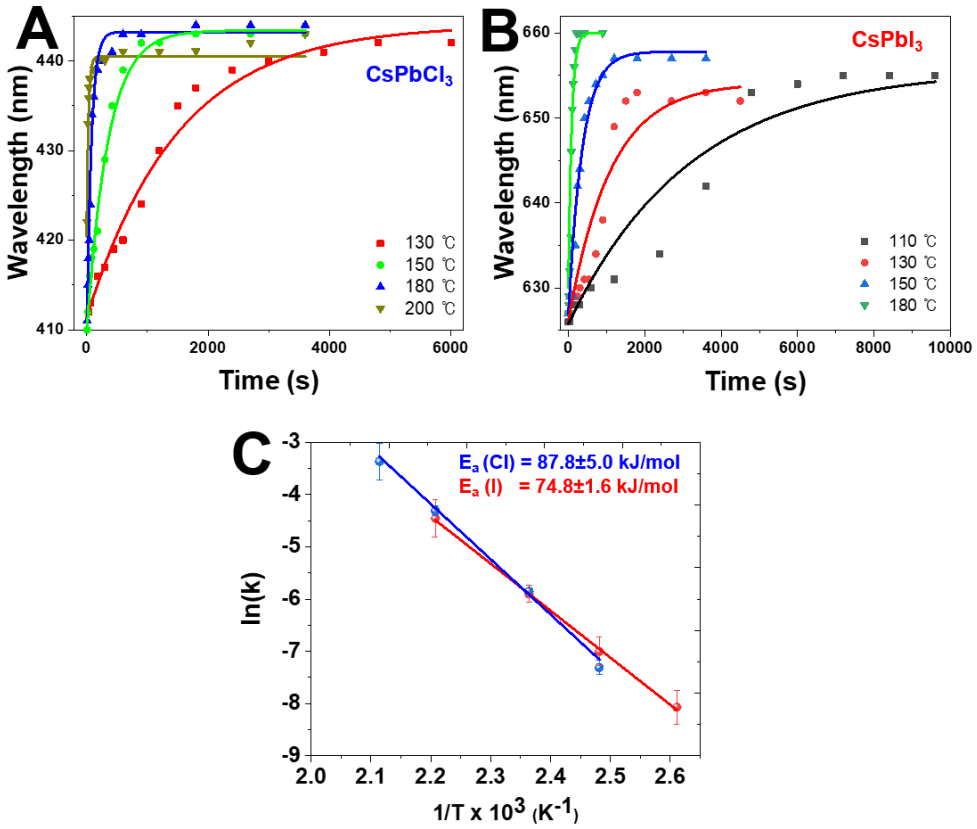

Figure A.10. (A,B) Changes in the wavelength of nanocrystal films by tracking the band-edge absorption peak for $CsPbCl_3$ (A) and for $CsPbI_3$ (B) during the course of annealing at the different temperatures (110-200 °C). (C) Arrhenius plot of ln(k) versus inverse temperature (1/T) obtained from the kinetic fitting of panels A,B. Monoexponential fits were used for detemination of rate contant k.

$CsPbCl_3$ films	A_1	τ_1 (ns)	A_2	τ_2 (ns)	τ_{ave} (ns)
0 sec	0.97	0.14	0.03	4.99	2.5
60 sec	0.85	0.67	0.15	5.48	3.6
300 sec	0.85	1.71	0.15	8.28	4.7
600 sec	0.82	1.36	0.18	9.97	6.7
1500 sec	0.85	0.98	0.15	8.28	5.3
2400 sec	0.97	0.60	0.03	6.94	2.1
4200 sec	0.81	0.65	0.19	1.99	1.2
$CsPbI_3$ films	A_1	τ_1 (μs)	A_2	τ_2 (μs)	$\tau_{ave}{}^{Mn}$(μs)
0 sec	0.60	1.19	0.39	25.3	23.7
60 sec	0.58	3.89	0.41	30.6	26.5
300 sec	0.95	0.88	0.05	13.6	6.2
600 sec	0.98	0.18	0.02	6.56	2.5
1500 sec	1	0.17	-	-	0.17

Table A.1 Kinetic fitting parameters obtained using biexponential fitting for CsPbCl3 and CsPbI3 nanocrystal films upon annealing at 130 °C for different time. The average carrier lifetimes (τ_{ave}) is computed by considering individual lifetimes (τ_1 and τ_2) and the corresponding amplitudes (A_1 and A_2).

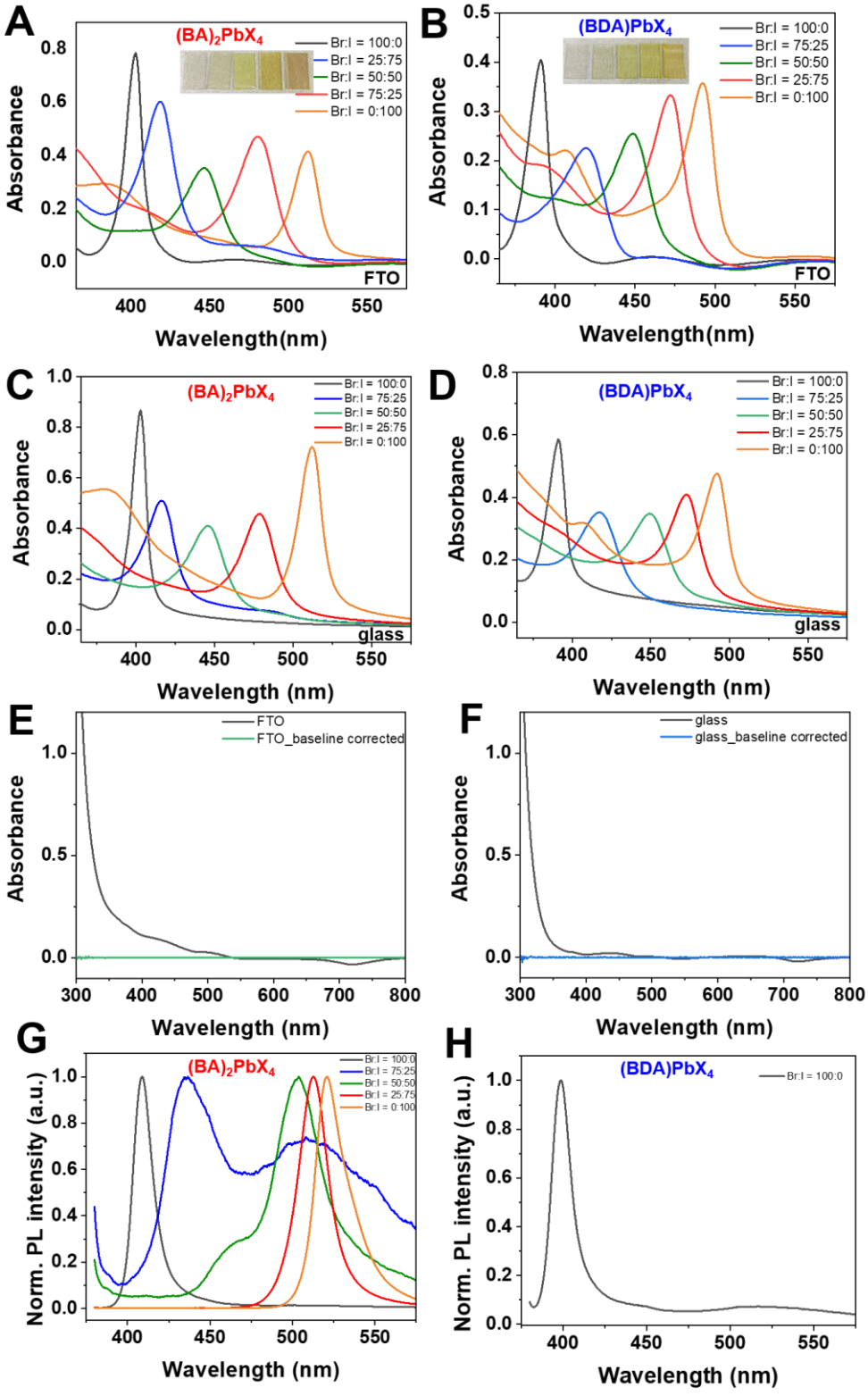
A
(BA)2PbX4
Br:I = 100:0
Br:I = 25:75
Br:I = 50:50
Br:I = 75:25
Br:I = 0:100
FTO
Absorbance
Wavelength(nm)
B
(BDA)PbX4
Br:I = 100:0
Br:I = 75:25
Br:I = 50:50
Br:I = 25:75
Br:I = 0:100
FTO
Absorbance
Wavelength(nm)
C
(BA)2PbX4
Br:I = 100:0
Br:I = 75:25
Br:I = 50:50
Br:I = 25:75
Br:I = 0:100
glass
Absorbance
Wavelength (nm)
D
(BDA)PbX4
Br:I = 100:0
Br:I = 75:25
Br:I = 50:50
Br:I = 25:75
Br:I = 0:100
glass
Absorbance
Wavelength (nm)
E
FTO
FTO_baseline corrected
Absorbance
Wavelength (nm)
F
glass
glass_baseline corrected
Absorbance
Wavelength (nm)
G
(BA)2PbX4
Br:I = 100:0
Br:I = 75:25
Br:I = 50:50
Br:I = 25:75
Br:I = 0:100
Norm. PL intensity (a.u.)
Wavelength (nm)
H
(BDA)PbX4
Br:I = 100:0
Norm. PL intensity (a.u.)
Wavelength (nm)

Figure A.11. (A,B) Absorption spectra of 2D RP $(BA)_2PbX_4$ (X = Br:I) and 2D DJ $(BDA)PbX_4$ (X = Br:I) perovskite films with varying Br:I ratio from Br:I = 100:0 to 0:100 on a FTO substrate. (C,D) Absorption spectra of 2D RP $(BA)_2PbX_4$ (X = Br:I) and 2D DJ $(BDA)PbX_4$ (X = Br:I) perovskite films with varying Br:I ratio from Br:I = 100:0 to 0:100 on a glass substrate. (E,F) Absorption spectra of (E) FTO and FTO-based line correction and (F) glass and glass-based line correction. (G,H) PL emission spectra of BA- and BDA-based film with a different halide composition from Br:I = 100:0 to 0:100 on a glass substrate. Noting that PL emission spectra were recorded with a glass since a FTO can serve as a electron transport layer, leading to reduced PL emission. The inset digital photographs of S1A,B represent the as-prepared film with different halide composition from Br:I = 100:0 to 0:100.

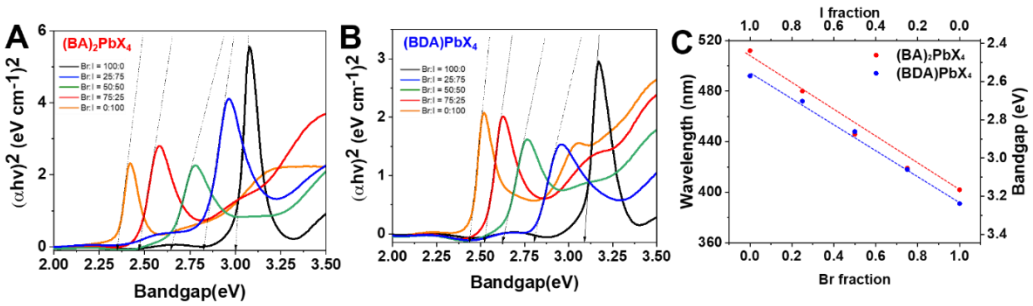

Figure A.12. (A,B) Corresponding *Tauc* plots of the $(BA)_2PbX_4$ (A) and $(BDA)PbX_4$ (B) perovskite films deposited on FTO substrates as shown in panel of Figures S1A,B. (C) Corresponding change in band-edge wavelength (nm) and bandgap (eV) as a function of halide composition for 2D RP and DJ perovskites films.

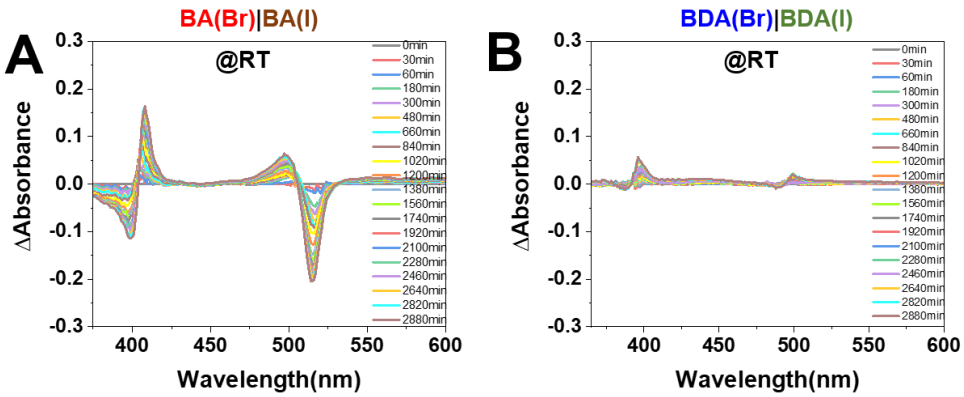

Figure A.13. (A,B) Difference absorption spectra recorded at room temperature for the physically paired 2D bromide and iodide perovskites films deposited on FTO substrates: (A) $(BA)_2PbBr_4|(BA)_2PbI_4$ with RP and (B) $(BDA)PbBr_4|(BDA)PbI_4$ with DJ. The absorption spectrum recorded at 0 min was served as reference to obtain the difference absorption spectra (⊿A).

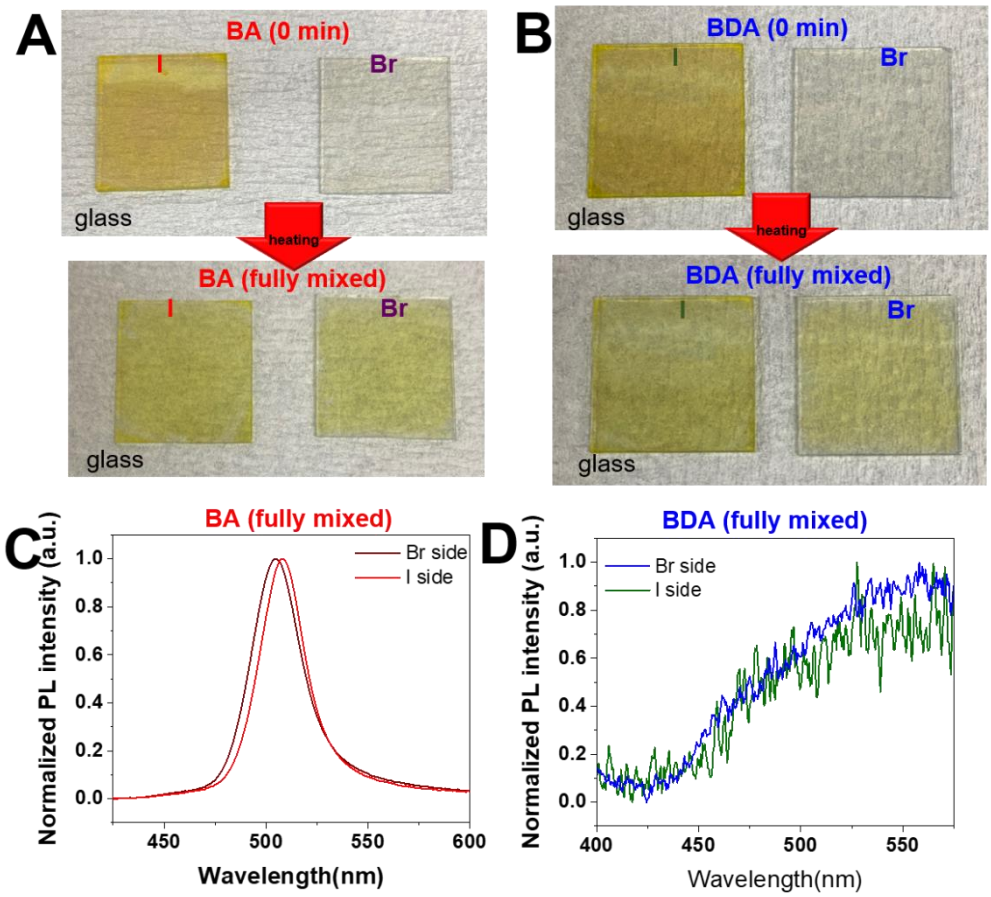

Figure A.14. (A,B) Digital photographs taken under laboratory light before (up) and after (bottom) mixing using 2D BA−based perovskites (A) and BDA−based perovskites (B) film with bromide (Br) and iodide (I), respectively, on a glass substrate. (C,D) PL emission spectra for fully− mixed film recorded using Br and I side, respectively for BA− (C) and BDA−based (D) mixed halide perovskite films.

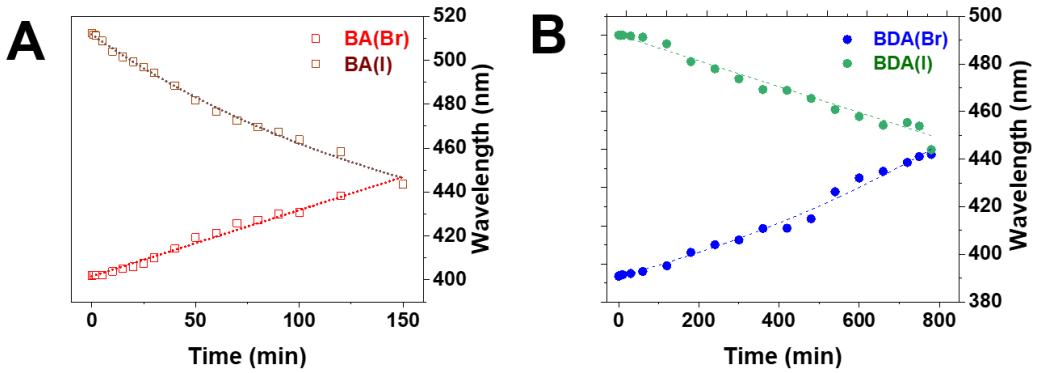

Figure A.15. (A,B) Changes in wavelength by tracking the band-edge wavelength of (A) BA (X = Br, I) and (B) BDA (X = Br, I) films, respectively, during the course of halide ion mixing at 120 °C over time.

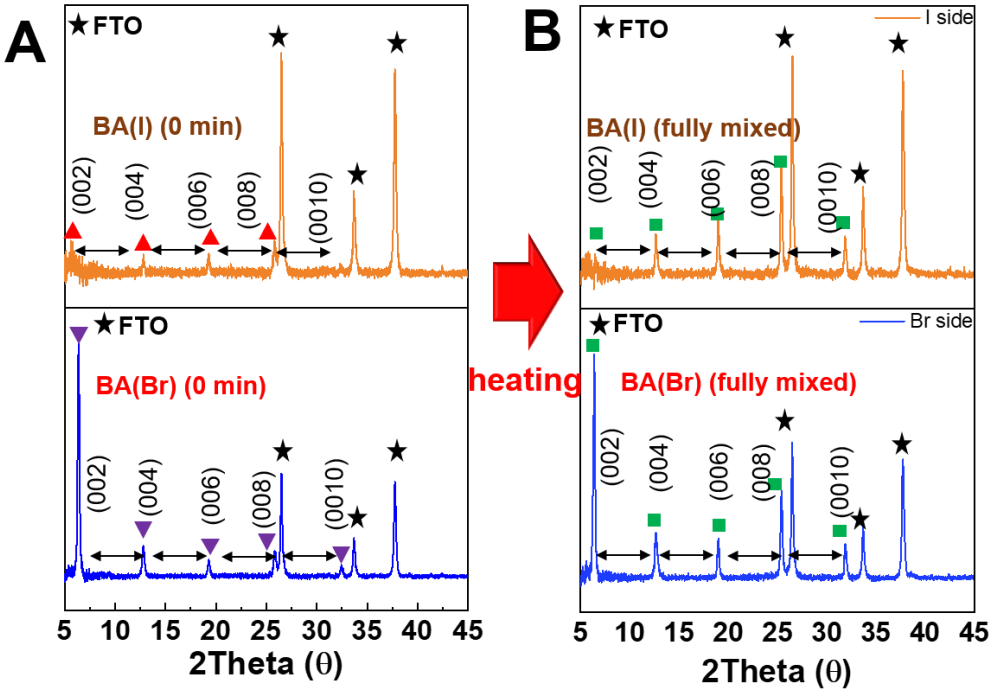

Figure A.16. (A,B) XRD patterns obtained before (0 min; A) and after mixing (fully-mixed; B) with BA(Br) and BA(I) on a FTO substrate. Asterisk marks on panel A,B denote the XRD patterns generated from FTO substrate. The black arrow indicates the periodicity found in 2D layered structures.

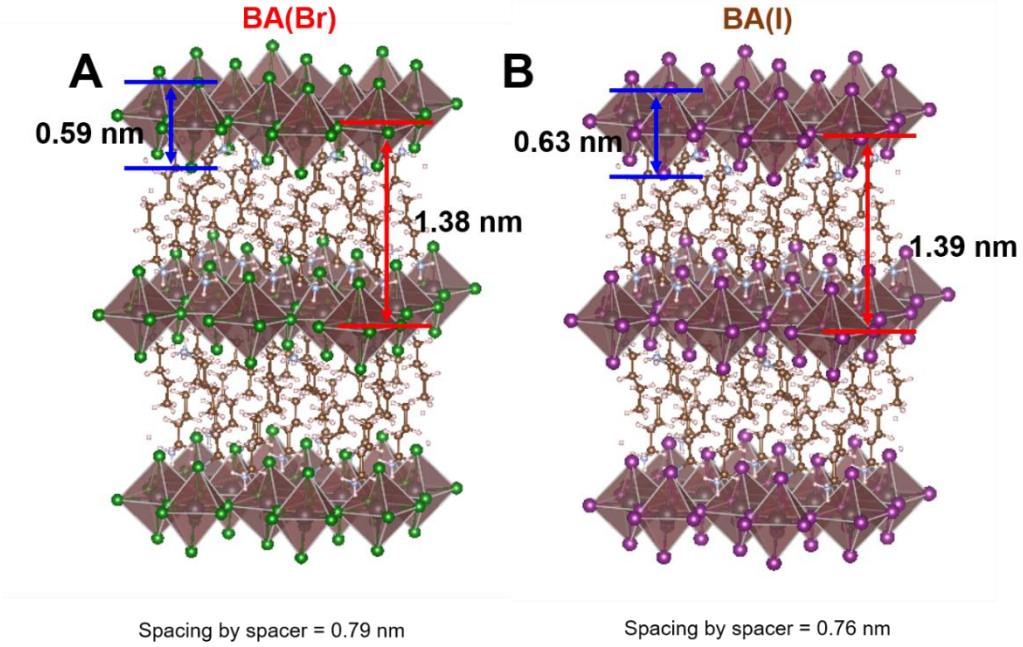

Figure A.17. (A,B) Crystallographic structures of (A) BA(Br) and (B) BA(I). The thickness of lead octahedral $[PbX_6]^{4-}$ is indicated with blue arrows whereas the interlayer spacing is indicated with red arrows within each structure.

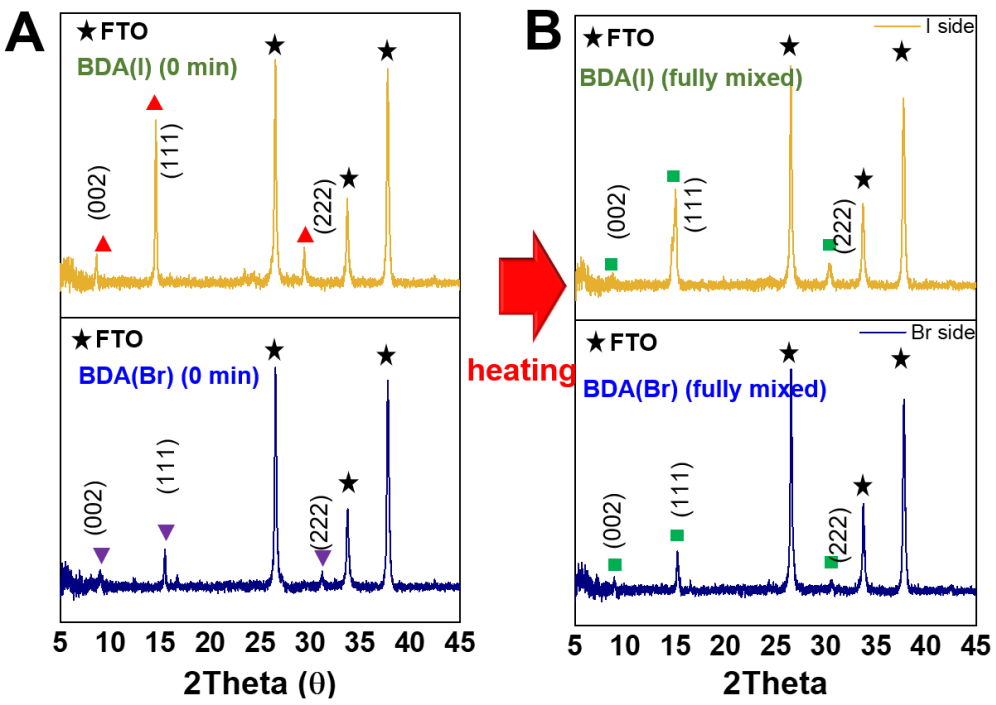

Figure A.18. (A,B) XRD patterns obtained before (0 min; A) and after mixing (fully mixed; B) with BDA(Br) and BDA(I) on a FTO substrate. Asterisk marks on panel A,B denote the XRD patterns generated from FTO substrate.

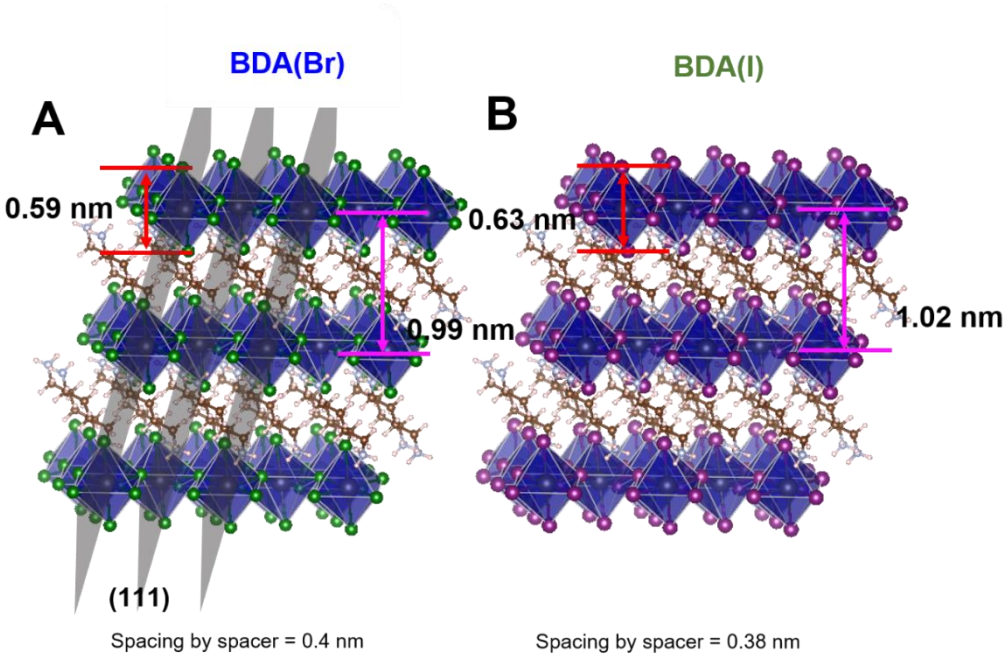

Figure A.19. (A,B) Crystallographic structures of (A) BDA(Br), (B) BDA(I). The thickness of lead octahedral $[PbX_6]^{4-}$ is indicated with red arrows whereas the interlayer spacing is indicated with margent arrows within each structure. The grey plane on panel A corresponds to the (111) crystallographic plane with a distinctive XRD reflection peak.

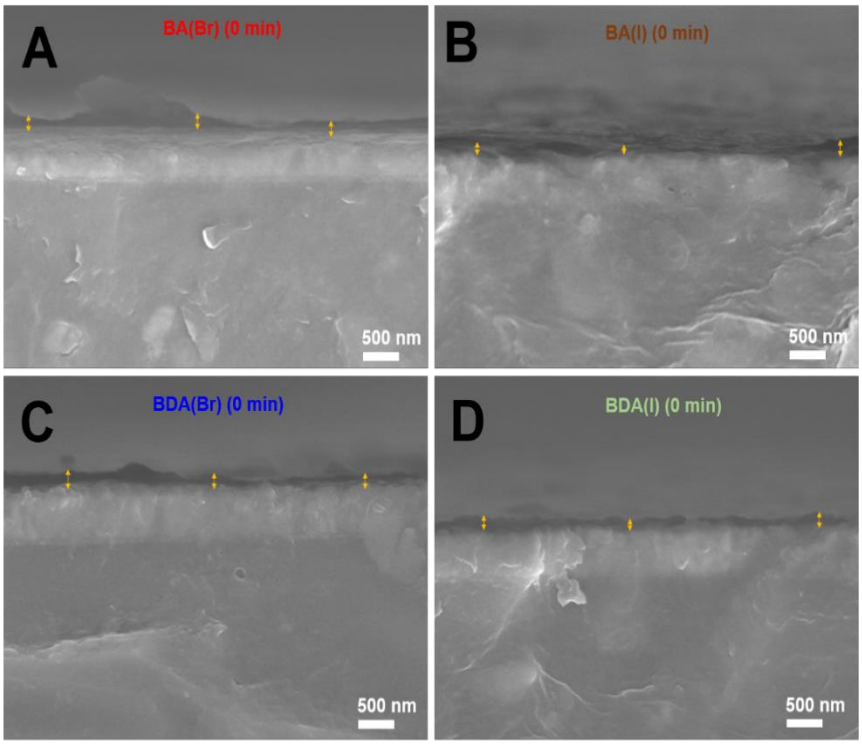
A
BA(Br) (0 min)
500 nm
B
BA(I) (0 min)
500 nm
C
BDA(Br) (0 min)
500 nm
D
BDA(I) (0 min)
500 nm

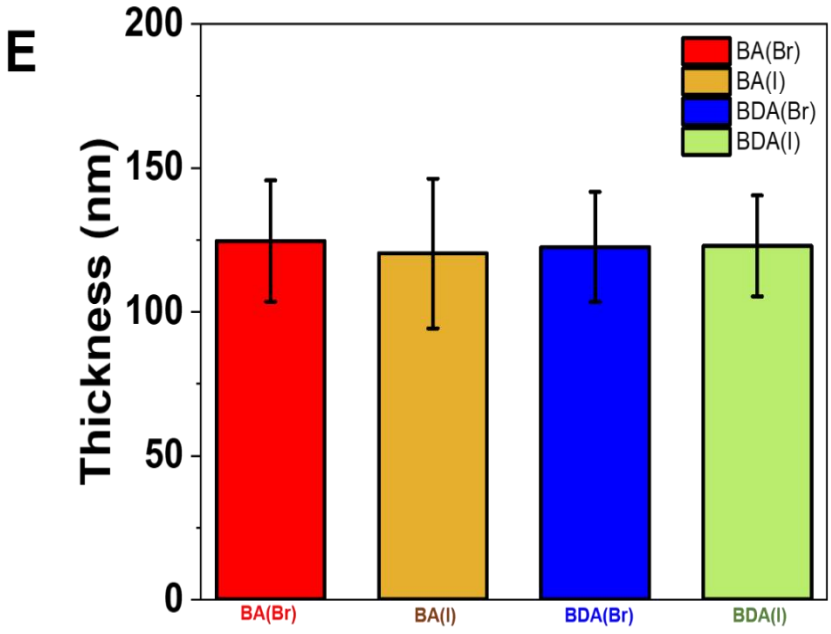
E
Thickness (nm)
200
150
100
50
0
BA(Br)
BA(I)
BDA(Br)
BDA(I)
BA(Br)
BA(I)
BDA(Br)
BDA(I)

Figure A.20. (A–D) Cross-section SEM images for 2D perovskite film before mixing (0 min): (A) BA(Br), (B) BA(I), (C) BDA(Br), and (D) BDA(I), respectively, on a FTO substrate. (E) Average thickness and standard deviation of each film. The average thickness of the film determined by counting six different points was 122 ± 21 nm (for BA(Br)), 120 ± 26 nm (for BA(Br)), 122 ± 19 nm (for BDA(Br)), and 122 ± 17 nm (for BDA(I)), respectively.

BA(Br)|BA(I)

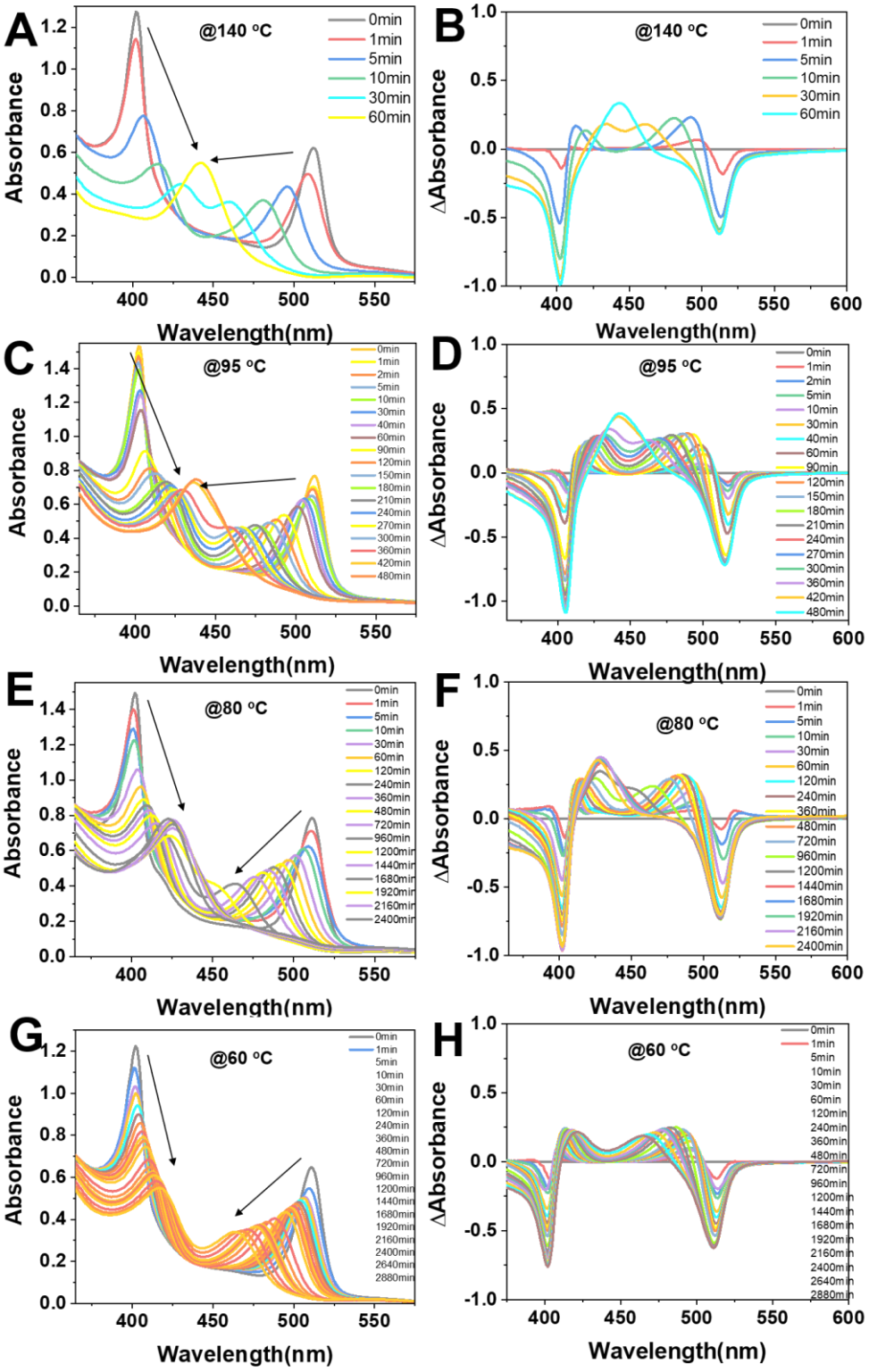
A
@140 °C
0min
1min
5min
10min
30min
60min
Absorbance
Wavelength(nm)
B
@140 °C
ΔAbsorbance
C
@95 °C
D
@95 °C
E
@80 °C
F
@80 °C
G
@60 °C
H
@60 °C

Figure A.21. (A,C,E,G) Absorption and (B,D,F,H) difference spectra of the paired 2D lead bromide and iodide (BA(Br)|BA(I)) films on a FTO substrate recorded at different temperature of (A,B) 140 ° C, (C,D) 95 ° C, (E,F) 80 ° C, and (G,H) 60 ° C as a function of mixing time. The absorption spectrum at 0 min was served as reference to obtain the difference absorption spectra (⊿A).

BDA(Br)|BDA(I)

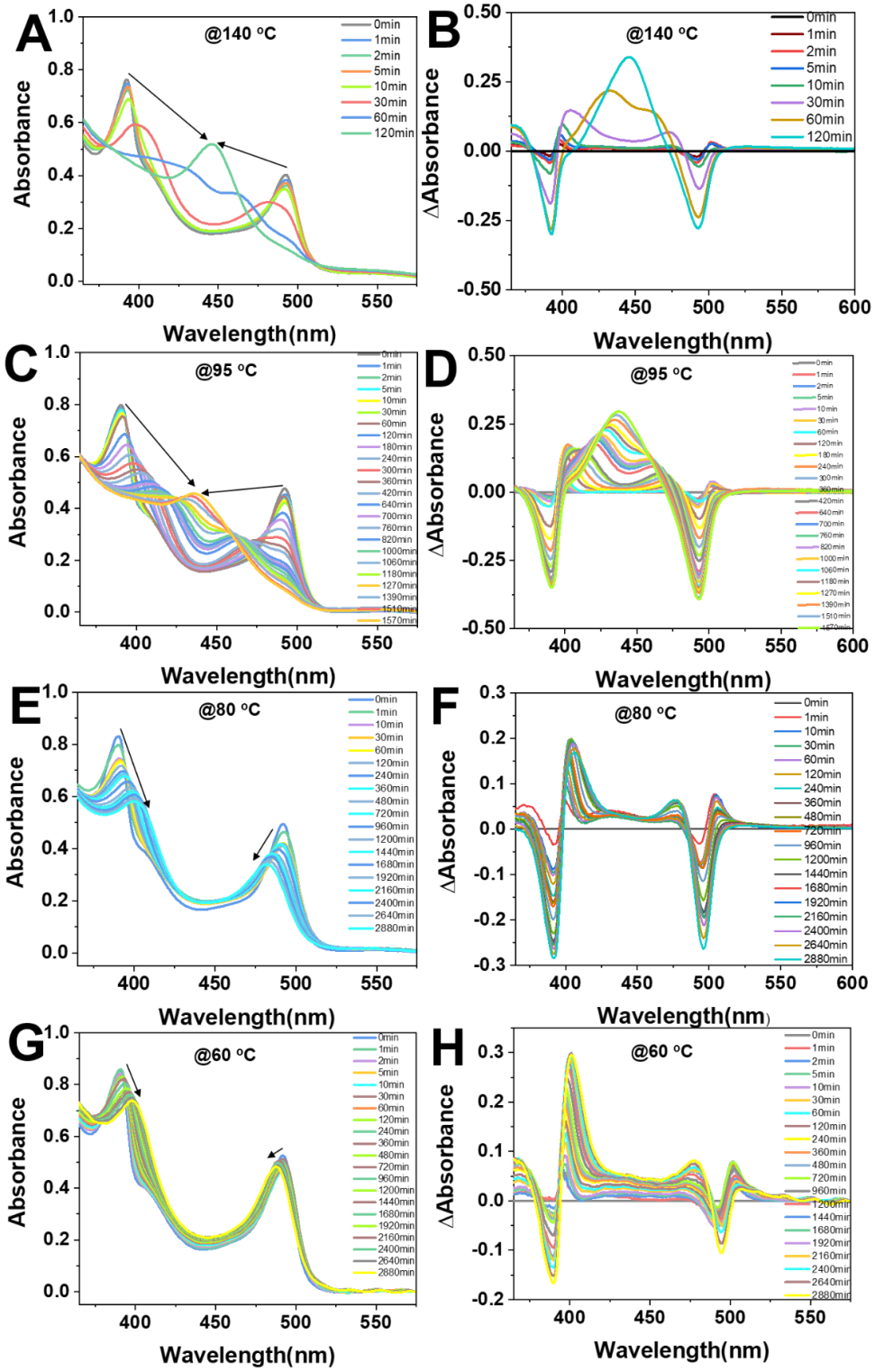
A
@140 °C
Absorbance
Wavelength(nm)
B
@140 °C
ΔAbsorbance
Wavelength(nm)
C
@95 °C
Absorbance
Wavelength(nm)
D
@95 °C
ΔAbsorbance
Wavelength(nm)
E
@80 °C
Absorbance
Wavelength(nm)
F
@80 °C
ΔAbsorbance
Wavelength(nm)
G
@60 °C
Absorbance
Wavelength(nm)
H
@60 °C
ΔAbsorbance
Wavelength(nm)

Figure A.22. (A,C,E,G) Absorption and (B,D,F,H) difference spectra of the paired 2D lead bromide and iodide (BDA(Br)|BDA(I)) films recorded at different temperature of (A,B) 140 ° C, (C,D) 95 ° C, (E,F) 80 ° C, and (G,H) 60 ° C as a function of mixing time in air. The absorption spectrum at 0 min was served as reference to obtain the difference absorption spectra (⊿A).

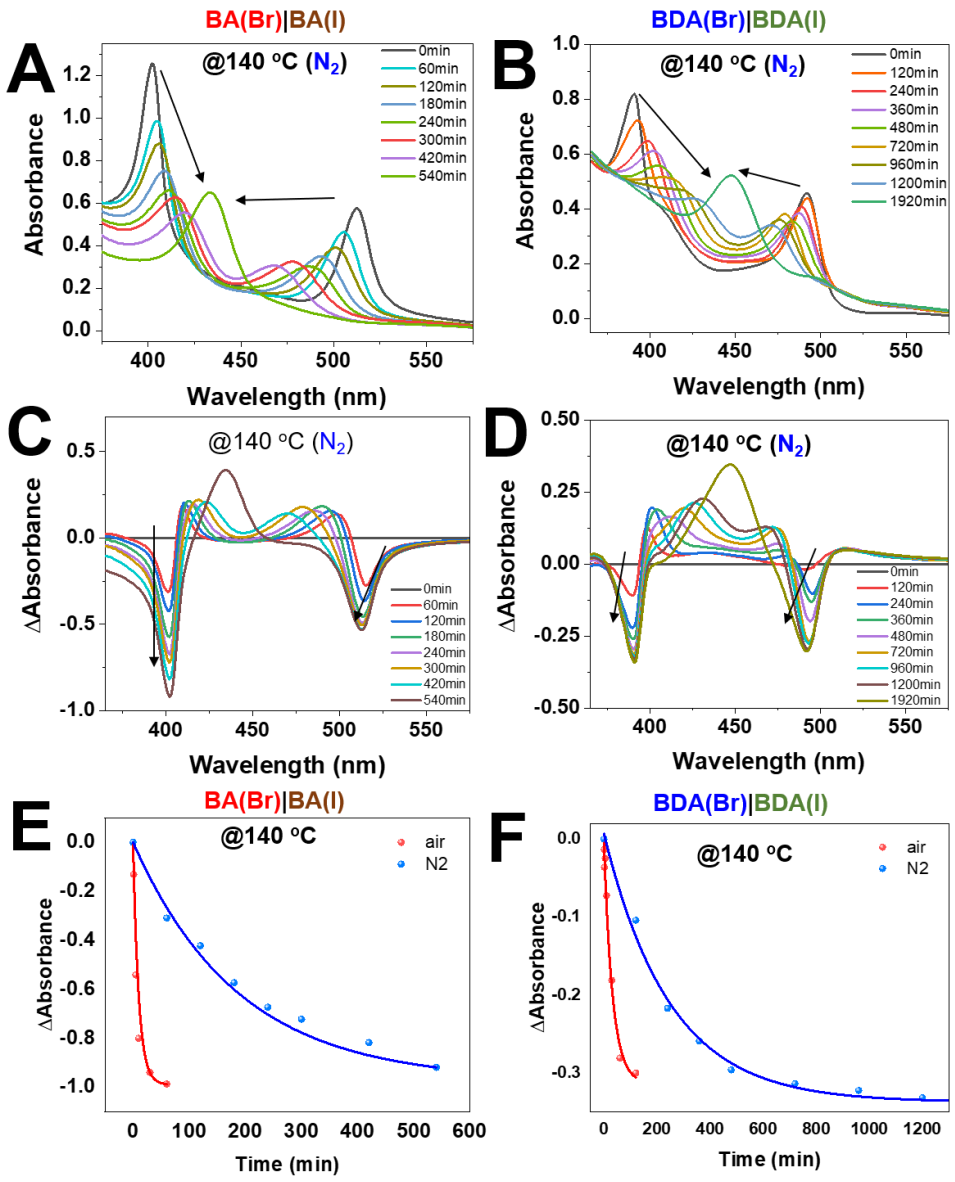

Figure A.23. (A,B) Absorption and (C,D) difference absorption spectra of the paired 2D lead bromide and iodide (BA(Br)|BA(I)) and (BDA(Br)|BDA(I)) film, respectively, recorded at 140 ° C as a function of mixing time in a glove box filled with nitrogen (N_2). The absorption spectrum at 0 min was served as reference to

obtain the difference absorption spectra (⊿A). (E,F) Corresponding kinetic traces and fittings for (BA(Br)|BA(I)) (E) and (BDA(Br)|BDA(I)) (F) films mixed in air and N_2 (glove box), respectively. Monoexponential function was used for fittings.

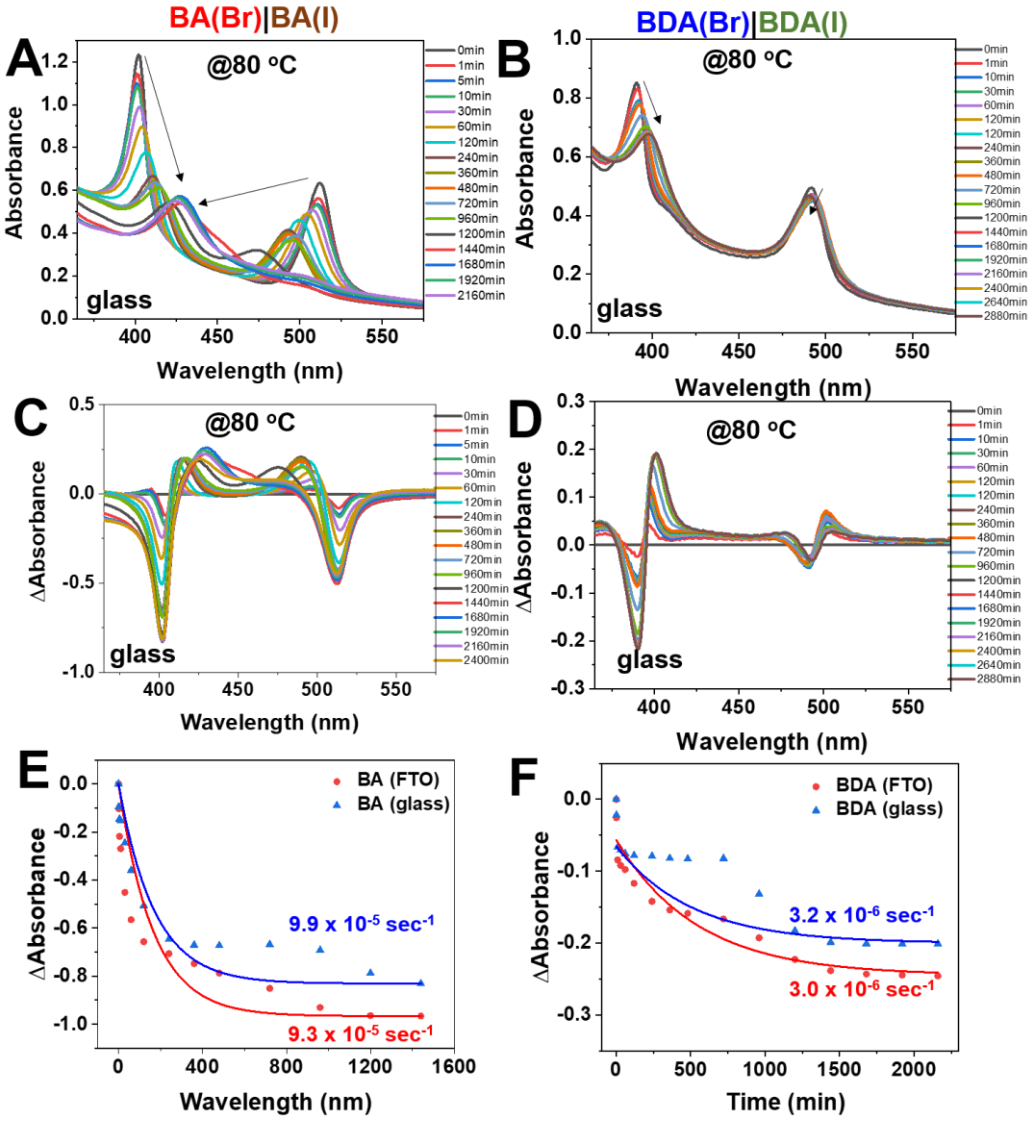

Figure A.24. (A,B) Absorption and (C,D) difference absorption spectra of the paired 2D lead bromide and iodide (BA(Br)|BA(I)) and (BDA(Br)|BDA(I)) film on a glass substrate, respectively, recorded at 140 ° C as a function of mixing time as control experiments. The absorption spectrum at 0 min was served as reference to obtain the difference absorption spectra (⊿A). (E,F) Corresponding

kinetic traces and fittings for (BA(Br)|BA(I)) (E) and (BDA(Br)|BDA(I)) (F) films mixed using a FTO and a glass substrate, respectively. Monoexponential decay function was used for fittings.

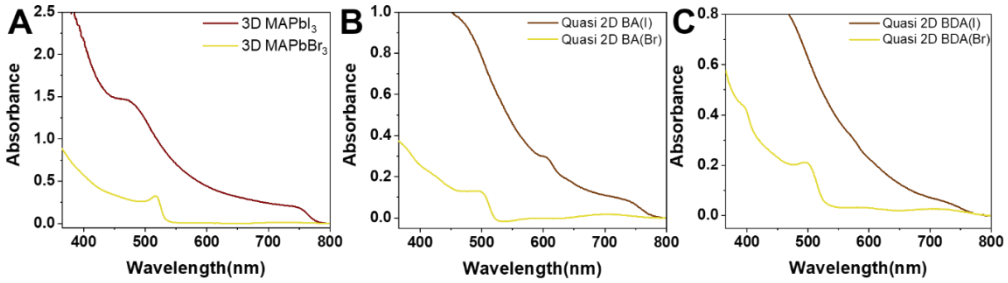

Figure A.25. (A–C) Absorption spectra of (A) 3D $MAPbX_3$ (X = Br, I), (B) quasi–2D BA–based (RP) perovskite film (X = Br, I), and (C) quasi–2D BDA–based (DJ) perovskites film (X = Br, I), respectively. Quasi–2D perovskites with same thickness of n = 10 were made for both RP and DJ phase.

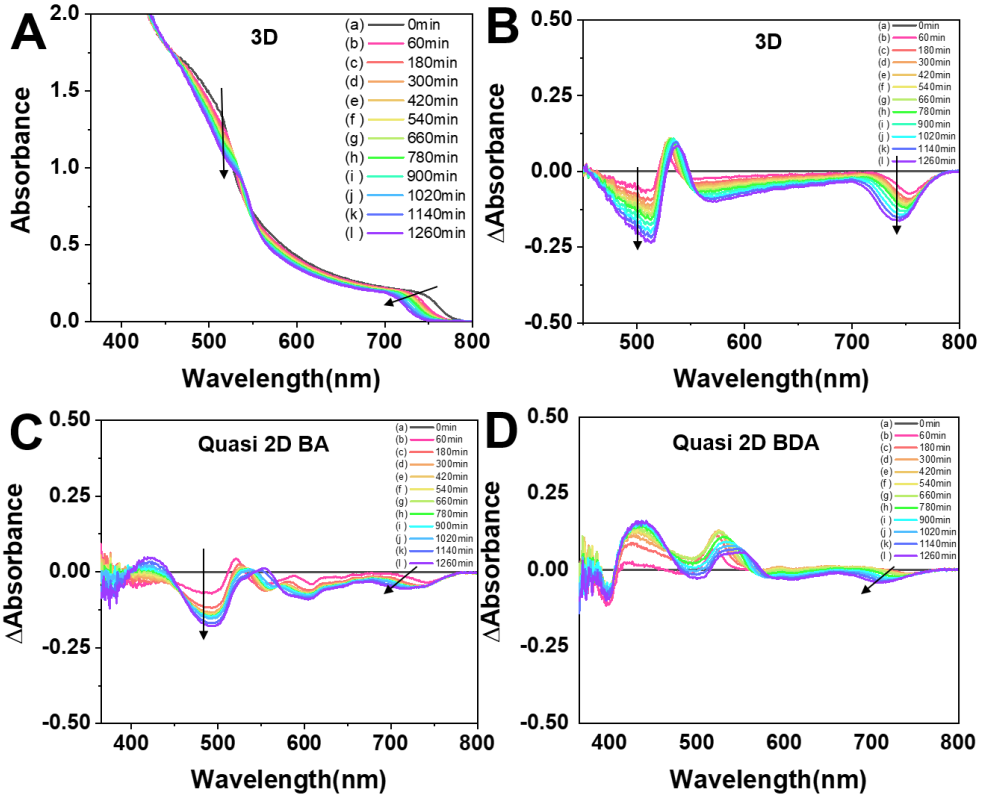

Figure A.26. (A,B) Absorption (A) and difference absorption (B) spectra for paired 3D lead bromide and iodide MAPbBr$_3$|MAPbI$_3$) recorded at 80 ° C over time. (C,D) difference absorption spectra recorded for paired quasi−2D (n = 10) bromide and iodide films obtained using BA with RP (C) and using BDA for DJ phase (D). The ratio of BA:MA = 9:2 and BDA:MA = 9:1 was used to yield each quasi−2D perovskites with n = 10, respectively.

REFERENCES

(1) Jing, H.; Peng, R.; Ma, R.-M.; He, J.; Zhou, Y.; Yang, Z.; Li, C.-Y.; Liu, Y.; Guo, X.; Zhu, Y.; Wang, D.; Su, J.; Sun, C.; Bao, W.; Wang, M. Flexible Ultrathin Single-Crystalline Perovskite Photodetector. *Nano Lett* 2020, *20* (10), 7144-7151. https://doi.org/10.1021/acs.nanolett.0c02468.

(2) Han, T. H.; Jang, K. Y.; Dong, Y.; Friend, R. H.; Sargent, E. H.; Lee, T. W. A Roadmap for the Commercialization of Perovskite Light Emitters. *Nature Reviews Materials*. Nature Research October 1, 2022, pp 757-777. https://doi.org/10.1038/s41578-022-00459-4.

(3) Yuan, S.; Dai, L.; Sun, Y.; Auras, F.; Zhou, Y.-H.; An, R.-Z.; Liu, Y.; Ding, C.; Cassidy, C.; Tang, X.; Dong, S.-C.; Kang, H.-B.; Chen, K.; Liu, X.; Ye, Z.-F.; Zhao, Y.; Adachi, C.; Liao, L.-S.; Greenham, N. C.; Qi, Y.; Stranks, S. D.; Cui, L.-S.; Friend, R. H. Efficient Blue Electroluminescence from Reduced-Dimensional Perovskites. *Nat Photonics* 2024, *18* (5), 425-431. https://doi.org/10.1038/s41566-024-01382-6.

(4) Lau, C. F. J.; Deng, X.; Ma, Q.; Zheng, J.; Yun, J. S.; Green, M. A.; Huang, S.; Ho-Baillie, A. W. Y. CsPbIBr2 Perovskite Solar Cell by Spray-Assisted Deposition. *ACS Energy Lett* 2016, *1* (3), 573-577. https://doi.org/10.1021/acsenergylett.6b00341.

(5) Cho, H. Bin; Min, J. W.; Kim, H. J.; Viswanath, N. S. M.; Samanta, T.; Han, J. H.; Park, Y. M.; Jang, S. W.; Im, W. Bin. Three-Dimensional Lead Halide Perovskites Embedded in Zero-Dimensional Lead Halide Perovskites: Synthesis, Stability, and Applications. *ACS Appl Electron Mater* 2023, *5* (1), 66-76. https://doi.org/10.1021/acsaelm.2c01297.

(6) Li, X.; Hoffman, J. M.; Kanatzidis, M. G. The 2D Halide Perovskite Rulebook: How the Spacer Influences Everything from the Structure to Optoelectronic Device Efficiency. *Chemical Reviews*. American Chemical Society February 24, 2021, pp 2230-2291. https://doi.org/10.1021/acs.chemrev.0c01006.

(7) Weidman, M. C.; Seitz, M.; Stranks, S. D.; Tisdale, W. A. Highly Tunable Colloidal Perovskite Nanoplatelets through Variable Cation, Metal, and Halide Composition. *ACS Nano* 2016, *10* (8), 7830-7839. https://doi.org/10.1021/acsnano.6b03496.

(8) Zhang, L.; Sun, C.; He, T.; Jiang, Y.; Wei, J.; Huang, Y.; Yuan, M. High-Performance Quasi-2D Perovskite Light-Emitting Diodes: From Materials to Devices. *Light Sci Appl* 2021, *10* (1), 61. https://doi.org/10.1038/s41377-021-00501-0.

(9) Brandt, R. E.; Poindexter, J. R.; Gorai, P.; Kurchin, R. C.; Hoye, R.

L. Z.; Nienhaus, L.; Wilson, M. W. B.; Polizzotti, J. A.; Sereika, R.; Žaltauskas, R.; Lee, L. C.; MacManus-Driscoll, J. L.; Bawendi, M.; Stevanović, V.; Buonassisi, T. Searching for "Defect-Tolerant" Photovoltaic Materials: Combined Theoretical and Experimental Screening. *Chemistry of Materials* **2017**, *29* (11), 4667-4674. https://doi.org/10.1021/acs.chemmater.6b05496.

(10) Wang, X.; Sun, Y.; Wang, Y.; Ai, X.-C.; Zhang, J.-P. Lewis Base Plays a Double-Edged-Sword Role in Trap State Engineering of Perovskite Polycrystals. *J Phys Chem Lett* **2022**, *13* (6), 1571-1577. https://doi.org/10.1021/acs.jpclett.2c00167.

(11) Wu, X.; Trinh, M. T.; Zhu, X.-Y. Excitonic Many-Body Interactions in Two-Dimensional Lead Iodide Perovskite Quantum Wells. *The Journal of Physical Chemistry C* **2015**, *119* (26), 14714-14721. https://doi.org/10.1021/acs.jpcc.5b00148.

(12) Gong, J.; Hao, M.; Zhang, Y.; Liu, M.; Zhou, Y. Layered 2D Halide Perovskites beyond the Ruddlesden-Popper Phase: Tailored Interlayer Chemistries for High-Performance Solar Cells. *Angewandte Chemie - International Edition*. John Wiley and Sons Inc March 1, 2022. https://doi.org/10.1002/anie.202112022.

(13) Chakraborty, R.; Nag, A. Dielectric Confinement for Designing Compositions and Optoelectronic Properties of 2D Layered Hybrid Perovskites. *Physical Chemistry Chemical Physics* **2021**, *23* (1), 82–93. https://doi.org/10.1039/D0CP04682E.

(14) Hoye, R. L. Z.; Hidalgo, J.; Jagt, R. A.; Correa–Baena, J. P.; Fix, T.; MacManus–Driscoll, J. L. The Role of Dimensionality on the Optoelectronic Properties of Oxide and Halide Perovskites, and Their Halide Derivatives. *Advanced Energy Materials*. John Wiley and Sons Inc January 1, 2022. https://doi.org/10.1002/aenm.202100499.

(15) Vreeland, E. C.; Watt, J.; Schober, G. B.; Hance, B. G.; Austin, M. J.; Price, A. D.; Fellows, B. D.; Monson, T. C.; Hudak, N. S.; Maldonado–Camargo, L.; Bohorquez, A. C.; Rinaldi, C.; Huber, D. L. Enhanced Nanoparticle Size Control by Extending LaMer's Mechanism. *Chemistry of Materials* **2015**, *27* (17), 6059–6066. https://doi.org/10.1021/acs.chemmater.5b02510.

(16) Murali, B.; Kolli, H. K.; Yin, J.; Ketavath, R.; Bakr, O. M.; Mohammed, O. F. Single Crystals: The Next Big Wave of Perovskite Optoelectronics. *ACS Mater Lett* **2020**, *2* (2), 184–214. https://doi.org/10.1021/acsmaterialslett.9b00290.

(17) Brown, A. A. M.; Vashishtha, P.; Hooper, T. J. N.; Ng, Y. F.; Nutan, G. V; Fang, Y.; Giovanni, D.; Tey, J. N.; Jiang, L.; Damodaran, B.; Sum, T. C.; Pu, S. H.; Mhaisalkar, S. G.; Mathews, N. Precise Control of CsPbBr3 Perovskite Nanocrystal Growth at Room Temperature: Size Tunability and Synthetic Insights. *Chemistry of Materials* **2021**, *33* (7), 2387–2397. https://doi.org/10.1021/acs.chemmater.0c04569.

(18) Vighnesh, K.; Wang, S.; Liu, H.; Rogach, A. L. Hot–Injection Synthesis Protocol for Green–Emitting Cesium Lead Bromide Perovskite Nanocrystals. *ACS Nano* **2022**, *16* (12), 19618–19625. https://doi.org/10.1021/acsnano.2c11689.

(19) Ng, C. K.; Wang, C.; Jasieniak, J. J. Synthetic Evolution of Colloidal Metal Halide Perovskite Nanocrystals. *Langmuir* **2019**, *35* (36), 11609–11628. https://doi.org/10.1021/acs.langmuir.9b00855.

(20) Wang, X.; Bao, Z.; Chang, Y. C.; Liu, R. S. Perovskite Quantum Dots for Application in High Color Gamut Backlighting Display of Light–Emitting Diodes. *ACS Energy Letters*. American Chemical Society November 13, 2020, pp 3374–3396. https://doi.org/10.1021/acsenergylett.0c01860.

(21) Quan, L. N.; García de Arquer, F. P.; Sabatini, R. P.; Sargent, E. H. Perovskites for Light Emission. *Advanced Materials* **2018**, *30* (45),

1801996. https://doi.org/10.1002/adma.201801996.

(22) Scheidt, R. A.; Atwell, C.; Kamat, P. V. Tracking Transformative Transitions: From CsPbBr3 Nanocrystals to Bulk Perovskite Films. *ACS Mater Lett* **2019**, *1* (1), 8–13. https://doi.org/10.1021/acsmaterialslett.9b00001.

(23) Akkerman, Q. A.; D' Innocenzo, V.; Accornero, S.; Scarpellini, A.; Petrozza, A.; Prato, M.; Manna, L. Tuning the Optical Properties of Cesium Lead Halide Perovskite Nanocrystals by Anion Exchange Reactions. *J Am Chem Soc* **2015**, *137* (32), 10276–10281. https://doi.org/10.1021/jacs.5b05602.

(24) Guo, Y.; Zhang, X.; Wang, X.; Zhang, L.; Xu, Z.; Sun, D. Nanoemulsions Stable against Ostwald Ripening. *Langmuir* **2024**, *40* (2), 1364–1372. https://doi.org/10.1021/acs.langmuir.3c03019.

(25) van Westen, T.; Groot, R. D. Effect of Temperature Cycling on Ostwald Ripening. *Cryst Growth Des* **2018**, *18* (9), 4952–4962. https://doi.org/10.1021/acs.cgd.8b00267.

(26) Dagtepe, P.; Chikan, V. Quantized Ostwald Ripening of Colloidal Nanoparticles. *The Journal of Physical Chemistry C* **2010**, *114* (39), 16263–16269. https://doi.org/10.1021/jp105071a.

(27) Jiang, H.; Cui, S.; Chen, Y.; Zhong, H. Ion Exchange for Halide Perovskite: From Nanocrystal to Bulk Materials. *Nano Select* 2021, *2* (11), 2040–2060. https://doi.org/https://doi.org/10.1002/nano.202100084.

(28) McGovern, L.; Grimaldi, G.; Futscher, M. H.; Hutter, E. M.; Muscarella, L. A.; Schmidt, M. C.; Ehrler, B. Reduced Barrier for Ion Migration in Mixed–Halide Perovskites. *ACS Appl Energy Mater* 2021, *4* (12), 13431–13437. https://doi.org/10.1021/acsaem.1c03095.

(29) Cho, J.; DuBose, J. T.; Le, A. N. T.; Kamat, P. V. Suppressed Halide Ion Migration in 2D Lead Halide Perovskites. *ACS Mater Lett* 2020, *2* (6), 565–570. https://doi.org/10.1021/acsmaterialslett.0c00124.

(30) Dey, A.; Ye, J.; De, A.; Debroye, E.; Ha, S. K.; Bladt, E.; Kshirsagar, A. S.; Wang, Z.; Yin, J.; Wang, Y.; Quan, L. N.; Yan, F.; Gao, M.; Li, X.; Shamsi, J.; Debnath, T.; Cao, M.; Scheel, M. A.; Kumar, S.; Steele, J. A.; Gerhard, M.; Chouhan, L.; Xu, K.; Wu, X.; Li, Y.; Zhang, Y.; Dutta, A.; Han, C.; Vincon, I.; Rogach, A. L.; Nag, A.; Samanta, A.; Korgel, B. A.; Shih, C.–J.; Gamelin, D. R.; Son, D. H.; Zeng, H.; Zhong, H.; Sun, H.; Demir, H. V.; Scheblykin, I. G.; Mora–Seró, I.; Stolarczyk, J. K.; Zhang, J. Z.; Feldmann, J.; Hofkens, J.; Luther, J. M.; Pérez–Prieto, J.; Li, L.; Manna, L.; Bodnarchuk, M. I.; Kovalenko, M. V; Roeffaers, M. B. J.; Pradhan, N.;

Mohammed, O. F.; Bakr, O. M.; Yang, P.; Müller-Buschbaum, P.; Kamat, P. V; Bao, Q.; Zhang, Q.; Krahne, R.; Galian, R. E.; Stranks, S. D.; Bals, S.; Biju, V.; Tisdale, W. A.; Yan, Y.; Hoye, R. L. Z.; Polavarapu, L. State of the Art and Prospects for Halide Perovskite Nanocrystals. *ACS Nano* 2021, *15* (7), 10775–10981. https://doi.org/10.1021/acsnano.0c08903.

(31) Nedelcu, G.; Protesescu, L.; Yakunin, S.; Bodnarchuk, M. I.; Grotevent, M. J.; Kovalenko, M. V. Fast Anion-Exchange in Highly Luminescent Nanocrystals of Cesium Lead Halide Perovskites (CsPbX3, X = Cl, Br, I). *Nano Lett* 2015, *15* (8), 5635–5640. https://doi.org/10.1021/acs.nanolett.5b02404.

(32) J. B. Patel, D. P. McMeekin, H. J. Snaith, K. A. Bush, B. Conings, G. Volonakis, S. Bent, R. A. Belisle, T. Leijtens, E. S. Parrott, L. M. Herz, R. J. Sutton, D. J. Slotcavage, M. D. McGehee, H.-G. Boyen, R. May, A. Palmstrom, W. Ma, M. B. Johnston, A. Babayigit, T. Green, J. T.-W. Wang, F. Giustino, R. Prasanna, G. E. Eperon, R. L. Milot, F. Moghadam, *Science (80-.).* 2016, *354*, 861–865.

(33) M. V. Khenkin, E. A. Katz, A. Abate, G. Bardizza, J. J. Berry, C. Brabec, F. Brunetti, V. Bulović, Q. Burlingame, A. Di Carlo, R. Cheacharoen, Y. B. Cheng, A. Colsmann, S. Cros, K. Domanski, M. Dusza, C. J. Fell, S. R.

Forrest, Y. Galagan, D. Di Girolamo, M. Grätzel, A. Hagfeldt, E. von Hauff, H. Hoppe, J. Kettle, H. Köbler, M. S. Leite, S. (Frank) Liu, Y. L. Loo, J. M. Luther, C. Q. Ma, M. Madsen, M. Manceau, M. Matheron, M. McGehee, R. Meitzner, M. K. Nazeeruddin, A. F. Nogueira, Ç. Odabaşı, A. Osherov, N. G. Park, M. O. Reese, F. De Rossi, M. Saliba, U. S. Schubert, H. J. Snaith, S. D. Stranks, W. Tress, P. A. Troshin, V. Turkovic, S. Veenstra, I. Visoly-Fisher, A. Walsh, T. Watson, H. Xie, R. Yıldırım, S. M. Zakeeruddin, K. Zhu, M. Lira-Cantu, *Nat. Energy* 2020, *5*, 35-49.

(34) K. Ji, M. Anaya, A. Abfalterer, S. D. Stranks, *Adv. Opt. Mater.* 2021, *9*, 2002128.

(35) Q. A. Akkerman, G. Rainò, M. V. Kovalenko, L. Manna, *Nat. Mater.* 2018, *17*, 394-405.

(36) Y. Hassan, J. H. Park, M. L. Crawford, A. Sadhanala, J. Lee, J. C. Sadighian, E. Mosconi, R. Shivanna, E. Radicchi, M. Jeong, C. Yang, H. Choi, S. H. Park, M. H. Song, F. De Angelis, C. Y. Wong, R. H. Friend, B. R. Lee, H. J. Snaith, *Nature* 2021, *591*, 72-77.

(37) K. Leng, W. Fu, Y. Liu, M. Chhowalla, K. P. Loh, *Nat. Rev. Mater.* 2020, *5*, 482-500.

(38) A. Dey, J. Ye, A. De, E. Debroye, S. K. Ha, E. Bladt, A. S.

Kshirsagar, Z. Wang, J. Yin, Y. Wang, L. N. Quan, F. Yan, M. Gao, X. Li, J. Shamsi, T. Debnath, M. Cao, M. A. Scheel, S. Kumar, J. A. Steele, M. Gerhard, L. Chouhan, K. Xu, X. G. Wu, Y. Li, Y. Zhang, A. Dutta, C. Han, I. Vincon, A. L. Rogach, A. Nag, A. Samanta, B. A. Korgel, C. J. Shih, D. R. Gamelin, D. H. Son, H. Zeng, H. Zhong, H. Sun, H. V. Demir, I. G. Scheblykin, I. Mora-Seró, J. K. Stolarczyk, J. Z. Zhang, J. Feldmann, J. Hofkens, J. M. Luther, J. Pérez-Prieto, L. Li, L. Manna, M. I. Bodnarchuk, M. V. Kovalenko, M. B. J. Roeffaers, N. Pradhan, O. F. Mohammed, O. M. Bakr, P. Yang, P. Müller-Buschbaum, P. V. Kamat, Q. Bao, Q. Zhang, R. Krahne, R. E. Galian, S. D. Stranks, S. Bals, V. Biju, W. A. Tisdale, Y. Yan, R. L. Z. Hoye, L. Polavarapu, *ACS Nano* 2021, *15*, 10775-10981.

(39) P. Wangyang, C. Gong, G. Rao, K. Hu, X. Wang, C. Yan, L. Dai, C. Wu, J. Xiong, *Adv. Opt. Mater.* 2018, *6*, 1-30.

(40) Q. Chen, J. Wu, X. Ou, B. Huang, J. Almutlaq, A. A. Zhumekenov, X. Guan, S. Han, L. Liang, Z. Yi, J. Li, X. Xie, Y. Wang, Y. Li, D. Fan, D. B. L. Teh, A. H. All, O. F. Mohammed, O. M. Bakr, T. Wu, M. Bettinelli, H. Yang, W. Huang, X. Liu, *Nature* 2018, *561*, 88-93.

(41) V. Morad, Y. Shynkarenko, S. Yakunin, A. Brumberg, R. D. Schaller, M. V. Kovalenko, *J. Am. Chem. Soc.* 2019, DOI 10.1021/jacs.9b02365.

(42) J. H. Noh, S. H. Im, J. H. Heo, T. N. Mandal, S. Il Seok, 2013, 13, 1764–1769.

(43) A. Singldinger, M. Gramlich, C. Gruber, C. Lampe, A. S. Urban, *ACS Energy Lett.* 2020, *5*, 1380–1385.

(44) A. F. Gualdrón–Reyes, S. Masi, I. Mora–Seró, *Trends Chem.* 2021, *3*, 499–511.

(45) A. Swarnkar, R. Chulliyil, V. K. Ravi, M. Irfanullah, A. Chowdhury, A. Nag, *Angew. Chemie* 2015, *127*, 15644–15648.

(46) J. Cho, Y. H. Choi, T. E. O' Loughlin, L. De Jesus, S. Banerjee, *Chem. Mater.* 2016, *28*, 6909–6916.

(47) G. Almeida, L. Goldoni, Q. Akkerman, Z. Dang, A. H. Khan, S. Marras, I. Moreels, L. Manna, *ACS Nano* 2018, *12*, 1704–1711.

(48) H. Huang, J. Raith, S. V. Kershaw, S. Kalytchuk, O. Tomanec, L. Jing, A. S. Susha, R. Zboril, A. L. Rogach, *Nat. Commun.* 2017, *8*, 1–7.

(49) J. Cho, P. V. Kamat, *Adv. Opt. Mater.* 2020, *2001440*, 1–9.

(50) J. Cho, S. Banerjee, *Chem. Mater.* 2018, *30*, 6144–6155.

(51) E. J. Braham, J. Cho, K. M. Forlano, D. F. Watson, R. Arròyave, S. Banerjee, *Chem. Mater.* 2019, *31*, 3281–3292.

(52) M. H. Park, J. S. Kim, J. M. Heo, S. Ahn, S. H. Jeong, T. W. Lee, *ACS Energy Lett.* 2019, *4*, 1134-1149.

(53) Y.-H. Kim, C. Wolf, Y.-T. Kim, H. Cho, W. Kwon, S. Do, A. Sadhanala, C. G. Park, S.-W. Rhee, S. H. Im, R. H. Friend, T.-W. Lee, *ACS Nano* 2017, *11*, 6586-6593.

(54) Y.-H. Kim, C. Wolf, Y.-T. Kim, H. Cho, W. Kwon, S. Do, A. Sadhanala, C. Gyung Park, S.-W. Rhee, S. Hyuk Im, R. H. Friend, T.-W. Lee, *ACS Nano* 2017, *11*, 6586-6593.

(55) R. A. Scheidt, C. Atwell, P. V. Kamat, *ACS Mater. Lett.* 2019, *1*, 8-13.

(56) J. B. Hoffman, G. Zaiats, I. Wappes, P. V. Kamat, *Chem. Mater.* 2017, *29*, 9767-9774.

(57) J. B. Hoffman, A. L. Schleper, P. V. Kamat, *J. Am. Chem. Soc.* 2016, *138*, 8603-8611.

(58) J. Cho, J. T. Dubose, A. N. T. Le, P. V. Kamat, *ACS Mater. Lett.* 2020, *2*, 565-570.

(59) J. T. DuBose, P. V. Kamat, *ACS Mater. Lett.* 2022, *4*, 93-101.

(60) L. Cheng, C. Yi, Y. Tong, L. Zhu, G. Kusch, X. Wang, X. Wang, T.

Jiang, H. Zhang, J. Zhang, C. Xue, H. Chen, W. Xu, D. Liu, R. A. Oliver, R. H. Friend, L. Zhang, N. Wang, W. Huang, J. Wang, *Research* 2020, *2020*, 1–10.

(61) T. Qiao, D. H. Son, *Acc. Chem. Res.* 2021, DOI 10.1021/acs.accounts.0c00706.

(62) J.–H. Im, I.–H. Jang, N. Pellet, M. Grätzel, N.–G. Park, *Nat. Nanotechnol.* 2014, *9*, 927–932.

(63) Q. Zhao, A. Hazarika, L. T. Schelhas, J. Liu, E. A. Gaulding, G. Li, M. Zhang, M. F. Toney, P. C. Sercel, J. M. Luther, *ACS Energy Lett.* 2020, *5*, 238–247.

(64) M. C. Brennan, J. E. Herr, T. S. Nguyen–Beck, J. Zinna, S. Draguta, S. Rouvimov, J. Parkhill, M. Kuno, *J. Am. Chem. Soc.* 2017, *139*, 12201–12208.

(65) Q. A. Akkerman, T. P. T. Nguyen, S. C. Boehme, F. Montanarella, D. N. Dirin, P. Wechsler, F. Beiglböck, G. Rainò, R. Erni, C. Katan, J. Even, M. V Kovalenko, *Science (80-.).* 2022, *377*, 1406–1412.

(66) H. Choe, D. Jeon, S. J. Lee, J. Cho, *ACS Omega* 2021, *6*, 24304–24315.

(67) H. Choe, H. Jin, S. J. Lee, J. Cho, *ACS Appl. Nano Mater.* 2022, *5*,

18385–18395.

(68) K. E. Hughes, S. R. Ostheller, H. D. Nelson, D. R. Gamelin, *Nano Lett.* 2019, *2*, DOI 10.1021/acs.nanolett.8b04905.

[(69) T. Udayabhaskararao, L. Houben, H. Cohen, M. Menahem, I. Pinkas, L. Avram, T. Wolf, A. Teitelboim, M. Leskes, O. Yaffe, D. Oron, M. Kazes, *Chem. Mater.* 2018, *30*, 84–93.

(70) S. Toso, D. Baranov, L. Manna, *Acc. Chem. Res.* 2021, *54*, 498–508.

(71) N. T. K. Thanh, N. Maclean, S. Mahiddine, *Chem. Rev.* 2014, *114*, 7610–7630.

(72) Y. Yang, C. Hou, T.–X. Liang, *Phys. Chem. Chem. Phys.* 2021, *23*, 7145–7152.

(73) G. Di Liberto, O. Fatale, G. Pacchioni, *Phys. Chem. Chem. Phys.* 2021, *23*, 3031–3040.

(74) Q. Wang, Z. Gong, S. Wu, S. Pan, J. Pan, *J. Cryst. Growth* 2022, *596*, 126838.

(75) S. H. Hwang, D. H. Shin, J. Yun, C. Kim, M. Choi, J. Jang, *Chem. – A Eur. J.* 2014, *20*, 4439–4446.

(76) S. W. Lee, K. S. Ahn, K. Zhu, N. R. Neale, A. J. Frank, *J. Phys. Chem. C* 2012, *116*, 21285–21290.

(77) N. T. K. Thanh, N. Maclean, S. Mahiddine, *Chem. Rev.* 2014, *114*, 7610–7630.

(78) J. Cho, P. V. Kamat, *Chem. Mater.* 2020, *32*, 6206–6212.

(79) J. T. Dubose, P. V. Kamat, *Chem. Rev.* 2022, *122*, 12475–12494.

(80) J. T. Dubose, P. V. Kamat, *J. Am. Chem. Soc.* 2021, *143*, 19214–19223.

(81) J. T. Dubose, P. V. Kamat, *J. Phys. Chem. C* 2020, *124*, 12990–12998.

(82) J. Cho, J. T. Dubose, P. V. Kamat, *Chem. Mater.* 2020, *32*, 510–517.

(83) L. Z. Lei, Z. F. Shi, Y. Li, Z. Z. Ma, F. Zhang, T. T. Xu, Y. T. Tian, D. Wu, X. J. Li, G. T. Du, *J. Mater. Chem. C* 2018, *6*, 7982.

(84) P. Wangyang, C. Gong, G. Rao, K. Hu, X. Wang, C. Yan, L. Dai, C. Wu, J. Xiong, *Adv. Opt. Mater.* 2018, *6*, 1.

(85) J. H. Han, T. Samanta, Y. M. Park, H. J. Kim, N. S. Manikanta Viswanath, H. W. Kim, B. K. Cha, S. B. Cho, W. Bin Im, *ACS Energy Lett.* 2023, *8*, 545.

(86) Y. Li, Y. Lei, H. Wang, Z. Jin, *Nano–Micro Lett.* 2023, *15*, 1.

(87) F. Montanarella, K. M. McCall, K. Sakhatskyi, S. Yakunin, P. Trtik, C. Bernasconi, I. Cherniukh, D. Mannes, M. I. Bodnarchuk, M. Strobl, B. Walfort, M. V. Kovalenko, *ACS Energy Lett.* 2021, *6*, 4365.

(88) Y. Zhou, J. Chen, O. M. Bakr, O. F. Mohammed, *ACS Energy Lett.* 2021, *6*, 739.

(89) T. B. Shonde, A. Mondal, H. Liu, M. Chaaban, A. Ben–Akacha, S. Lee, E. S. Knorr, B. Ma, *ACS Mater. Lett.* 2022, *4*, 271.

(90) L. Mao, C. C. Stoumpos, M. G. Kanatzidis, *J. Am. Chem. Soc.* 2019, *141*, 1171.

(91) H. Tsai, W. Nie, J. C. Blancon, C. C. Stoumpos, R. Asadpour, B. Harutyunyan, A. J. Neukirch, R. Verduzco, J. J. Crochet, S. Tretiak, L. Pedesseau, J. Even, M. A. Alam, G. Gupta, J. Lou, P. M. Ajayan, M. J. Bedzyk, M. G. Kanatzidis, A. D. Mohite, *Nature* 2016, *536*, 312.

(92) X. Li, J. M. Hoffman, M. G. Kanatzidis, *Chem. Rev.* 2021, *121*, 2230.

(93) C. C. Stoumpos, M. G. Kanatzidis, *Acc. Chem. Res.* 2015, *48*, 2791.

(94) J. C. Blancon, H. Tsai, W. Nie, C. C. Stoumpos, L. Pedesseau, C. Katan, M. Kepenekian, C. M. M. Soe, K. Appavoo, M. Y. Sfeir, S. Tretiak,

P. M. Ajayan, M. G. Kanatzidis, J. Even, J. J. Crochet, A. D. Mohite, *Science (80−.).* 2017, *355*, 1288.

(95) E. D. Kinigstein, H. Tsai, W. Nie, J. C. Blancon, K. G. Yager, K. Appavoo, J. Even, M. G. Kanatzidis, A. D. Mohite, M. Y. Sfeir, *ACS Mater. Lett.* 2020, *2*, 1360.

(96) J. Cho, J. T. Dubose, P. V. Kamat, *J. Phys. Chem. Lett.* 2020, *11*, 2570.

(97) A. N. Yadav, S. Min, H. Choe, J. Park, J. Cho, *Small* 2023, DOI 10.1002/smll.202305546.

(98) J. Cho, J. T. Dubose, A. N. T. Le, P. V. Kamat, *ACS Mater. Lett.* 2020, *2*, 565.

(99) J. Cho, P. S. Mathew, J. T. DuBose, P. V. Kamat, *Adv. Mater.* 2021, *33*, 1.

(100) P. S. Mathew, J. T. Dubose, J. Cho, P. V. Kamat, *ACS Energy Lett.* 2021, *6*, 2499.

(101) J. V. Milić, S. M. Zakeeruddin, M. Grätzel, *Acc. Chem. Res.* 2021, *54*, 2729.

(102) A. Dučinskas, G. C. Fish, M. A. Hope, L. Merten, D. Moia, A.

Hinderhofer, L. C. Carbone, J. E. Moser, F. Schreiber, J. Maier, J. V. Milić, M. Grätzel, *J. Phys. Chem. Lett.* 2021, *12*, 10325.

(103) Y. Li, J. V. Milić, A. Ummadisingu, J. Y. Seo, J. H. Im, H. S. Kim, Y. Liu, M. I. Dar, S. M. Zakeeruddin, P. Wang, A. Hagfeldt, M. Grätzel, *Nano Lett.* 2019, *19*, 150.

(104) S. Ahmad, P. Fu, S. Yu, Q. Yang, X. Liu, X. Wang, X. Wang, X. Guo, C. Li, *Joule* 2019, *3*, 794.

(105) C. M. M. Soe, C. C. Stoumpos, M. Kepenekian, B. Traoré, H. Tsai, W. Nie, B. Wang, C. Katan, R. Seshadri, A. D. Mohite, J. Even, T. J. Marks, M. G. Kanatzidis, *J. Am. Chem. Soc.* 2017, *139*, 16297.

(106) Y. Liu, L. K. Ono, G. Tong, H. Zhang, Y. Qi, *ACS Energy Lett.* 2021, *6*, 908.

(107) H. Yu, Y. Xie, J. Zhang, J. Duan, X. Chen, Y. Liang, K. Wang, L. Xu, *Adv. Sci.* 2021, *8*, 1.

(108) C. H. A. Li, P. K. Ko, C. C. S. Chan, A. Sergeev, D. Chen, N. Tewari, K. S. Wong, J. E. Halpert, *Adv. Funct. Mater.* 2023, *2303301*, 1.

(109) T. L. Leung, H. W. Tam, F. Liu, J. Lin, A. M. C. Ng, W. K. Chan, W. Chen, Z. He, I. Lončarić, L. Grisanti, C. Ma, K. S. Wong, Y. S. Lau, F. Zhu,

Ž. Skoko, J. Popović, A. B. Djurišić, *Adv. Opt. Mater.* 2020, *8*, 1.

(110) G. Nedelcu, L. Protesescu, S. Yakunin, M. I. Bodnarchuk, M. J. Grotevent, M. V. Kovalenko, *Nano Lett.* 2015, *15*, 5635.

(111) V. K. Ravi, R. A. Scheidt, J. Dubose, P. V. Kamat, *J. Am. Chem. Soc.* 2018, *140*, 8887.

(112) V. K. Ravi, R. A. Scheidt, A. Nag, M. Kuno, P. V. Kamat, *ACS Energy Lett.* 2018, *3*, 1049.

(113) J. Cho, P. V. Kamat, *Adv. Opt. Mater.* 2020, *2001440*, 1.

(114) H. Choe, H. Jin, S. J. Lee, J. Cho, *ACS Appl. Nano Mater.* 2022, *5*, 18385.

(115) S. Min, H. Choe, S. Hyun Jung, J. Cho, *ChemPhysChem* 2023, DOI 10.1002/cphc.202300202.

(116) Q. A. Akkerman, V. D' Innocenzo, S. Accornero, A. Scarpellini, A. Petrozza, M. Prato, L. Manna, *J. Am. Chem. Soc.* 2015, *137*, 10276.

(117) T. Elmelund, R. A. Scheidt, B. Seger, P. V. Kamat, *ACS Energy Lett.* 2019, *4*, 1961.

(118) P. S. Mathew, P. V. Kamat, *Adv. Opt. Mater.* 2023, *2300957*, 1.

(119) J. Chakkamalayath, N. Hiott, P. V. Kamat, *ACS Energy Lett.* 2023, *8*, 169.

(120) H. Choe, D. Jeon, S. J. Lee, J. Cho, *ACS Omega* 2021, *6*, 24304.

(121) K. O. Ighodalo, W. Chen, Z. Liang, Y. Shi, S. Chu, Y. Zhang, R. Khan, H. Zhou, X. Pan, J. Ye, Z. Xiao, *Angew. Chemie – Int. Ed.* 2023, *62*, DOI 10.1002/anie.202213932.

(122) Y. Hassan, J. H. Park, M. L. Crawford, A. Sadhanala, J. Lee, J. C. Sadighian, E. Mosconi, R. Shivanna, E. Radicchi, M. Jeong, C. Yang, H. Choi, S. H. Park, M. H. Song, F. De Angelis, C. Y. Wong, R. H. Friend, B. R. Lee, H. J. Snaith, *Nature* 2021, *591*, 72.

(123) R. A. Kerner, Z. Xu, B. W. Larson, B. P. Rand, *Joule* 2021, *5*, 2273.

(124) Y. R. Wang, A. Senocrate, M. Mladenović, A. Dučinskas, G. Y. Kim, U. Rothlisberger, J. V. Milić, D. Moia, M. Grätzel, J. Maier, *Adv. Energy Mater.* 2022, *12*, DOI 10.1002/aenm.202200768.

(125) T. Elmelund, B. Seger, M. Kuno, P. V. Kamat, *ACS Energy Lett.* 2020, *5*, 56.

(126) F. Brivio, C. Caetano, A. Walsh, *J. Phys. Chem. Lett.* 2016, *7*, 1083.

(127) C. R. Roy, D. Pan, Y. Wang, M. P. Hautzinger, Y. Zhao, J. C. Wright,

Z. Zhu, S. Jin, *J. Am. Chem. Soc.* 2021, *143*, 5212.

(128) B. A. Rosales, L. Men, S. D. Cady, M. P. Hanrahan, A. J. Rossini, J. Vela, *Chem. Mater.* 2016, *28*, 6848.

(129) Akriti, S. Zhang, Z. Y. Lin, E. Shi, B. P. Finkenauer, Y. Gao, A. J. Pistone, K. Ma, B. M. Savoie, L. Dou, *Adv. Mater.* 2021, *33*, 1.

(130) K. Wang, Z. Y. Lin, Z. Zhang, L. Jin, K. Ma, A. H. Coffey, H. R. Atapattu, Y. Gao, J. Y. Park, Z. Wei, B. P. Finkenauer, C. Zhu, X. Meng, S. N. Chowdhury, Z. Chen, T. Terlier, T. H. Do, Y. Yao, K. R. Graham, A. Boltasseva, T. F. Guo, L. Huang, H. Gao, B. M. Savoie, L. Dou, *Nat. Commun.* 2023, *14*, 1.

(131) E. Shi, B. Yuan, S. B. Shiring, Y. Gao, Akriti, Y. Guo, C. Su, M. Lai, P. Yang, J. Kong, B. M. Savoie, Y. Yu, L. Dou, *Nature* 2020, *580*, 614.

(132) Y. Gao, E. Shi, S. Deng, S. B. Shiring, J. M. Snaider, C. Liang, B. Yuan, R. Song, S. M. Janke, A. Liebman-Peláez, P. Yoo, M. Zeller, B. W. Boudouris, P. Liao, C. Zhu, V. Blum, Y. Yu, B. M. Savoie, L. Huang, L. Dou, *Nat. Chem.* 2019, *11*, 1151.

(133) N. Hiott, J. Chakkamalayath, P. V Kamat, *ACS Mater. Lett.* 2023, 2614.

(134) E. T. Hoke, D. J. Slotcavage, E. R. Dohner, A. R. Bowring, H. I. Karunadasa, M. D. McGehee, *Chem. Sci.* 2015, *6*, 613.

(135) P. S. Mathew, J. Cho, P. V Kamat, *ACS Energy Lett.* 2021, *6*, 2499.

(136) P. S. Mathew, G. Szabó, M. Kuno, P. V. Kamat, *ACS Energy Lett.* 2022, *7*, 3982.

(137) C. M. Mauck, W. A. Tisdale, *Trends Chem.* 2019, *1*, 380.

(138) A. Senocrate, T. Acartürk, G. Y. Kim, R. Merkle, U. Starke, M. Grätzel, J. Maier, *J. Mater. Chem. A* 2018, *6*, 10847.

(139) C. R. Roy, Y. Zhou, D. D. Kohler, Z. Zhu, J. C. Wright, S. Jin, *ACS Energy Lett.* 2022, *7*, 3423.

(140) A. Dučinskas, G. Yeong Kim, D. Moia, A. Senocrate, Y.-R. Wang, M. A. Hope, A. Mishra, D. J. Kubicki, M. Siczek, W. Bury, T. Schneeberger, L. Emsley, J. V. Milić, J. Maier, M. Grätzel, *ACS Energy Lett.* 2021, *6*, 337.

(141) A. Ruth, M. C. Brennan, S. Draguta, Y. V. Morozov, M. Zhukovskyi, B. Janko, P. Zapol, M. Kuno, *ACS Energy Lett.* 2018, *3*, 2321.

(142) L. Huang, Z. Ge, X. Zhang, Y. Zhu, *J. Mater. Chem. A* 2021, *9*, 4379.

(143) N. Aristidou, C. Eames, I. Sanchez-Molina, X. Bu, J. Kosco, M.

Saiful Islam, S. A. Haque, *Nat. Commun.* 2017, *8*, 1.

(144) J. Schlipf, Y. Hu, S. Pratap, L. Bießmann, N. Hohn, L. Porcar, T. Bein, P. Docampo, P. Müller-Buschbaum, *ACS Appl. Energy Mater.* 2019, *2*, 1011.

(145) P. Toloueinia, H. Khassaf, A. Shirazi Amin, Z. M. Tobin, S. P. Alpay, S. L. Suib, *ACS Appl. Energy Mater.* 2020, *3*, 8240.

ABSTRACT IN KOREAN

개 요

민선홍

화학과

성신여자대학교 대학원

3차원(3D) 및 2차원(2D) 납 할로겐화물 페로브스카이트는 밴드 갭, 흡수 또는 방출 파장, 전하 캐리어 재조합 역학 등과 같은 광전자 특성을 쉽게 조정할 수 있기 때문에 발광 다이오드 및 광전지의 유망한 소재로 여겨져 왔습니다. 이러한 특성은 나노 결정의 크기, 할로겐화물 이온 구성 및 표면 리간드의 조절을 통해 미세하게 조정될 수 있습니다. 첫번째로, CsPbBr3 페로브스카이트 나노크리스탈의 납 팔면체 [PbX6]4− 내부의 Pb−X bonding strength (more ionic Pb−Cl versus more ionic Pb−I)에 대해 조사하였고, 그것이 CsPbX3(X = Cl, and I) 나노크리스탈의 growth kinetic에 미치는 영향에 대해 연구했습니다. 우리는 CsPbX3 (X=Cl, and I) 나노크리스탈의 growth kinetic에 대한 활성화 에너지를 다음과 같이 결정했습니다; 92 kJ/mol for CsPbCl3 and 71kJ/mol for CsPbI3.

두번째로, 우리는 2D 납 할로겐화물 페로브스카이트에서 halide ion migration에 대한 활성화 에너지를 결정했습니다. mono− 또는 multi−

dentate 특성에 의해 결정되는 2D 구조상의 spacer 리간드의 결합 모드는 halide vacancy 및 stability와 관련된 lead halide frameworks 의 rigidity에 영향을 줍니다. 우리는 RP와 DJ상의 2D 납 할로겐화물 페로브스카이트에서의 halide ion migration kinetic을 온도 및 두께에 따른 분광학적 측정을 통해 규명했습니다. 또한, spacer리간드의 결합모드가 다른 2D 페로브스카이트에서 halide ion migration kinetic에 대한 활성화 에너지를 각각 다음과 같이 결정했습니다; Ruddlesden-Popper(RP) phase의 경우 50.9kJ/mol, Dion-Jacobson(DJ) phase의 경우 60.8kJ/mol.

이러한 kinetic 연구는 Pb-X의 화학 결합과 관련된 성장 메커니즘과 2D 납 할로겐화물 페로브스카이트의 구조 특성에 대한 정보를 제공하기 때문에, 우리는 LED(발광 다이오드) 또는 광전지에 적합한 페로브스카이트 나노 결정을 합성할 수 있는 전략을 효율적으로 설계할 수 있습니다.